Syntheses of Metallic Cobalt Nanoparticles and Nanowires by Electroless Deposition

Mary Donnabelle Lirio Balela

2011

Table of Contents

Syntheses of Metallic Co Nanoparticles and Nanowires by Electroless Deposition

Abstract

Metal nanoparticles is one of the most promising advanced materials due to their optical, magnetic, and chemical properties significantly different from their bulk forms. In particular, cobalt (Co) displays enhanced magnetic and catalytic properties when the particle size is reduced to nanoscale. Therefore, Co nanoparticles have potential applications in magnetic recording, biomedicine, and catalysis. Co nanoparticles have been successfully synthesized by a variety of liquid-phase methods. However, the determination of the synthesis conditions for the nanoparticles remains largely empirical, and the mechanism of the particle formation is not fully understood. In the present work, Co particles with diameters of about 40 - 400 nm are synthesized by electroless deposition in boiling propylene glycol. The Co particle size is decreased to some degree by varying the concentration of reactants, and by adding nucleating agents. The formation of Co particles and the reducing power of propylene glycol are investigated by in-situ measurements of mixed potential. The mixed potential decreases with an increase in temperature and NaOH concentration, which suggests faster oxidation of propylene glycol. It also shifts abruptly to a more negative value when nucleating agents are added. This indicates that nucleating agents accelerates the oxidation of propylene glycol, as well as aid in the formation of Co particles as heterogeneous nucleation sites. Thus, it is demonstrated that electrochemical measurements, such as mixed potential, can be employed to investigate the formation of nanoparticles. In

the second part of the study, Co nanoparticles of 24 - 110 nm in mean diameters are prepared by electroless deposition in an aqueous solution at room temperature using hexachloroplatinic acid and hydrazine as nucleating and reducing agents, respectively. The formation of Co nanoparticles is studied using mixed potential measurements and linear sweep voltammetry, in conjunction with quartz crystal microbalance. When the mixed potential is below the oxidation-reduction potential of the Co(II)/Co redox pair, Co(II) are reduced. The anodic current density for hydrazine oxidation is increased in the presence of nucleating agent owing to the catalytic activity of small Pt nanoparticles. Thus, the mixed potential decreases with a higher concentration of nucleating agent, and smaller Co nanoparticles are formed. The addition of a larger concentration of NaOH results in more negative oxidation potential for hydrazine with higher anodic current. Simultaneously, the reduction potential for Co is decreased. As a result, the mixed potential shifts negatively, and the reduction of Co(II) occurs faster. When propylene glycol is used as solvent instead of water, larger Co particles are fabricated possibly due to the decrease in the rate of oxidation of hydrazine. When a magnetic field is applied during the reaction, smooth Co nanowires of about 190 nm and lengths up to 160 μm are obtained in a propylene glycol solution instead of spherical particles. On the other hand, bead-like nanowires of about 54 nm in mean diameter and 30 μm long are formed when the reaction is carried out in an aqueous solution. Thus, the morphology of the nanowires is influenced by reaction rate; the formation of smooth nanowires is favored at a slower reaction rate. Regardless of the magnetic field, spherical Co nanoparticles are first formed in the solution and then magnetized by the magnetic field. Attractive dipolar interactions are induced along the magnetic field direction, which results in the self-assembly of Co nanoparticles into nanowires.

Chapter I General Introduction

Metal nanoparticles exhibit distinct physical, chemical, electrical, and magnetic properties.[1-3] The variation in these properties is not a result of a scaling factor, but originates from different causes in each metal nanoparticle.[4] For example, in noble metal nanoparticles, it is due to the strong absorption of radiation within the visible region leading to the collective oscillation of the electrons in the conduction band (called surface plasmon resonance) from the surface of one nanoparticle to another.[1,4] In transition metal nanoparticles, it is from the large surface-to-volume ratio resulting in high chemical activities[5] and single-domain magnetic properties.[6] Therefore, a large decrease in particle size results in novel optical, chemical, and magnetic properties; these properties have great technological and fundamental scientific importance owing to their remarkable difference from the properties of their bulk forms.[7] For example, colloidal gold nanoparticles, studied by Faraday in 1857, have been used in stained glass windows in Europe and in colored vases and other ornaments in China owing to their surface plasmon resonance properties.[3] Chemically inert as bulk, gold has displayed excellent catalytic properties for oxidation of carbon monoxide, hydrocarbons, and nitrogen oxides when the particle size is reduced to nanometer range.[2,8-9] Platinum and platinum-ruthenium nanoparticles supported in different forms of carbon are also widely employed as catalysts for fuel cell reactions.[4,10-11] On the other hand, silver and copper nanoparticles, due to their high electrical conductivities, are used as commercial inks for printable electronics.[12-14] Ferromagnetic metal nanoparticle (iron, cobalt, and nickel) has potential applications in separation technology, magnetic recording, and biomedicine.[15-16] In particular, cobalt, having a saturation magnetization

comparable to that of iron, is a common component in permanent magnets. On the other hand, cobalt nanostructures, e.g. nanoparticles and nanowires, have shown a significant increase in magnetic properties with a large coercivity up to 9.0 kOe and a remanence close to 1.0. [22-23] This marked improvement in their magnetic properties makes them attractive for high-density magnetic recording.[17-18] Due to their large surface area, both Co nanoparticles and nanowires have displayed excellent catalytic activities for some reactions, e.g. hydrogenation of citral to citric alcohol and hydrogenolysis of glycerol to propanediol.[19] Further, they have shown a high catalytic activity for hydrogen generation for hydrogen storage application.[20-21]

There are many kinds of synthetic methods for the preparation of metal nanoparticles. Liquid-phase methods offer several important advantages over conventional high-temperature methods.[22] In a solution, metal nanoparticles are precipitated at a lower temperature.[22] Control of particle morphology, structure, and composition is also easily achieved by providing a convenient medium for growing the nanoparticles.[2,23-25] Examples of liquid-phase processes are reduction in reverse micelles, thermal decomposition of organometallic precursor, hydrothermal reduction, and reduction using reducing agents (electroless deposition).

The reverse micelle method involves the reduction of metal ions in micelles formed using droplets of water sustained in an organic phase by a surfactant. [25] A reverse micelle is usually a thermodynamically stable mixture of 4 components: surfactant [e.g. bis(2-ethylhexyl) s-sodium sulfosuccinate (AOT), sodium dodecyl sulfate (SDS), centyltrimethylammonium bromide (CTAB), polyoxyethylene(10) isooctylphenyl ether (Triton X-100)], co-surfactant (aliphatic alcohols with a chain length of C_6-C_8), organic

solvent, and water.[26-27] It can solubilize relatively large amounts of water, which makes them suitable for the synthesis of metal nanoparticles.[4] Since the reduction of metal ions is conducted inside the micelles and the surface of the resulting nanoparticles is covered by surfactants, it is possible to vary the particle composition, shape, and size distribution.[1-2,26] However, the synthesized nanoparticles are usually poorly crystallized with a broad size distribution.

The thermal decomposition of organometallic precursors is performed by the rapid injection of a zero-valent organometallic precursor into a hot solvent containing bulky surfactant. The surfactant adsorbs reversibly on the surface of the nanoparticles suppressing particle growth. Consequently, highly-crystallized metallic nanoparticles with a narrow size distribution are fabricated. The morphology of the nanoparticles is observed to be dependent on the type and amount of surfactant in the solution.[28-29] In this method, the main issues involve the toxicity of the reactants, particularly the metal precursor and the high-temperature solvent, and the strict requirement for an air-free atmosphere during synthesis.

An alternative approach to thermal decomposition is the use of more conventional solvents that are usually limited by their rather low boiling temperature as is demonstrated in hydrothermal method. By heating the solvent in a sealed vessel (an autoclave), the autogenous pressure far exceeds the ambient pressure, leading to an increase in the boiling point of the solvent. Co and Ni nanoparticles and nanowires have already been prepared by this method. [30-32]

On the other hand, electroless deposition is one of the most promising methods for preparing metallic nanoparticles, particularly ferromagnetic nanoparticles. It utilizes the oxidation-reduction reaction between the metal species and reducing agent in the solution.

Using this method, a large quantity of metal nanoparticles can be fabricated in a single process at a low cost since neither high vacuum nor high temperature is required.[12,33] Further, it is versatile such that reactions can be carried out in aqueous or organic solutions. Examples of reducing agents are hydrazine monohydrate,[33-35] sodium borohydride,[36-38] and polyols.[10-11,13-14,22-23].

These liquid-phase methods have their own processes and mechanisms for preparation of metal nanoparticles. However, there are basically three steps in the formation of metal nanoparticles in a homogeneous solution: reduction of metal ions to metal atoms, aggregation of metal atoms to metal nuclei, and growth of metal nuclei to metal nanoparticles as illustrated in Fig. 1.1.[5] Tailoring the particle size of metal nanoparticles is achieved by controlling the nucleation and growth rates during synthesis. Generally, a fast nucleation produces a high concentration of nuclei, leading to the suppression of particle growth. Consequently, smaller nanoparticles are formed. A slow nucleation, on the other hand, provides a small number of nuclei consuming the same amount of metal precursor. Thus, larger particles are obtained. Both nucleation and growth rates are significantly influenced by changes in several process parameters, such as reaction temperatures, concentration of reactants, types of reducing agents, concentration of nucleating agents, and addition of protective agents.

Liquid polyols are interesting among non-aqueous solvents because, like water and monoalcohols, they are hydrogen-bonded liquids with a high value of relative permittivity; they can dissolve ionic inorganic compounds so some extent. Electroless deposition of metal particles in polyols is typically carried out under ambient atmospheric pressure and temperatures up to 250 ^{o}C, depending on the nature of metals and the type of polyol. In this

process, the reaction rate is controlled by manipulating the synthesis conditions. Thus, non-agglomerated metal particles with a well-defined shape, a controlled average size from micrometer to nanometer size range, and a narrow size distribution are obtained. Although the formation of noble metal particles, such as Ag, Au, Pt, and Pd, in polyols have been investigated electrochemically,[39-40] the synthesis of Co particles has not fully been understood. Previous studies have been limited to the effect of the precipitation of intermediate solid phases from metal salts on the reaction rate and the physical properties of the Co particles.[41]

Electrochemical measurements, which are needed to delineate the mechanism of formation of Co particles, have been restricted by complex reactions occurring in parallel at the boiling point. A theoretical approach which involves the Gibbs free energy of the reduction of transition metal oxides and hydroxides to their respective metal by a polyol has been correlated with the reducibility of metal precursors at the boiling point.[42] Estimation of the free energy change, however, is based on the complete oxidation of the polyol to water and carbon dioxide, which hardly occurs during the actual synthesis due to kinetics. In the present work, in-situ mixed potential measurements are applied to study the electroless deposition of Co particles in boiling propylene glycol as discussed in Chapter II. The influence of process parameters, such as sodium hydroxide and cobalt acetate concentrations, and addition of different nucleating agents, on the particle morphology and the overall reaction rate is also investigated. These results are then correlated with the changes in mixed potentials. The optimum conditions for the synthesis of Co particles described in this chapter are applied in succeeding chapters.

The synthesis of Co nanoparticles is more commonly conducted in an organic solvent at an elevated temperature. Its fabrication at room temperature is still challenging, specifically in an aqueous solution, due to the difficulty of formation of size-controlled Co nanoparticles without agglomeration and oxidation. In addition, water is reduced by the reducing agent, resulting in a competition between Co deposition and H_2 generation. Nevertheless, using water as solvent will greatly simplify the synthesis process, and thus reduce the cost of fabrication of Co nanoparticles, which is more convenient for industrial application. The reducing agent sodium borohydride can reduce Co(II) at room temperature, but the reaction yields amorphous Co nanoparticles with a substantial amount of boron.[2,36-38] Therefore, Chapter III presents a preparation of size-controlled Co nanoparticles with a narrow size distribution by electroless deposition in an aqueous solution at room temperature. Hydrazine monohydrate and hexachloroplatinic acid are used as reducing and nucleating agents, respectively. Contamination of Co nanoparticles is avoided with the use of hydrazine monohydrate. The formation of Co nanoparticles is investigated by in-situ monitoring of the mixed potentials in conjunction with quartz crystal microbalance. The effects of concentrations of sodium hydroxide, hexachloroplatinic acid, and hydrazine monohydrate on the reaction rate and particle morphology are examined. Linear sweep voltammetry are conducted to determine the anodic and cathodic currents associated with hydrazine oxidation and cobalt deposition, and the oxidation and reduction potentials of hydrazine and Co are then separately evaluated from the anodic and cathodic current curves. Based on the electrochemical study, a formation mechanism of Co nanoparticles is proposed.

The fabrication of one-dimensional (1-D) ferromagnetic nanostructures, such as nanowires and nanorods, have attracted considerable interest due to their novel properties

and many applications.[17,43-44] Template-based synthetic methods using anodized aluminum oxide, polycarbonate membranes, or tobacco mosaic virus, is quite successful in preparing well-aligned magnetic nanowires and nanorods with tunable diameter and length.[44-47] However, the preparation of the templates and their subsequent removal complicates the synthetic process.[48-50] Recently, the application of magnetic fields during solution reduction is being used to fabricate anisotropic nanostructures due to its simplicity and effectiveness. For example, Fe_3O_4 nanochains,[51] Ni-Co alloy microwires,[52-53] Co nanorods, [31,49,54] and Ni nanowires[32,48,50] have already been prepared by magnetic-field-assisted hydrothermal synthesis. This indicates that the formation of smooth metal nanowires under the magnetic field is promoted in slow processes. Thus, a rapid formation of Co nanowires by electroless deposition at room temperature under a magnetic field is discussed in Chapter IV. The variation in wire morphology is studied in different reaction rates. The influences of magnetic field strength, concentrations of hexachloroplatinic acid and hydrazine, and types of solvent on the size of Co nanowires are investigated. Electrochemical study of the formation of Co nanowires is carried out using linear sweep voltammetry and in-situ mixed potential measurements. A formation mechanism of Co nanowires is then discussed.

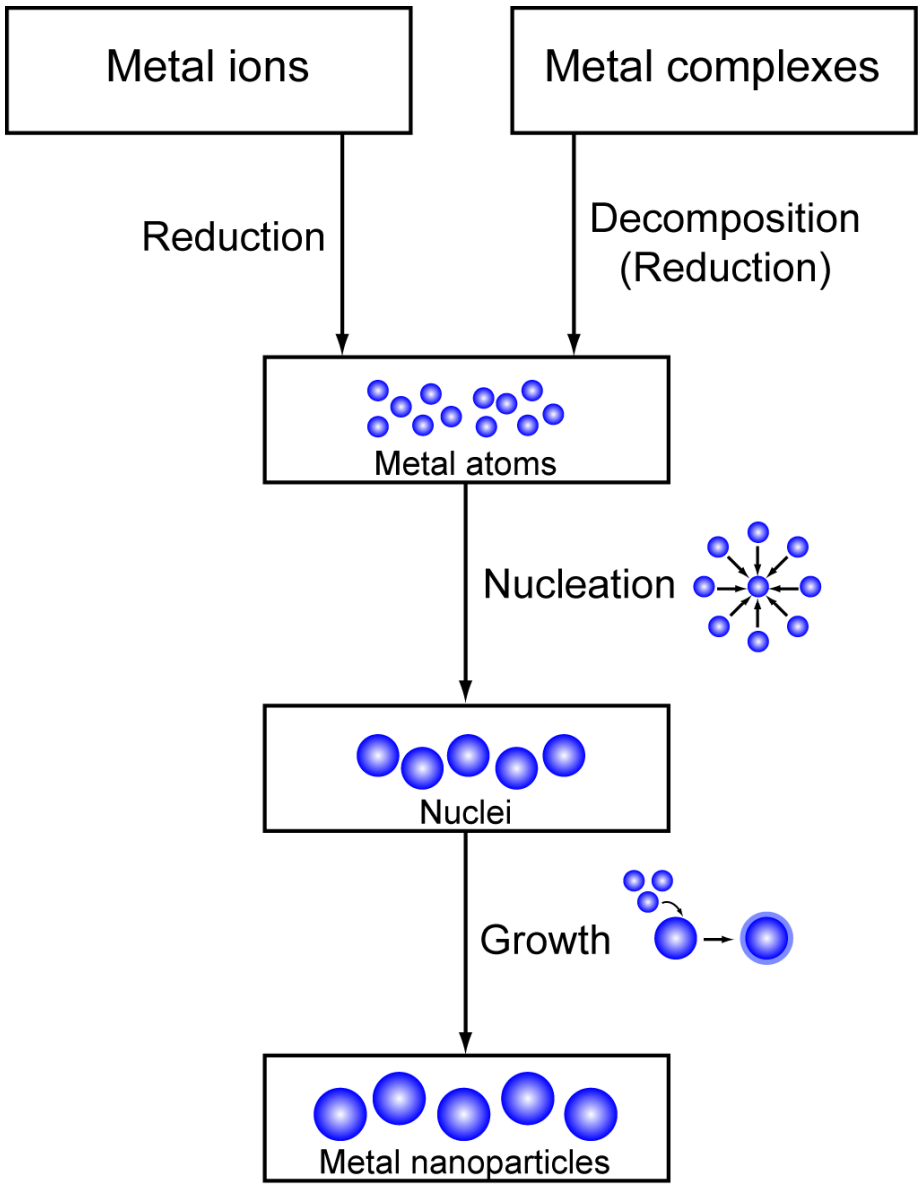

Figure 1.1 Preparation of metal nanoparticles in homogeneous solution by liquid-phase method.[5]

References

1. G. Cao, *Nanostructures and Nanomaterials: Synthesis, Properties and Applications*. Imperial College Press, London (2004).

2. S. P. Gubin, Y. A. Koksharov, G. B. Khomutov, and G. Yu Yurkov, "Magnetic Nanoparticles: Preparation, Structure and Properties", *Russ. Chem. Rev*., **74**, 489 (2005).

3. G. B. Sergeev, *Nanochemistry*. Elsevier, Amsterdam (2006).

4. C. Burda, X. Chen, R. Narayanan, and M. A. El-Sayed, "Chemistry and Properties of Nanocrystals of Different Shape", *Chem. Rev*., **105**, 1025 (2005).

5. N. Toshima, "Metal Nanoparticles for Catalysis", *Nanoscale Material*, ed. L. M. Liz-Marzan, and P. V. Kanat, Springer/Kluwer Academics, New York (2003).

6. X. Batlle, and A. Labarta, "Finite-Size Effects in Fine Particles: Magnetic and Transport Properties", *J. Phys. D: Appl. Phys*., **35**, R15 (2002).

7. B. L. Cushing, V. L. Kolesnichenko, and C. J. O'Connor, "Recent Advances in the Liquid-Phase Syntheses of Inorganic Nanoparticles", *Chem. Rev*., **104**, 3893 (2004).

8. H. Zhu, C. Tao, S. Zheng, S. Wu, and J. Li, "Effect of Alkyl Chain on Phase Transfer of Surfactant Capped Au Nanoparticles Across the Water/Toluene Interface", *Colloids Surf. A: Physicochem. Eng. Aspects*, **256**, 17 (2005).

9. Z.-C. Xu, C. M. Shen, T.-Z. Yang, H.-R. Zhang, H.-L. Li, J.-Q. Li, and H.-J. Gao, "From Aqueous to Organic: A Step-by-Step Strategy for Shape Evolution of Gold Nanoparticles", *Chem. Phys. Lett.*, **415**, 342 (2005).

10. R. M. Rioux, H. Song, M. Grass, S. Habas, K. Niesz, J. D. Heofelmeyer, P. Yang, and G. A. Somojai, "Monodisperse Platinum Nanoparticles of Well-Defined Shape: Synthesis,

Characterization, Catalytic Properties and Future Prospects", *Topics in Catalysis*, **39**, 167 (2006).

11. Y. Chen, K. Y. Liew, and J. Li, "Size-Controlled Synthesis of Ru Nanoparticles by Ethylene Glycol Reduction", *Mater. Lett.*, **62**, 1018 (2008).

12. S. Yagi, H. Nakanishi, E. Matsubara, S. Matsubara, T. Ichitsubo, K. Hosoya, and Y. Matsuba, "Formation of Cu Nanoparticles by Electroless Deposition Using Aqueous CuO Suspension", *J. Electrochem. Soc.*, **155**, D474 (2008).

13. Y. Sun, B. Gates, B. Mayers, and Y. Xia, "Crystalline Silver Nanowires by Soft Solution Process", *Nanolett.*, **2**, 165 (2002).

14. Y. Sun, Y. Yin, B. T. Mayers, T. Herricks, and Y. Xia, "Uniform Silver Nanowires Synthesis by Reducing $AgNO_3$ with Ethylene Glycol in the Presence of Seeds and Poly(Vinyl Pyrrolidone)", *Chem. Mater.*, **14**, 4736 (2002).

15. P. Cojocaru, L. Magagnin, E. Gomez, and E. Valles, "Electrodeposition of CoNi and CoNiP Alloys in Sulphamate Electrolytes", *J. Alloys Comp.*, **503**, 454 (2010).

16. P. Tartaj, M. P. Morales, S. Veintemillas-Verdaguer, T. Gonzalez-Carreno, and C. J. Serna, "The Preparation of Magnetic Nanoparticles for Applications in Biomedicine", *J. Phys D: Appl. Phys*. **36**, R182 (2003).

17. G. Viau, C. Garcia, T. Maurer, G. Chaboussant, F. Ott, Y. Soumare, and J.-Y. Piquemal, "Highly Crystalline Cobalt Nanowires with High Coercivity Prepared by Soft Chemistry", *Phys. Status Solidi. A*, **206**, 663 (2009).

18. Y. Soumare, J.-Y. Piquemal, T. Maurer, F. Ott, G. Chaboussant, A. Falqui, and G. Viau, "Oriented Magnetic Nanowires with High Coercivity", *J. Mater. Chem.*, **18**, 5696 (2008).

19. Q. Liu, X. Guo, J. Chen, J. Li, W. Song, and W. Shen, “Cobalt Nanowires Prepared by Heterogeneous Nucleation in Propanediol and their Catalytic Properties”, *Nanotech.,* **19**, 365608 (2008).

20. S. K. Singh, X.-B. Zhang, and Q. Xu, “Room-Temperature Hydrogen Generation from Hydrous Hydrazine for Chemical Hydrogen Storage”, *J. Am. Chem. Soc.*, **131**, 9894 (2009).

21. B. H. Liu, Z. P. Li, and S. Suda, “Nickel- and Cobalt-Based Catalysts for Hydrogen Generation by Hydrolysis of Borohydride”, *J. Alloys Comp.*, **415** 288 (2006).

22. R. E. Cable and R. E. Schaak, “ Low-Temperature Solution Synthesis of Nanocrystalline Binary Intermetallic Compounds Using the Polyol Process”, *Chem. Mater.*, **17**, 6835 (2005).

23. G. Viau, F. Fiévet-Vincent, and F. Fiévet, “Nucleation and Growth of Bimetallic CoNi and FeNi Monodisperse Particles Prepared in Polyols”, *Solid State Ionics*, **84**, 259 (1996).

24. T. Hyeon, “Chemical Synthesis of Magnetic Nanoparticles”, *Chem. Comm.*, **10** 927 (2002).

25. D. V. Talapin, E. V. Shevchenko, and H. Weller, “Synthesis and Characterization of Magnetic Nanoparticles”, *Nanoparticles: From Theory to Application*, ed. G. Schmid, Wiley-VCH, Germany (2004).

26. W. Liang, M. Liu, and G. Guo, “Microemulsion”, *Handbook of Nanophase and Nanostructured Materials: Volume I: Synthesis*, ed. Z. L. Wang, Y. Liu,and Z. Zhang, Kluwer Academics/Plenum Publishers, New York (2003).

27. X.-M. Lin, and A. C. S. Samia, “Synthesis, Assembly and Physical Properties of Magnetic Nanoparticles”, *J. Magn. Magn. Mater*., **305**, 100 (2006).

28. N. Shukla, E. B. Svedberg, J. Ell, and A. J. Roy, “Surfactant Effects on the Shapes of Cobalt Nanoparticles” *Mater. Lett*., **60**, 1950 (2006).

29. V. F. Puntes, K. Krishnan, and A. P. Alivisatos, “Synthesis of Colloidal Cobalt Nanoparticles with Controlled Size and Shapes”, *Topics in Catalysis,* **19**, 145 (2002).

30. C. Jiang, L. Wang, and K. Kuwabara, “Selective-Precursor Reducing Route to Cobalt Nanocrystals and Ferromagnetic Property”, *J. Solid State Chem.*, **180**, 3146 (2007).

31. B.-Q. Xie, Y. Qian, S. Zhang, S. Fu, and W. Yu, “A Hydrothermal Reduction Route to Single-Crystalline Hexagonal Cobalt Nanowires”, *Eur. J. Inorg. Chem.,* **2006**, 2454 (2006).

32. M. Zhang, J. Deng, M, Zhang, and W. Li, “Shape-Controlled Synthesis of Nickel Wires Using an External Magnetic Field”, *Chinese J. Catalysis*, **30**, 447 (2009).

33. S. Yagi, T. Koyonagi, H. Nakanishi, T. Ichitsubo, and E. Matsubara, “Formation of Nickel Nanoparticles by Electroless Deposition Using NiO and Ni(OH)2 Suspensions”, *J. Electrochem. Soc.*, **155**, D583 (2008).

34. M. D. L. Balela, S. Yagi, and E. Matsubara, “Room-Temperature Synthesis of Cobalt Nanoparticles by Electroless Deposition in Aqueous Solution”, *Electrochem. Solid-State Lett.*, **13**, D4 (2010).

35. M. D. L. Balela, S. Yagi, and E. Matsubara, “Room-Temperature Synthesis of Cobalt Nanoparticles in Aqueous Solution”, *ECS Trans.*, **28**, 29 (2010).

36. V. Salgueriño-Maceira, M. A. Correa-Duarte, M. Farle, M. A. Lopez-Quintela, K. Sieradzki, and R. Diaz, “Synthesis and Characterization for Colloidal Cobalt Particles’, *Langmuir,* **22**, 1455 (2006).

37. Y.-W. Zhao, R. K. Zheng, X. X. Zhang, and J. Q. Xiao, “A Simple Method to Prepare Uniform Co Nanoparticles”, *IEEE Trans. Magn*., **39**, 2764 (2003).

38. S. Ram, “Allotropic Phase Transformations in HCP, FCC and BCC Metastable Structures in Co-Nanoparticles” *Mater. Sci. Eng A*, **304**, 923 (2001).

39. F. Bonet, C. Guéry, D. Guyomard, R. Herrera Urbina, K. Tekaia-Elhsissen, and J. M. Tarascon, "Electrochemical Reduction of Noble Metal Species in Ethylene Glycol at Platinum and Glassy Carbon Rotating Disk Electrodes", *Solid State Ionics,* **126**, 337 (1999).

40. F. Bonet, C. Guéry, D. Guyomard, R. Herrera Urbina, K. Tekaia-Elhsissen, and J. M. Tarascon, "Electrochemical Reduction of Noble Metal Compounds in Ethylene Glycol", *Intl. J. Inorganic Mater.,* **1**, 47 (1999).

41. R.J. Joseyphus, T. Matsumoto, H. Takahashi, D. Kodama, K. Tohji, and B. Jeyadevan, "Designed Synthesis of Cobalt and its Alloys by Polyol Process", *J. Solid State Chem.*, **180**, 3008 (2007).

42. D. Larcher and R. Patrice, "Preparation of Metallic Powders and Alloys in Polyol Media: A Thermodynamic Approach", *J. Solid State Chem.*, **154**, 405 (2000).

43. E. K. Athanassiou, P. Grossman, R. N. Grass, and W. J. Stark, "Template Free, Large Scale Synthesis of Cobalt Nanowires Using Magnetic Fields for Alignment", *Nanotech.*, **18**, 165606-165613 (2007).

44. M. Aslam, R. Bhobe, N. Alem, S. Donthu, and V. P. Dravid, "Controlled Large-Scale Synthesis and Magnetic Properties of Single-Crystal Cobalt Nanorods", *J. Appl. Phys.*, **98**, 074311 (2005).

45. N. B. Chaure, P. Stamenov, F. M. F. Rhen, and J. M. D. Coey, "Oriented Cobalt Nanowires Prepared by Electroless Deposition in a Porous Membrane", *J. Magn. Magn. Mater.*, **290**, 1210 (2005).

46. L. Vila, P. Vincent, L. Dauginet–De Pra, G. Pino, E. Minoux, L. Gangloff, S. Demoustier–Champagne, N. Sarazin, E. Ferain, R. Legras, L. Piraux, and P. Legagneux,

"Growth and Field-Emission Properties of Vertically Aligned Cobalt Nanowire Arrays", *Nanolett.*, **4**, 521 (2004).

47. M. Knez, A. M. Bittner, F. Boes, C. Wege, H. Jeske, E. Maiβ, and K. Kern, "Biotemplate Synthesis of 3-nm Nickel and Cobalt Nanowires", *Nanolett.*, **3**, 1079 (2003).

48. C. Gong, J. Tian, T. Zhao, Z. Wu, and Z. Zhang, "Formation Of Ni Chains Induced By Self-Generated Magnetic Field" *Mater. Research Bull.*, **44**, 35 (2009).

49. J. Wang, M. Yao, C. Xu, Y. Zhu, G. Xu, and P. Cui, "Magnetic Chanins of Co Spheres Synthesized by Hydrothermal Process Under Magnetic Field", *Mater. Lett.*, **62**, 3431 (2008).

50. C. Gong, L. Yu, Y. Duan, J. Tian, Z. Wu, and Z. Zhang, "The Fabrication and Magnetic Properties of Ni Fibers Synthesized Under External Magnetic Fields", *Eur. J. Inorg. Chem.*, **2008**, 2884 (2008).

51. H. Wang, Q.-W. Chen, L.-X. Sun, H. Qi, S. Zhou, and J. Xiong, "Magnetic-Field-Induced Formation of One-Dimensional Magnetite Nanochains", *Langmuir*, **25**, 7135 (2009).

52. M. Wu, G. Liu, M. Li, P. Dai, Y. Ma, and L. Zhang, "Magnetic Field-Assisted Solvothermal Assembly of One-Dimensional Nanostructures of Ni-Co Alloy Nanoparticles", *J. Alloys and Compounds*, **491**, 689 (2010).

53. M. J. Hu, B. lin, S. H. Yu, "Magnetic Field-Induced Solvothermal Synthesis of One-Dimensional Assemblies of Ni-Co Alloy Microstructures", *Nano. Res.*, **1**, 303 (2008).

54. F. Liang, L. Guo, Q. P. Zhong, X. Wen, S. Yang, W. Zheng, C. Chen, N. Zhang, and W. Chu., "One-Step Solution Fabrication Of Magnetic Chains Consisting Of Jingle-Bell-Shaped Cobalt Mesospheres", *Appl. Phys. Lett.*, **89**, 103105 (2006).

Chapter II Electroless Deposition of Co Particles by the Polyol Process

2.1 Introduction

The polyol synthesis, that is the synthesis of metal particles by electroless deposition in polyol, has been extensively studied over the years.[1-5] It is widely used due to its simplicity since polyol acts as both solvent and reducing agent, and in some cases also as a protective agent for agglomeration. Deposition of metal particles in polyols proceeds through the following steps: (i) formation and dissolution of intermediate solid phases, (ii) reduction of metal ions, and (iii) nucleation and growth of metal particles.[3,6] The nucleation and growth can be effectively separated by controlling the process parameters, such as temperature, concentration of reactants, types of polyol, and addition of nucleating agents.[7-9] Thus, size-controlled metal particles with different compositions and a very narrow size distribution can be produced. Metal particles of Co,[3,9-10] Ni,[11] Fe,[12-13] Ag,[7,14] Pt,[15] and their alloys,[4-5,16-19] have been synthesized by this method.

The overall reaction in polyol synthesis consists of the reduction of metal species in solution and the simultaneous oxidation of polyols. For example, the electrochemical reduction of noble metal ions in ethylene glycol using platinum and glassy carbon rotating disk electrodes at room temperature up to 60 ºC has been studied.[20-21] It is reported that ethylene glycol is electrochemically stable at room temperature from −1.15 to 1.65 V vs SCE (saturated calomel electrode) on a glassy carbon electrode, while it is stable from −0.82 to 2.0 V vs SCE on a Pt electrode. On the other hand, few reports are available on the electrochemical study of the reduction of ferromagnetic metals by polyols. These metals are

more difficult to reduce in polyols, and their synthesis conditions have been determined empirically. In this chapter, a formation of Co particles by electroless deposition in boiling propylene glycol is presented. The influence of process parameters, i.e. concentrations of sodium hydroxide, Co(II) acetate, and various nucleating agents, on the morphology and size distribution of nanoparticles have been studied. The magnetic properties of the Co particles, such as saturation magnetization and coercivity, are measured at room temperature. The electrochemical behavior of propylene glycol at high temperatures up to the boiling point is evaluated by in-situ measurements of the mixed potential, and the optimum conditions for the deposition of Co particles are determined.

2.2 Experimental

2.2.1 Preparation of Co particles

Co(II) acetate tetrahydrate [$Co(C_2H_3O_2)_2{\cdot}4H_2O$] was used as a Co(II) ionic source. Silver nitrate ($AgNO_3$), palladium chloride ($PdCl_2$), and hexachloroplatinic acid hexahydrate ($H_2PtCl_6{\cdot}H_2O$) were used as nucleating agents. Propylene glycol ($C_3H_8O_2$, PG) was used as solvent, reducing agent, and dispersing agent. Sodium hydroxide (NaOH) was added to provide OH^- ions into the solutions. All chemicals in the present study were the reagent grade.

A 0.10 mol dm^{-3} (M) Co(II)-PG solution was prepared by dissolving Co(II) acetate tetrahydrate powder in 75 cm^3 PG solution containing 0.25 M NaOH. With nucleating agents, 2.5 mM $AgNO_3$, $PdCl_2$, or $H_2PtCl_6{\cdot}H_2O$ was added. The reaction solution was then mechanically agitated and heated to the boiling temperature of about 150 - 165 °C for 1 - 3 hours, depending on the concentration of reactants. After the reaction, Co particles were

separated by centrifugation and washed several times with ethanol and acetone prior to drying in a vacuum at room temperature.

2.2.2 Analysis of Co particles

The morphology of Co particles was observed by a transmission electron microscope (TEM, Philips CM12) and a field-emission scanning electron microscope (Zeis Supra 55VP and JEOL JSM 6500-F). The mean diameter was determined by the image analysis of 300 particles randomly selected in each sample. The structure was analyzed by X-ray diffraction (XRD, MAC Science M03XHF22) using Cr *K*α. Magnetic properties, such as saturation magnetization and coercivity, were measured at room temperature using a vibrating sample magnetometer (VSM, DMS Model 10) with a magnetic field of 2 T. In-situ mixed potential measurements and linear sweep voltammetry were carried out on a platinum (Pt) sheet with an active surface area of 360 mm^2 using a potentiostat/galvanostat (Hokuto Denko Co. Ltd., HA-151). The Pt sheet was mechanically polished before each measurement. A Ag/AgCl electrode (Horiba, 2565A-10T) immersed in 3.33 M KCl aqueous solution and a Pt plate were the reference and counter electrodes, respectively. The reference electrode was connected to the reaction solution through a glass bridge filled with the starting Co(II)-NaOH-PG solution. In this chapter, all potentials were reported against the potential of the Ag/AgCl electrode [0.206 V vs standard hydrogen electrode (SHE) at 25 °C].

2.2.3 Electrochemical consideration

2.2.3.1 Reduction reactions

During the reaction in propylene glycol, a number of anodic and cathodic partial reactions occur simultaneously. The primary cathodic partial reactions are Co deposition and hydrogen (H_2) generation. With nucleating agents, Ag, Pd, or Pt deposition takes place earlier than the above reactions because of their higher oxidation-reduction potentials.[22-23] The cathodic partial reactions are written as follows:

Ag deposition

$$Ag(I) + e^- \rightarrow Ag \quad (2\text{-}1)$$

Pd deposition

$$Pd(II) + 2e^- \rightarrow Pd \quad (2\text{-}2)$$

Pt deposition

$$Pt(IV) + 4e^- \rightarrow Pt \quad (2\text{-}3)$$

Co deposition

$$Co(II) + 2e^- \rightarrow Co \quad (2\text{-}4)$$

H_2 generation

$$2H_2O + 2e^- \rightarrow H_2 + 2OH^- \quad (2\text{-}5)$$

Co(II) is in a dynamic equilibrium with the solution and the solid intermediate phase formed from the reaction of Co(II) with propylene glycol and OH^- ions in the solution.[8,24] It also represents all the Co(II) species in the solution, i.e. Co alkoxide, Co^{2+}, $Co(OH)_2$, $HCoO_2^-$ or $Co(OH)_3^-$, CoO_2^{2-} and $Co(OH)_4^{2-}$.

The oxidation-reduction potentials of the above redox pairs could not be calculated due to insufficient thermodynamic data in propylene glycol. Experimental evaluation of the reduction potential of Co is also difficult at the boiling point of propylene glycol due to complex reactions occurring in parallel with Co deposition, e.g. the decomposition of propylene glycol and the evaporation of volatile products.

2.2.3.2 Oxidation reactions

The primary anodic partial reactions are the oxidation reactions of propylene glycol. The reaction formula of propylene glycol oxidation is as follows: [25-26]

First Stage: Dehydration of propylene glycol

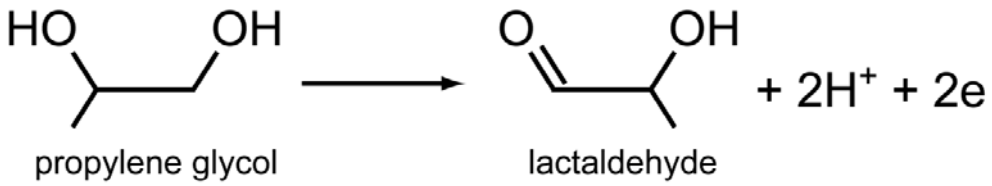

Second Stage: Oxidation of aldehyde

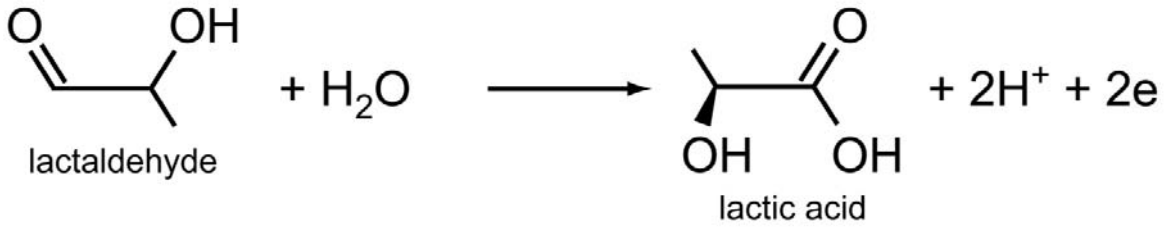

First, propylene glycol is dehydrated to form lactaldehyde. Lactaldehyde, which has a lower boiling temperature than propylene glycol, is subsequently oxidized to lactic acid.

Figure 2.1 shows the anodic polarization curve of propylene glycol on a Pt electrode at room temperature. The anodic sweep was started from the rest potential up to 2.0 V at a rate of 1 mV s^{-1}. The anodic current was observed at about 1.0 V, which is the onset of oxidation of propylene glycol.

2.2.3.3 In-situ mixed potential measurement

In an electrochemical system, the current (I_{total}) measured on anodic and cathodic electrodes are the sum of the anodic and cathodic partial currents, respectively. Namely, there are the following faradaic processes:

$$O_1 + n_1 e^- \leftrightarrow R_1 \tag{2-6}$$

$$\begin{matrix} O_2 + n_2 e^- \leftrightarrow R_2 \\ \vdots \end{matrix} \tag{2-7}$$

where n_i are the number of electrons exchanged in the ith oxidation/reduction processs. Thus, the observed anodic and cathodic currents are the sum of all partial anodic and cathodic reactions:

$$I_{total,anodic} = I_{anodic,1} + I_{anodic,2} + \ldots \tag{2-8}$$

$$\begin{matrix} I_{total,cathodic} = I_{cathodic,1} + I_{cathodic,2} + \ldots \\ \vdots \end{matrix} \tag{2-9}$$

In such a system, we can observe a potential where the absolute values of the total anodic and cathodic currents are equal as it is seen in Fig. 2.2. [28]

$$\left|I_{\text{total,anodic}}\right| = \left|I_{\text{total,cathodic}}\right| \tag{2-10}$$

Thus, by coupling with thermodynamic calculation, we can predict a final product in the reaction solution. [29-31]

2.3 Observation by SEM and XRD

Figure 2.3 shows the Co particles prepared by electroless deposition in boiling PG solutions with 0.10 M Co(II) acetate and 0 - 0.40 M NaOH. The starting time of reduction of Co(II) decreases with an increase in NaOH concentration. Without NaOH, the reduction of Co(II), indicated by a change in a color of solution from purple to black, starts after about 3 hr at 165 °C. The reaction does not reach completion even at 6 h. The large hollow Co alkoxide[24] particles are observed with small metallic Co particles in Fig. 2.3(a). The agglomerates of Co nanoparticles from 0.40 to 2.0 μm in diameter are present.

The viscosity of the solution increases by addition of NaOH, and the reaction time is greatly reduced. For example, the reaction is completed by 3 h at 165 °C at 0.10 M NaOH and Co particles of about 0.70 μm diameter are formed. At 0.25 M NaOH, Co particles of about 0.30 μm diameter are prepared by 2 h. It is clearly seen in Fig. 2.3 that the size distribution of Co particles becomes sharper with a larger NaOH concentration up to 0.25 M. The increase in the driving force for the reduction of Co(II) promotes a homogeneous nucleation of Co particles.[4,17] This results in a sharper size distribution. At 0.40 M NaOH, the boiling temperature is decreased to 155 °C. Large Co particles are obtained after 1 h

reaction time. At a very high concentration of NaOH, the primary Co nanoparticles possibly agglomerate, leading to an increase in the apparent particle size.[16,24]

Figure 2.4 shows the XRD patterns of the nanoparticles in Fig. 2.3. The diffraction peaks of Co products are fundamentally attributed to both hexagonal close-packed (hcp) and face-centered cubic (fcc) Co. The strongest peak at 68.0° and the small peaks at 80.5° and 132.0° are 111, 200, and 220 of fcc Co, respectively. The shoulders at higher scattering angles of the peaks at 68.0° and 132.0° are due to the presence of the 002 and 110 hcp Co peaks at 68.9° and 132.2°. The diffused peaks at 63.8° and 73.6° are 100 and 101 of hcp Co. In the absence of NaOH, relatively strong hcp Co peaks are observed. A slow reduction rate possibly promotes the formation of hcp Co which is the thermodynamically stable phase at a low temperature. Although large hollow Co alkoxide particles are observed in the sample of Fig. 2.3(a), only Co peaks are determined in the XRD profile in Fig. 2.4(a). Therefore, it is possible that the Co alkoxide particles are amorphous. The crystallite size of the samples calculated from the 111 fcc Co peaks by Scherrer's equation is about 15.9 - 26.0 nm and much smaller than the apparent particle diameters. This is consistent with the observation of agglomerates in Fig. 2.3. The crystallite size listed in Table 2.1 decreases with an increase in NaOH concentration up to 0.25 M possibly due to the enhanced nucleation of Co.

2.4 Discussion

2.4.1 Effect of increasing NaOH concentration

Figure 2.5 shows the change in mixed potential with temperature up to the boiling point of PG solutions with 0 - 0.40 M NaOH. The mixed potential decreases with an increase in temperature. Without NaOH, the mixed potential is about 0.050 V at 50 °C and

shows a minimum value (about –0.50 V) at the boiling temperature of about 165 °C. Thus, Co(II) is easily reduced at the boiling point of the polyol.[11,24,27] The addition of NaOH negatively shifts the mixed potentials. At 0.10 M NaOH, the mixed potential is about –0.14 V at 50 °C. This change in the mixed potential is due to the presence of OH^- ions which accelerates the decomposition of PG. In the absence of NaOH, the dehydrogenation of PG is slow, which leads to higher potentials. Consequently, the reduction of Co(II) proceeds slowly and large Co particles are produced in Fig. 2.3(a). The slower reaction rate favors the growth of thermodynamically stable hcp Co as it is seen in Fig. 2.4(a). In contrast, the mixed potential of PG is lower in the presence of NaOH. Thus, the reducing force of propylene glycol becomes stronger at higher NaOH concentration. This results in the homogeneous nucleation of many Co nuclei at the beginning of the reaction and smaller Co particles with sharper size distribution are formed. On the other hand, the potential shows a local at 0.40 M NaOH at 140 °C. This is due to rapid dehydrogenation of PG at much lower boiling temperatures.

2.4.2 Effect of increasing Co(II) acetate concentration

Figure 2.6 shows the SEM images of the Co particles obtained from PG solutions with 0.25 M NaOH and different amounts of Co(II) acetate. The average particle size decreases with an increase in concentration of Co(II) acetate. A larger number of Co nuclei are formed at a higher concentration of Co(II) acetate.[32-33] The standard deviation of the particle size is about 15 % in all samples. This indicates sharp size distribution.

2.4.3 Effect of addition of nucleating agent

Figure 2.7 shows TEM images of Co particles synthesized with and without nucleating agents. The addition of the nucleating agents such as $AgNO_3$, $PdCl_2$, and H_2PtCl_6 significantly decreases the size of Co particles. Further, the reaction time is reduced to less than 1 h. The average size of Co particles is plotted against the concentration ratio of [X]/[Co], where X = Ag, Pd, Pt in Fig. 2.8. Smaller Co particles are synthesized with larger concentrations of nucleating agent. The particle sizes are drastically changed by the addition of $AgNO_3$ and the smallest Co particles of about 106 nm in diameter are formed at 2.5×10^{-2}. Beyond this concentration ratio, only agglomerated particles are obtained. Ag particles are easily agglomerated at elevated temperatures.[14,34] Thus, the Ag particles do not effectively work as the nuclei of Co particles. Similar results have been previously reported by Viau et al.[4] who synthesized $Co_{80}Ni_{20}$ particles in ethylene glycol using $AgNO_3$. In contrast, particles of 40 - 120 nm are prepared with $PdCl_2$ and H_2PtCl_6. Pt salts with relatively high solubility in PG effectively work as nucleating agents and produce fine particles.[34]

Figure 2.9 shows the mixed potential measured in the reaction solutions without and with nucleating agents (2.5 mM $AgNO_3$, $PdCl_2$, or H_2PtCl_6). Without any nucleating agent, the mixed potential is near –0.30 V at 50 °C, which is close to the value obtained for a PG solution with 0.25 M NaOH in Fig 2.5(c). With an increase in temperature, the mixed potential gradually decreases until the potential reaches the minimum of about –0.92 V at 150 °C. The mixed potential then remains almost constant at about –0.90 V over 150 ˚C up to the higher limit of the boiling point, 165 °C. The color of the reaction suspension subsequently changes to black, indicating that the reduction of Co(II) near 165 °C. In the

presence of nucleating agents, the mixed potential is a much larger negative value, and the boiling temperature decreases below 165 °C. The boiling temperature decreases to 155 °C with $AgNO_3$ and $PdCl_2$. With $PdCl_2$, the minimum of the mixed potential at about –0.90 V is attained around 140 °C. With H_2PtCl_6, the smallest mixed potential is about –0.90 V at 120 °C, and the potential is stable until boiling at 150 °C. With nucleating agents, Co particles are obtained in less than 1 h. Therefore, the decrease in both the mixed potential and the boiling temperature suggest that nucleating agents do not only supply the nucleation sites for Co particles, but also accelerate the oxidation of propylene glycol. Consequently, Co nanoparticles are formed at a shorter time. Further, the nature of nucleating agent seems to influence the reaction kinetics to some extent. When H_2PtCl_6 is used, the reduction reaction is greatly enhanced, leading to the finest Co particles in Fig. 2.7(d).

2.4.4 Room-temperature magnetic properties of Co particles

Figure 2.10 shows the changes in coercivity of the Co particles with respect to the average particle size. The maximum coercivity of about 560 Oe is achieved by the Co nanoparticles with an average size of 61 nm. The coercivity of the particles larger than 61 nm decreases with an increase in particle size, whereas the coercivity of the Co nanoparticles smaller than 61 nm in mean diameter is reduced with a decrease in particle size. This clearly suggests two mechanisms of magnetization reversal.[5,35] The larger particles exhibits multi-domain behavior where magnetization reversal is achieved by domain wall motion.[5,35]. This is verified by the linear relationship between coercivity and the inverse of the mean particle size in the inset of Fig. 2.10. In contrast, the smaller particles have single-domain properties

where magnetization reversal is accomplished by coherent spin rotation.[5,35]. The decline of the coercivity with the decrease in particle size is due to thermal effects.[36-37]

The highest saturation magnetization of about 168 emu g^{-1} is attained by the Co particles of about 364 nm in diameter. This value is close to the saturation magnetization for bulk hcp Co (~166 emu $g^{-1.}$).[35-37] The saturation magnetization of the Co particles increases with the particle size as shown in Fig 2.11. This is ascribed to the contribution of the impurities at surface of Co particles.

2.5 Summary

We have investigated the electroless deposition of Co particles in boiling propylene glycol by in-situ measurement of mixed potential. The mixed potential of propylene glycol decreases with an increase in temperature and with the addition of NaOH. This implies a faster oxidation of propylene glycol. Consequently, Co(II) reduction is enhanced. The mean diameter of the Co particles is varied to some extent by changing the concentration of the reactants and by the addition of nucleating agents. With nucleating agents, the mixed potential is lowered and the reduction of Co(II) occurs at temperatures below the boiling point of propylene glycol. Thus, the nucleating agent aids in the formation of Co particles with sharp size distributions and accelerates the kinetics of the redox reactions. In addition, the nature of the nucleating agent apparently influences the reaction rate. When H_2PtCl_6 is used, the reaction temperature is significantly lowered, and the finest Co nanoparticles are formed. The Co particles are ferromagnetic at room temperature. The largest coercivity of about 560 Oe is attained by the Co particles 61 nm in mean particle size. The present study

demonstrates that in-situ monitoring of the mixed potential can be utilized for the study of the reaction conditions favorable for particle formation.

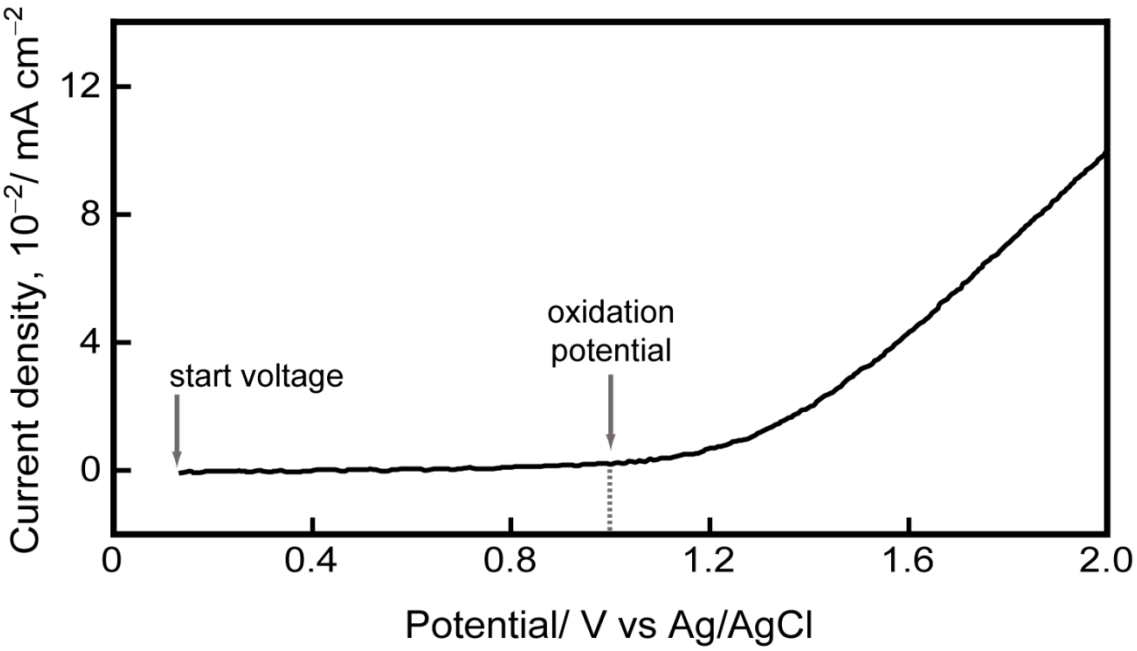

Figure 2.1 Voltammogram of the oxidation of propylene glycol measured on a Pt electrode at room temperature. The sweep rate was 1 mV s^{-1}. 0.10 M $LiClO_4$ is added as supporting electrolyte.

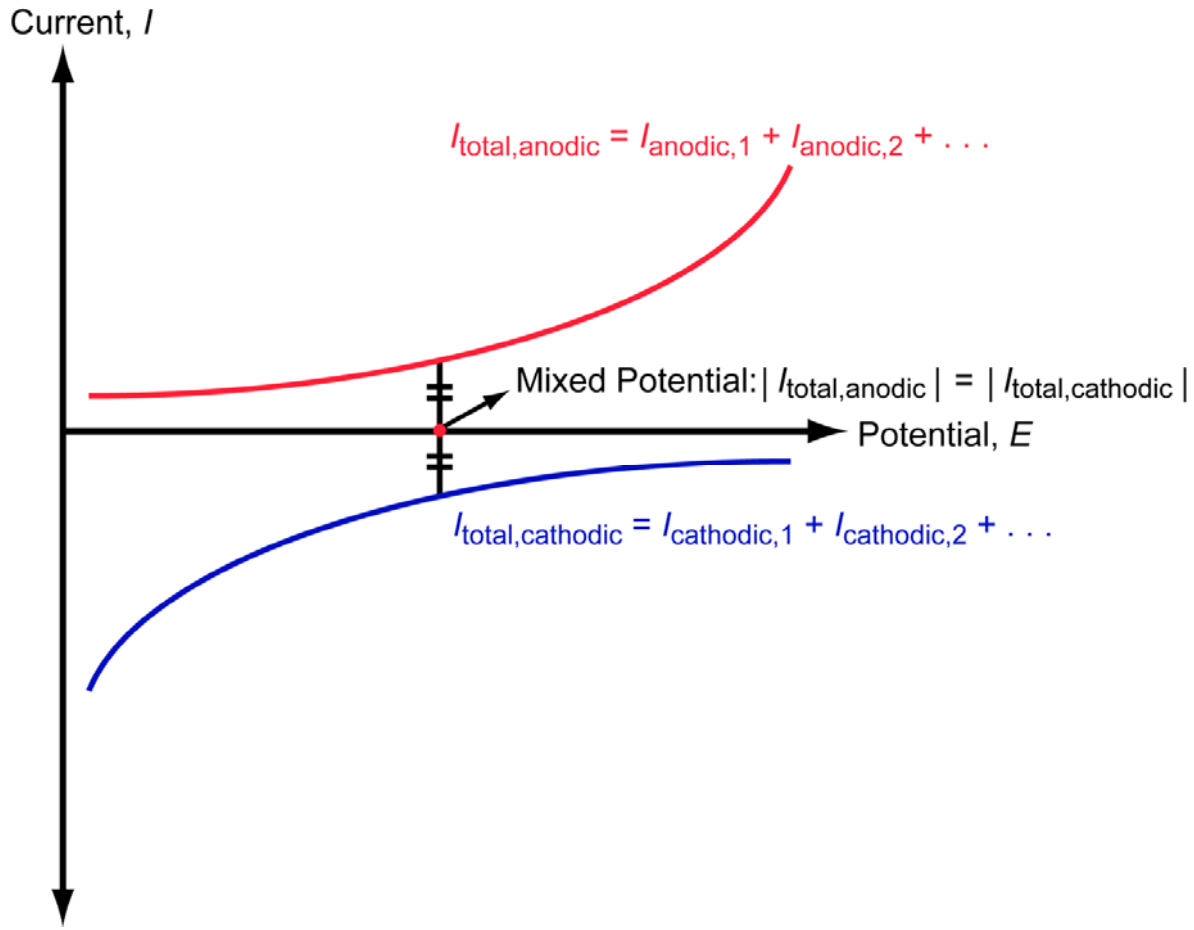

Figure 2.2 A schematic diagram of a potential-current curve. The mixed potential corresponds to the potential where the absolute value of the total anodic current ($I_{total,\ anodic}$) is equal to that of the total cathodic current ($I_{total,\ cathodic}$) in a reaction.[28]

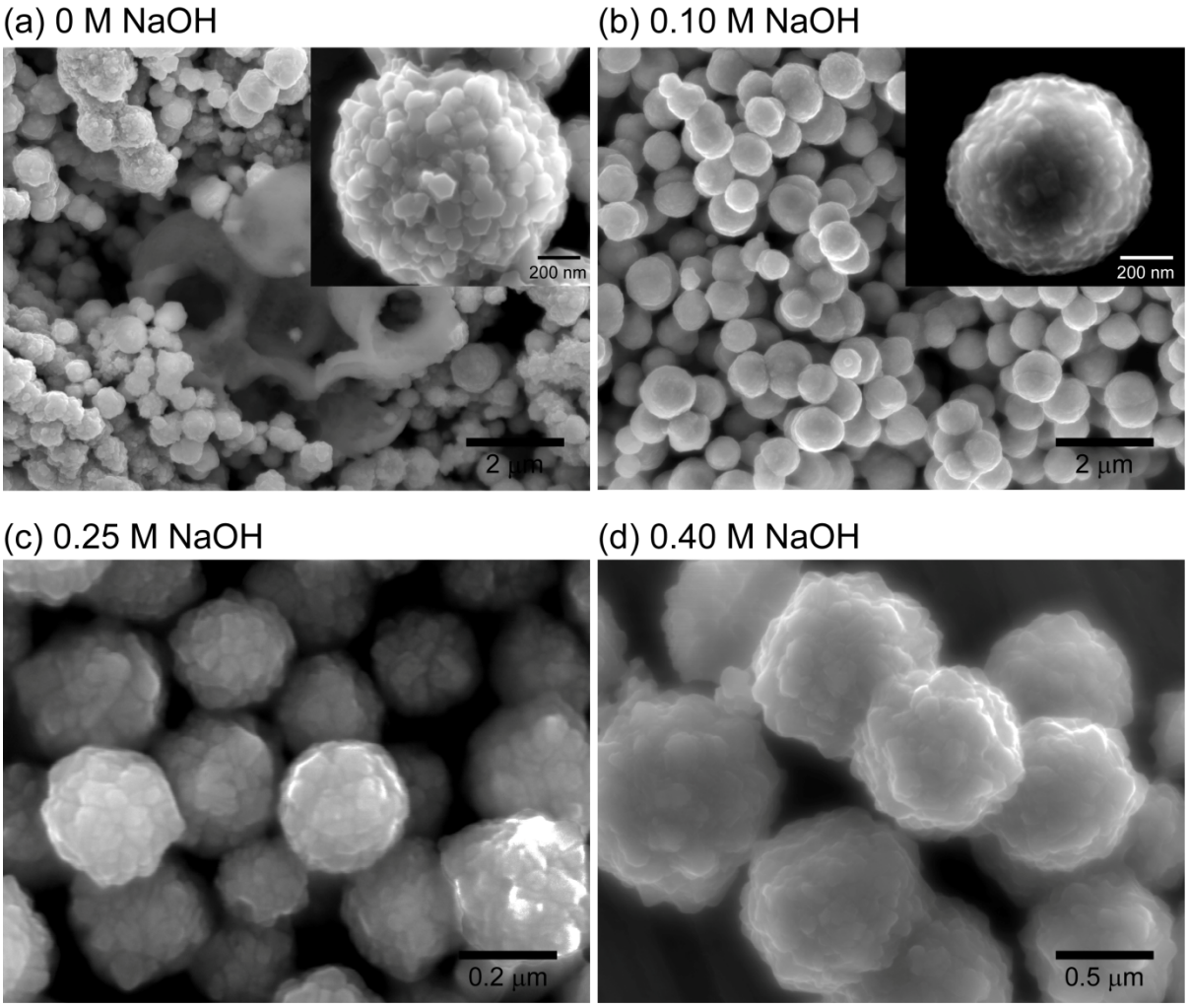

Figure 2.3 SEM images of Co particles prepared by electroless deposition in PG solutions with 0.10 M Co(II) acetate and (a) 0, (b) 0.10, (c) 0.25, and (d) 0.40 M NaOH. The Co particles have a mean diameter of about (a) 1.0, (b) 0.70, (c) 0.30, and (d) 0.50 μm.

Table 2.1 List of crystallite and particle sizes determined by XRD and SEM, respectively, for Co particles prepared with increasing concentration of NaOH.

	NaOH Concentration,M			
	0	0.10	0.25	0.40
XRD				
2theta/ degree	68.337	68.366	68.349	68.213
Crystallite size/ nm	26.0	16.2	15.9	17.8
SEM				
Average particle size/ μm	1.0	0.70	0.30	0.50

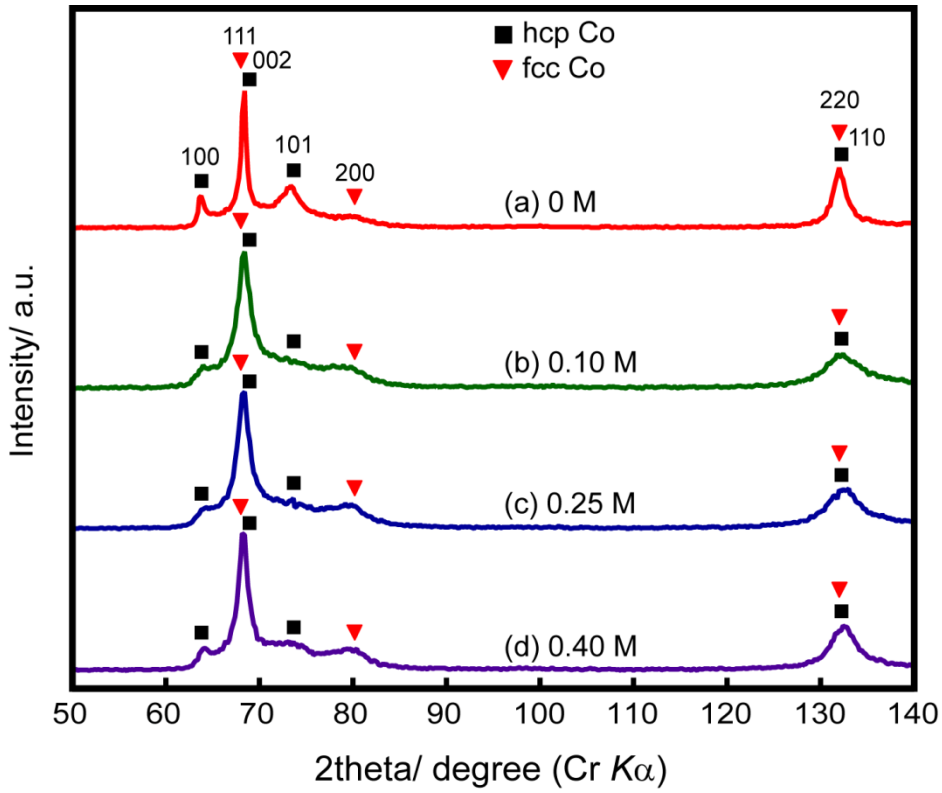

Figure 2.4 XRD patterns of Co particles prepared by electroless deposition in PG solutions with 0.10 M Co(II) acetate and (a) 0, (b) 0.10, (c) 0.25, and (d) 0.40 M NaOH. The Co particles have a mean diameter of about (a) 1.0, (b) 0.70, (c) 0.30, and (d) 0.50 μm.

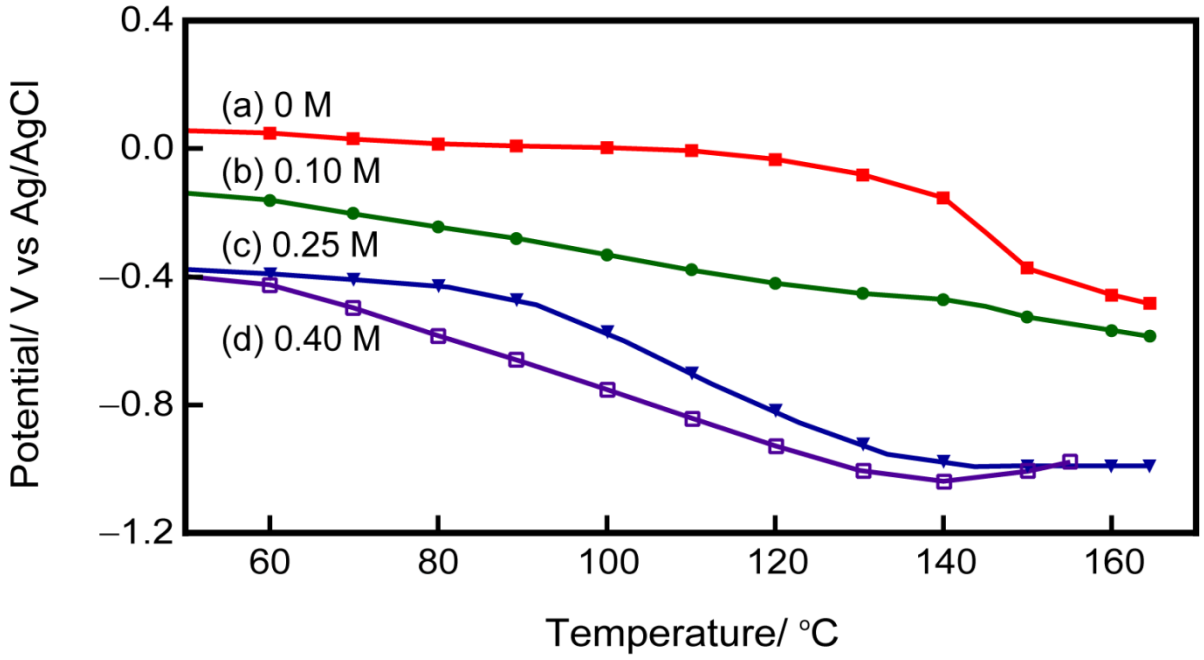

Figure 2.5 Change in mixed potential with temperature up to the boiling point (155 - 165 ºC) in PG solutions containing (a) 0, (b) 0.10, (c) 0.25, and (d) 0.40 M NaOH. 0.10 M $LiClO_4$ is added as supporting electrolyte.

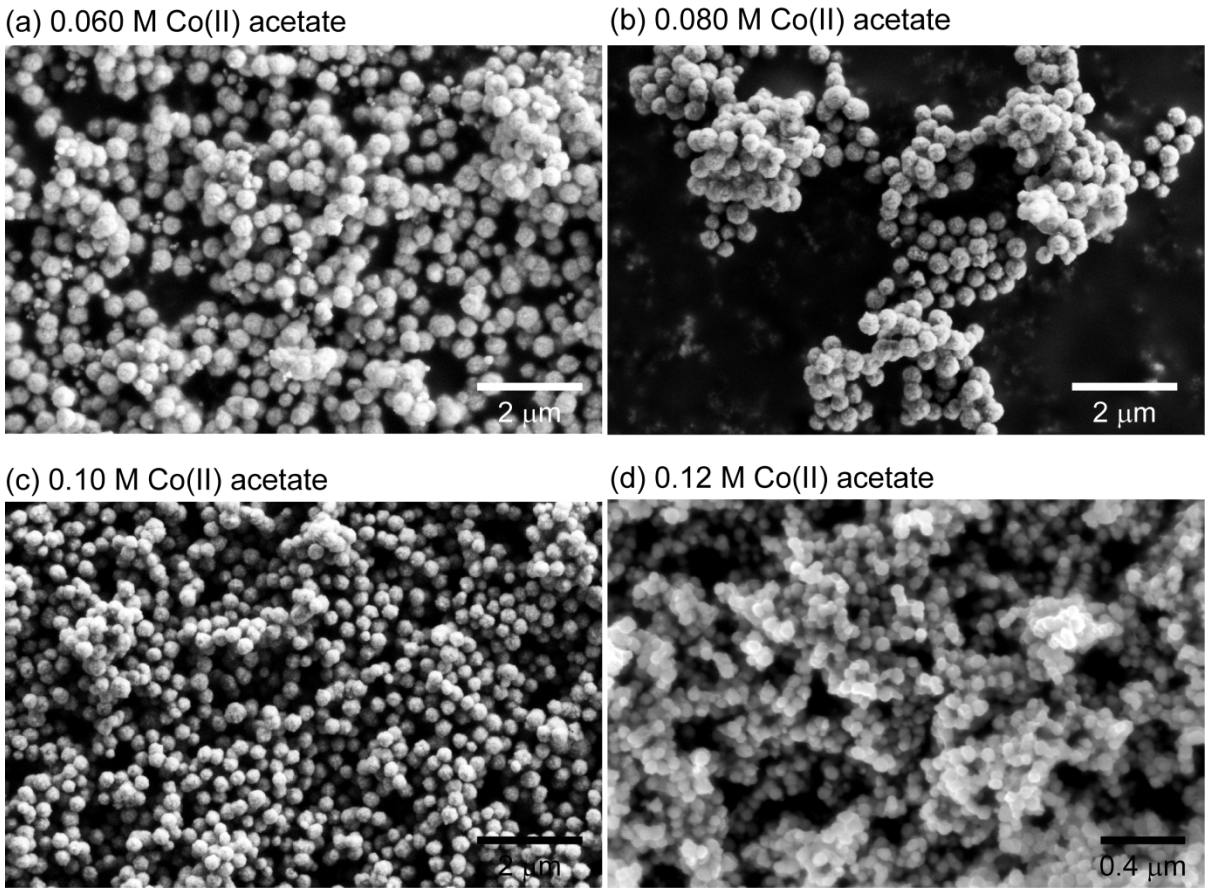

Figure 2.6 SEM images of Co particles prepared by electroless deposition using (a) 0.060 M, (b) 0.080 M, (c) 0.10 M, and (d) 0.12 M Co (II) acetate. The mean diameters of Co particles are (a) 388, (b) 364, and (c) 300, and (d) 152 nm. The concentration of NaOH is 0.25 M.

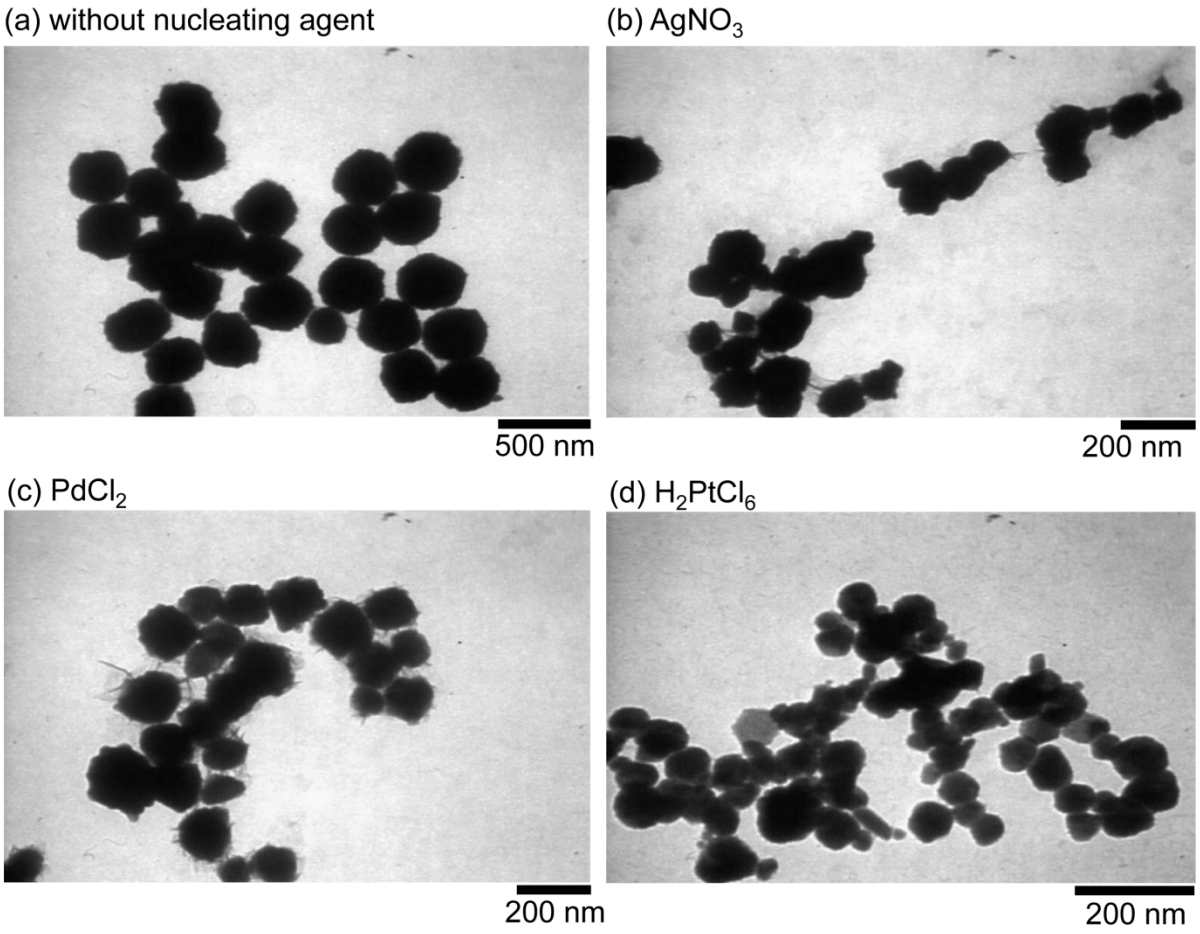

Figure 2.7 TEM images of Co particles prepared (a) without any nucleating agent and by nucleating with 2.5 mM (b) $AgNO_3$, (c) $PdCl_2$, and (d) H_2PtCl_6. The mean diameters of Co particles are (a) 300, (b) 106, (c) 121, and (d) 61 nm. The PG solutions contain 0.10 M Co(II) acetate and 0.25 M NaOH.

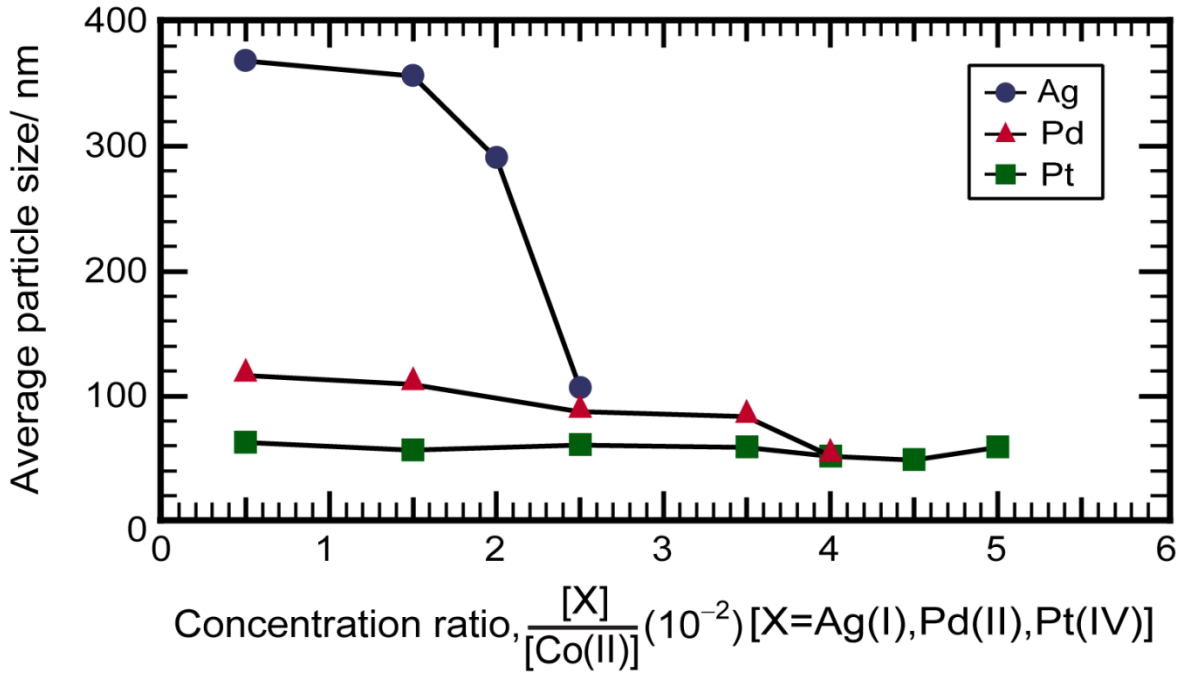

Figure 2.8 Change in the average particle size of the Co particles with increasing concentrations of nucleating agents ($AgNO_3$, $PdCl_2$, and H_2PtCl_6). The PG solutions contain 0.10 MCo(II) acetate and 0.25 M NaOH.

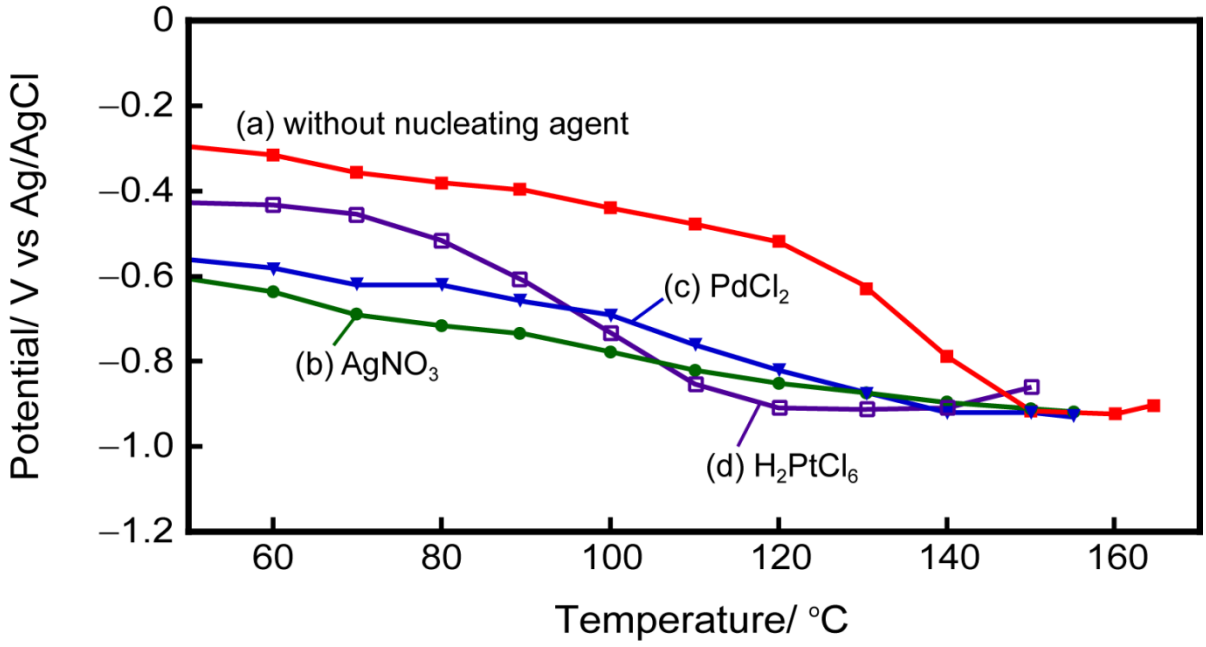

Figure 2.9 Change in mixed potential with temperature up to the boiling point (150 - 165 ºC) measured in PG solutions (a) without any nucleating agent, and with 2.5 mM (b) $AgNO_3$, (c) $PdCl_2$, and (d) H_2PtCl_6. The PG solutions contain 0.10 M Co(II) acetate, 0.25 M NaOH, and 0.10 M $LiClO_4$ as supporting electrolyte.

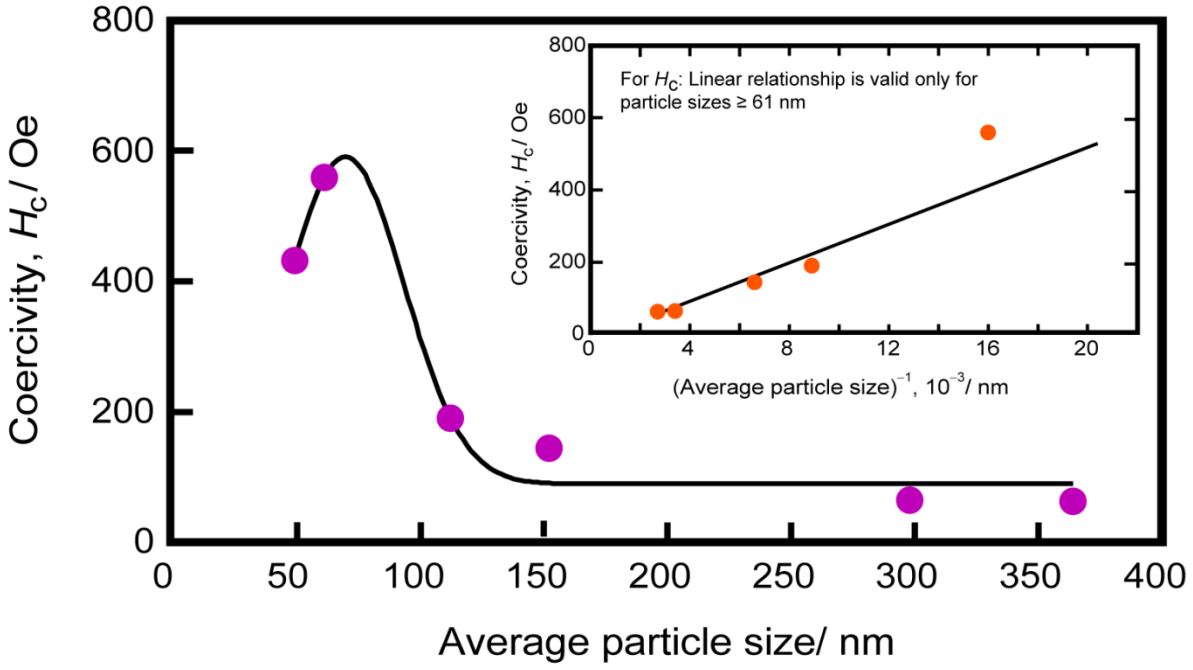

Figure 2.10 Coercivity (H_c, Oe) at room temperature plotted vs the average particle size of Co particles. Inset shows the linear relationship of H_c and the inverse of the average particle size of the Co particles with diameters ≥ 61 nm.

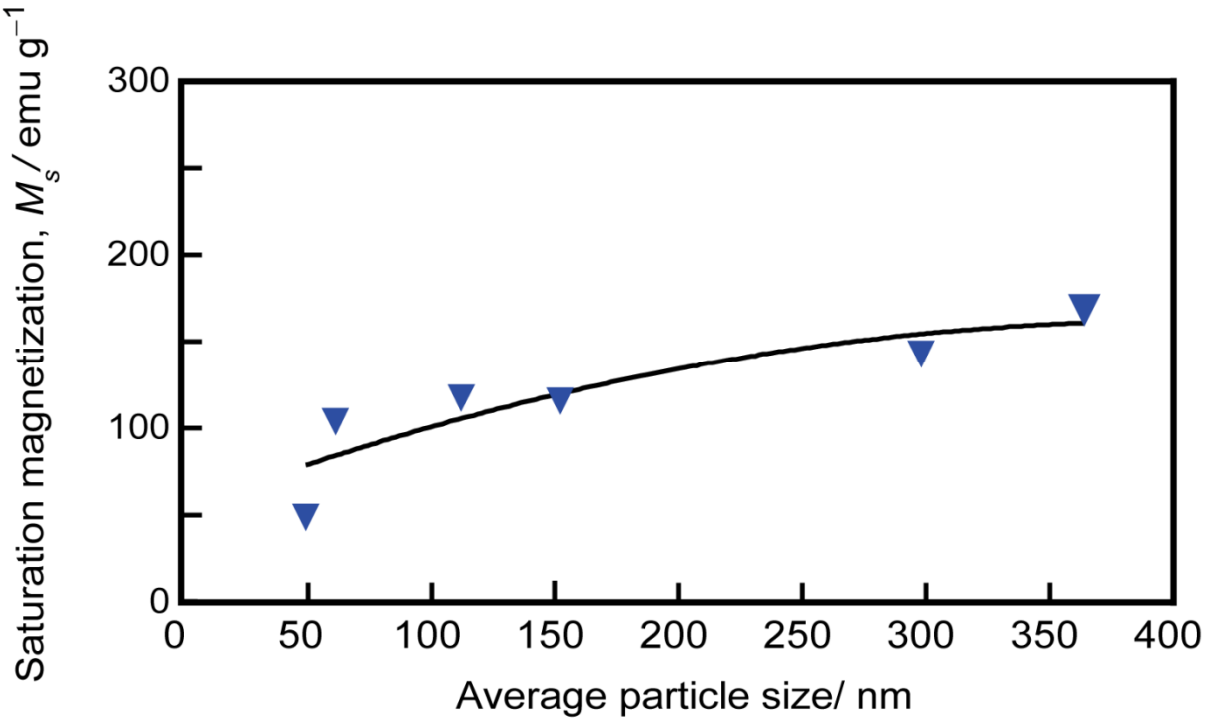

Figure 2.11 Saturation magnetization (M_s, emu g^{-1}) at room temperature plotted against the average particle size of Co particles.

References

1. F. Fiévet, J.-P. Lagler, B. Blin, B. Beaudoin, and M. Figlarz, "Homogeneous and Heterogeneous Nucleation in the Polyol Process for the Preparation of Micron and Submicron Size Metal Particles", *Solid State Ionics*, **32-33**, 198 (1989).

2. F. Fiévet, F. Fiévet-Vincent, J.-P. Lagler, B. Dumont, and M. Figlarz, "Controlled Nucleation and Growth of Micrometer-Size Copper Particles Prepared by the Polyol Process", *J. Mater. Chem.,* **3**, 627 (1993).

3. L. K. Kurihara, G. M. Chow, and P. E. Schoen, "Nanocrystalline Metallic Powders and Films Produced by the Polyol Method", *Nanostructured Mater.,* **6**, 607 (1995).

4. G. Viau, F. Fiévet-Vincent, and F. Fiévet, "Nucleation and Growth of Bimetallic CoNi and FeNi Monodisperse Particles Prepared in Polyols", *Solid State Ionics*, **84**, 259 (1996).

5. C. Luna, M. Morales, C. J. Serna, and M. Vazquez, "Exchange Anisotropy in $Co_{80}Ni_{20}$/Oxide Nanoparticles", *Nanotech.,* **15**, S293 (2004).

6. T. Hinotsu, B. Jeyadevan, C. N. Chinnasamy, K. Shinoda, and K. Tohji, "Size and Structure Control of Magnetic Nanoparticles by Using a Modified Polyol Process", *J. Appl. Phys.,* **95**, 7477 (2004).

7. Y. Sun, Y. Yin, B. T. Mayers, T. Herricks, and Y. Xia, "Uniform Silver Nanowires Synthesis by Reducing $AgNO_3$ with Ethylene Glycol in the Presence of Seeds and Poly(Vinyl Pyrrolidone)", *Chem. Mater.,* **14**, 4736 (2002).

8. D. Ung, G. Viau, F. Fiévet-Vincent, F. Herbst, V. Richards, and F. Fiévet, "Magnetic Nanoparticles with Hybrid Shape", *Progress in Solid State Chemistry,* **33**, 137 (2005).

9. Q. Liu, C. Guo, J. Chen, W. Song, and W. Shen, "Cobalt Nanowires Prepared by Heterogeneous Nucleation in Propanediol and their Catalytic Properties", *Nanotech.,* **19**, 365806 (2008).

10. N. Chakroune, G. Viau, C. Ricolleau, F. Fiévet-Vincent, and F. Fiévet, "Cobalt-Based Anisotropic Particles Prepared by the Polyol Process", *J. Mater. Chem.,* **13**, 312 (2003).

11. M. S. Hegde, D. Larcher, L. Dupont, B. Beaudoin, K. Tekaia-Elhsissen, and J. M. Tarascon, "Synthesis and Chemical Reactivity of Polyol Prepared Monodisperse Nickel Powders", *Solid State Ionics*, **93**, 33 (1997).

12. G. Viau, F. Fiévet-Vincent, and F. Fiévet, "Monodisperse Iron-Based Particles: Precipitation in Liquid Polyols", *J. Mater. Chem.,* **6**, 1047 (1996).

13. R. J. Joseyphus, D. Kodama, T. Matsumoto, Y. Sato, B. Jeyadevan, and K. Tohji, "Role of Polyol in the Synthesis of Fe Particles", *J. Magn. Magn. Mater.,* **310**, 2393 (2007)

14. P.-Y. Silvert, R. Herrera-Urbina, and K. Tekaia-Elhsissen, "Preparation of Colloidal Silver Dispersions by the Polyol Process Part 2-Mechanism of Particle Formation", *J. Mater. Chem.,* **7**, 293 (1997).

15. R. M. Rioux, H. Song, M. Grass, S. Habas, K. Niesz, J. D. Hoefelmeyer, P. Yang, and G. A. Somorjai, "Monodisperse Platinum Nanoparticles of Well-Define Shape: Synthesis, Characterization, Catalytic Properties and Future Prospects", *Topics in Catalysis,* **39**, 167 (2006).

16. D. Kodama, K. Shinoda, K. Sato, Y. Sato, B. Jeyadevan, and K. Tohji, "Synthesis of Size-Controlled Fe-Co Alloy Nanoparticles by Modified Polyol Process", *J. Magn. Magn. Mater.,* **310**, 2396 (2007)

17. D. Ung, G. Viau, C. Ricolleau, F. Warmont, P. Gredin, and F. Fiévet, "CoNi Nanowires Synthesized by Heterogeneous Nucleation in Liquid Polyol", *Adv. Mater.* **17**, 338 (2005).

18. B. Jeyadevan, K. Urakawa, A. Hobo, N. Chinnasamy, K. Shinoda, K. Tohji, D. D. J. Djayaprawira, M. Tsunoda, and M. Takahashi, "Direct Synthesis of Fct-FePt Nanoparticles by Chemical Route", *Jpn. J. Appl. Phys.,* **42**, L350 (2003).

19. C. N. Chinnasamy, B. Jeyadevan, K. Shinoda, and K. Tohji, "Polyol-Process-Derived CoPt Nanoparticles: Structural and Magnetic Properties", *J. Appl. Phys.,* **93**, 7583 (2003).

20. F. Bonet, C. Guéry, D. Guyomard, R. Herrera Urbina, K. Tekaia-Elhsissen, and J. M. Tarascon, "Electrochemical Reduction of Noble Metal Species in Ethylene Glycol at Platinum and Glassy Carbon Rotating Disk Electrodes", *Solid State Ionics,* **126**, 337 (1999).

21. F. Bonet, C. Guéry, D. Guyomard, R. Herrera Urbina, K. Tekaia-Elhsissen, and J. M. Tarascon, "Electrochemical Reduction of Noble Metal Compounds in Ethylene Glycol", *Intl. J. Inorganic Mater.,* **1**, 47 (1999).

22. S. Yagi, M. Kawamori, and E. Matsubara, "Electrochemical Study on the Synthesis Process of Co-Ni Alloy Nanoparticles via Electroless Deposition", *J. Electrochem. Soc.,* **155**, E92 (2010).

23. S. Yagi, M. Kawamori, and E. Matsubara, "Electrochemical QCM Study on the Synthesis Process of Co Nanoparticles via Electroless Deposition", *Electrochem. Solid-State Lett.,* **13**, E1 (2010).

24. R. J. Joseyphus, T. Matsumoto, H. Takahashi, D. Kodama, K. Tohji, and B. Jeyadevan, "Designed Synthesis of Cobalt and its Alloys by Polyol Process", *J. Solid State Chem.,* **180**, 3008 (2007).

25. T. S. Davoy, J. E. Jackson, G. M. Swain, D. J. Miller, J. Li, and J. Lipkowski, "Mild Electrocatalytic Hydrogenation of Lactic Acid to Lactaldehyde and Propylene Glycol", *J. Catalysis,* **246**, 15 (2007).

26. S. Demirel, P. Kern, M. Lucas, and P. Claus, "Oxidation of Mono- and Polyalcohols with Gold: Comparison of Carbon and Ceria Supported Catalysts", *Catalysis Today,* **122**, 292 (2007).

27. D. Larcher and R. Patrice, "Preparation of Metallic Powders and Alloys in Polyol Media: A Thermodynamic Approach", *J. Solid State Chem.,* **154**, 405 (2000).

28. E. M. Pater and S. Bruckenstein, "Determining the Thermodynamic Electrode Potential in the Presence of a Mixed Potential using EQCM Technique", *Electrochem. Comm.,* **5**, 958 (2003).

29. S. Yagi, T. Koyanagi, H. Nakanishi, T. Ichitsubo, and E. Matsubra, "Formation of Nickel Nanoparticles by Electroless Deposition Using NiO and $Ni(OH)_2$ Suspensions", *J. Electrochem. Soc.,* **155**, D583 (2008).

30. S. Yagi, H. Nakanishi. E. Matsubara, S. Matsubara, T. Ichitsubo, K. Hosoya, and Y. Matsuba, "Formation of Cu Nanoparticles by Electroless Deposition Using Aqueous Cu Suspension", *J. Electrochem. Soc.,* **155**, D474 (2008).

31. S. Yagi, H. Nakanishi. T. Ichitsubo, and E. Matsubara, "Oxidation-State Control of Nanoparticles Synthesized via Chemical Reduction Using Potential Diagramsn", *J. Electrochem. Soc.,* **156**, D321 (2009).

32. T. Sugimoto, *Monodispersed Particles,* Elsevier, Amsterdam (2001).

33. G. Cao, *Nanostructures and Nanomaterials: Synthesis, Properties and Applications,* Imperial College Press, London (2004).

34. G. Viau, P. Toneguzzo, A. Pierrard, O. Archer, F. Fiévet-Vincent, and F. Fiévet, "Heterogeneous Nucleation and Growth of Metal Nanoparticles in Polyols", *Scripta Materialia*, **44**, 2263 (2001).

35. B. D. Cullity, *Introduction to Magnetic Materials,* Addison-Wesley Publishing Company, London (1972).

36. R. H. Kodama, "Magnetic Nanoparticles", *J. Magn. Magn Mater*. **200**, 359 (1999).

37. X. Batlle and A. Labarta, "Finite-Size Effects in Fine Particles: Magnetic and Transport Properties", *J. Phys. D: Appl. Phys*. **35**, R15 (2002).

Chapter III Modification of Electroless Deposition for Synthesis of Co Nanoparticles at Room Temperature

3.1 Introduction

The synthesis of Co nanoparticles in an aqueous solution at room temperature is attractive since it is simple, low cost, and easily scalable for industrial production. Such process is, however, still challenging because of the difficulty of formation of size-controlled Co nanoparticles without agglomeration and oxidation. The reducing agent, such as sodium borohydride, can reduce Co(II) at room temperature.[1-3] But the synthesized Co nanoparticles are usually polydispersed and amorphous due to contamination with boron.

This chapter presents a method of preparation of Co nanoparticles with diameters of 24 - 500 nm by electroless deposition in an aqueous solution at room temperature. Hydrazine (N_2H_4) is used as reducing agent so that contamination of the Co products is prevented, while hexachloroplatinic acid hexahydrate ($H_2PtCl_6 \cdot 6H_2O$) is employed as the nucleating agent based on the results of Chapter II. The formation of Co nanoparticles is investigated by in-situ mixed potential measurements in conjunction with quartz crystal microbalance. The effects of the addition of H_2PtCl_6 with different NaOH and N_2H_4 concentrations on the particle growth and reaction rate are studied by electron microscopy, X-ray diffraction, and linear sweep voltammetry. The oxidation and reduction potentials of N_2H_4 and Co are separately evaluated from anodic and cathodic polarization curves, respectively. Based on the electrochemical study, a formation mechanism of Co nanoparticles is proposed.

3.2 Experimental

All chemical reagents were analytical grade. In a typical experiment, Co(II) solution and reducing agent solution were prepared separately. First, 1.0 x 10^{-2} mol Co(II) acetate tetrahydrate, 1.3 x 10^{-3} mmol polyethylene glycol [PEG, $H(OCH_2CH_2)nOH$, M_w = 20,000], and 2.5 x 10^{-2} mol NaOH were dissolved in 75 cm^3 distilled water while nitrogen gas (N_2) was bubbled at 50 cm^3 min^{-1}. Then, 2.5 x 10^{-2} mmol $H_2PtCl_6 \cdot 6H_2O$ in 10 cm^3 propylene glycol (PG) solution was added as a nucleating agent. On the other hand, 1.0 x 10^{-1} mol (5.0 cm^3) hydrazine monohydrate ($N_2H_4 \cdot H_2O$) was dissolved in 25 cm^3 deaerated PG. The two solutions were then mixed vigorously at room temperature. The final solution had a total volume of 115 cm^3 and the final concentrations of the reagents were 87 mM Co(II) acetate, 1.1 mM PEG, 0.22 M NaOH, 0.22 mM H_2PtCl_6, and 0.87 M N_2H_4. After 1 h, Co nanoparticles were magnetically separated and washed several times with ethanol.

The morphology of Co nanoparticles was observed by a field-emission scanning electron microscope (JEOL JSM 6500-F) and a transmission electron microscope (TEM, JEOL JEM 2010). The mean diameter was determined by image analysis of 300 nanoparticles in each sample. The structure was analyzed by X-ray diffraction (XRD) using Cr *K*α radiation (MAC Science M03XHF22). Electrochemical measurements of mixed potentials and polarization curves were conducted using a potentiostat/galvanostat (Hokuto Denko Co. Ltd., HA-151). The working and reference electrodes were 9 MHz AT-cut Pt-sputtered quartz crystal substrates and a Ag/AgCl electrode (Horiba 2565-10T), respectively. A Pt sheet was used as a counter electrode only during linear sweep voltammetry. Mixed potentials measured in an aqueous solution were reported against the standard electrode potential (SHE). In pure PG solution, the potentials were referred to the potential of the

Ag/AgCl electrode. The resonance frequency shift during linear sweep voltammetry was measured by Seiko EG&G quartz crystal microbalance (QCM, QCA 917). The effective mass deposited on the substrate, Δm, was calculated from the change in the resonance frequency, Δf, by the Sauerbrey equation:

$$\Delta f = -\left[\frac{2 f_0^2}{A\sqrt{\rho_Q \mu_Q}}\right]\Delta m \qquad (3\text{-}1)$$

where f_0 is the frequency of the Pt-sputtered quartz crystal substrate before deposition, A the piezo-electrically active area of the substrate, ρ_Q the density of quartz (2.648 g cm^{-3}), and μ_Q the shear modulus of quartz (2.947 x 10^{11} g cm^{-1} s^{-2}).

3.3 Electrochemical consideration of Co deposition and hydrazine oxidation

3.3.1 Determination of the activity of Co^{2+} aquo ions

When the Co ionic source Co(II) acetate dissolves in water in the presence of abundant OH^- ions, Co^{2+} aquo ions are released into the solution and hydrolyzed to form solid Co(II) hydroxide ($Co(OH)_2$). When the Co^{2+} aquo ions are in equilibrium with $Co(OH)_2$, the reaction is written as follows:

$$Co^{2+} + 2H_2O \leftrightarrow Co(OH)_2 + 2H^+ \qquad (3\text{-}2)$$

From Equation (3-2), the activity of Co^{2+} aquo ions in the solution depends on the concentration of H^+ ions. Thus, the activity of Co^{2+} aquo ions ($a_{Co^{2+}}$) can be expressed as

function of the solution pH. Since the change in Gibbs free energy of Equation (3-2) is equal to zero under an equilibrium state at 298 K, $a_{Co^{2+}}$ is determined as follows:

$$\Delta G = \Delta G° + RT \ln\left(\frac{a_{Co(OH)_2} \cdot a_{H^+}^2}{a_{Co^{2+}} \cdot a_{H_2O}^2}\right) = 0$$

$$\Delta G° = \mu^o_{Co(OH)_2} + 2\mu^o_{H^+} - \mu^o_{Co^{2+}} - 2\mu^o_{H_2O}$$

$$a_{Co^{2+}} = (8.16 \times 10^{12}) \times (10^{-\mathrm{pH}}) \tag{3-3}$$

where ΔG is the change in Gibbs free energy of the reaction (J mol^{-1}), R is the gas constant (8.314 J mol^{-1} K^{-1}), T is the temperature (298 K), μ° is the standard chemical potential of a chemical species presented in the subscript, and a is the activity of a chemical species written in the subscript. In the present work, the activities of $Co(OH)_2$ [$a_{Co(OH)_2}$] and H_2O (a_{H_2O}) are taken as unity since they are pure substances. Using the standard Gibbs free energy of formation of each chemical species in Table 3.1, $a_{Co^{2+}}$ at a certain pH value is calculated using Equation (3-3). $a_{Co^{2+}}$ drastically decreases with increasing pH as it is seen in Fig. 3.1.

3.3.2 Determination of the oxidation-reduction potential of the Co(II)/Co redox pair

In the case of metal Co in equilibrium with Co^{2+} aquo ions in the solution, the equilibrium reaction between the Co^{2+}/Co redox pair is written as:

$$Co^{2+} + 2e^{-} \leftrightarrow Co \tag{3-4}$$

Since only the difference in potential (E) can be measured, a reference electrode is required to determine the oxidation-reduction potential of the Co^{2+}/Co redox pair ($E_{Co^{2+}/Co}$). When $E_{Co^{2+}/Co}$ is determined with respect to standard hydrogen electrode (SHE), it is necessary to combine Equation (3-4) with the equilibrium reaction for the H^{+}/H_2 redox pair.

$$2H^{+}_{(SHE)} + 2e^{-} \leftrightarrow H_{2(SHE)} \tag{3-5}$$

Thus, the equilibrium reaction for the Co^{2+}/Co redox pair against SHE is given below:

$$Co^{2+} + H_{2(SHE)} \leftrightarrow Co + 2H^{+}_{(SHE)} \tag{3-6}$$

The change in Gibbs free energy of the above reaction is written as:

$$\Delta G = \mu^{o}_{Co} + 2\mu^{o}_{H^{+}_{(SHE)}} - \mu^{o}_{Co^{2+}} - \mu^{o}_{H_2(SHE)} + RT\ln\left(\frac{a_{Co}\cdot a^{2}_{H^{+}_{(SHE)}}}{a_{Co^{2+}}\cdot P_{H_{2(SHE)}}}\right)$$

$$= \mu^{o}_{Co} + 2\mu^{o}_{H^{+}_{(SHE)}} - \mu^{o}_{Co^{2+}} - \mu^{o}_{H_2(SHE)} + RT\ln\left(\frac{1}{a_{Co^{2+}}}\right) \tag{3-7}$$

Because metal Co is a pure solid substance, a_{Co} is equal to 1. On the other hand, $a_{H^+_{(SHE)}}$ and the partial pressure of H_2 ($P_{H_{2(SHE)}}$, atm) are taken as 1. By substituting $a_{Co^{2+}}$ calculated at a certain pH using Equation (3-3) into (3-7), the change in Gibbs free energy of Equation (3-6) is determined.

The Gibbs free energy change is related to $E_{Co^{2+}/Co}$ by the following equation:

$$\begin{aligned} \Delta G &= -nFE_{Co^{2+}/Co} \\ &= -2FE_{Co^{2+}/Co} \end{aligned} \tag{3-8}$$

where n is the number of mole of electrons exchanged in the reaction and F is the Faraday's constant (96,485 C mol^{-1}). The change in $E_{Co^{2+}/Co}$ with increasing pH is depicted in Fig. 3.2; $E_{Co^{2+}/Co}$ shifts to more negative potentials with increase in pH. It should be noted that other Co deposition reactions, such as the direct reduction of $Co(OH)_2$ to Co, can also occur in the solution. Nonetheless, the oxidation-reduction potential of the $Co(OH)_2$/Co redox pair ($E_{Co(OH)_2/Co}$) at a certain pH value is equal to $E_{Co^{2+}/Co}$. For example, E is about –0.62 V at pH 12 for all Co(II)/Co redox pairs, where Co(II) includes every Co(II) species, e.g. Co^{2+}, $Co(OH)_2$, $HCoO_2^-$ or $Co(OH)_3^-$, CoO_2^{2-} and $Co(OH)_4^{2-}$. Therefore, $E_{Co^{2+}/Co}$ can be rewritten as $E_{Co(II)/Co}$.

3.3.3 Determination of the oxidation-reduction potential of the N_2/N_2H_4 redox pair

When Co(II) ions are reduced in the solution, the reducing agent hydrazine (N_2H_4) is simultaneously oxidized. The equilibrium reaction for the N_2/N_2H_4 redox pair is as follow:

$$N_2 + 4H^+ + 4e^- \leftrightarrow N_2H_4 \tag{3-9}$$

The equilibrium reaction for the N_2/N_2H_4 redox pair must be combined with the equilibrium reaction for H^+/H_2 redox pair in order to determine the oxidation-reduction potential vs SHE. Therefore, Equations (3-9) is rewritten as:

$$N_2 + 4H^+ + 2H_{2(SHE)} \leftrightarrow N_2H_4 + 4H^+_{(SHE)} \tag{3-10}$$

The change in Gibbs free energy in the reaction of (3-10) is:

$$\Delta G = \mu^o_{N_2H_4} + 4\mu^o_{H^+_{(SHE)}} - \mu^o_{N_2} - 4\mu^o_{H^+} - 2\mu^o_{H_2(SHE)} + RT\ln\left(\frac{a_{N_2H_4}\cdot a^4_{H^+_{(SHE)}}}{P_{N_2}\cdot a^4_{H^+}\cdot P^2_{H_2(SHE)}}\right)$$

$$= -4FE_{N_2/N_2H_4} \tag{3-11}$$

The values of E_{N_2/N_2H_4} is evaluated from the thermodynamic data in Table 3-1, and then substituting the values of the activities and partial pressures for the chemical species in the expression. Both $a_{H^+_{(SHE)}}$ and $P_{H_2(SHE)}$ are equal to unity. Because N_2 gas flows during the reaction, P_{N_2} is equated to 1. $a_{N_2H_4}$ is set to be equal to the concentration of N_2H_4. Figure 3.3

shows the change in E_{N_2/N_2H_4} with increasing pH when $a_{N_2H_4}$ is equal to 0.87 M. E_{N_2/N_2H_4} is decreased at higher pH.

3.4 Results and Discussion

3.4.1 Electroless deposition of Co nanoparticles in an aqueous solution

Figure 3.4 shows the XRD patterns of Co products for different reaction times at room temperature. Using water as a solvent, the reaction is conducted under similar conditions explained in Chapter II. Since PG could not reduce Co(II) at room temperature, a stronger reducing agent, i.e. N_2H_4, is employed. The N_2H_4/Co(II) acetate concentration ratio is initially set to 10, and the solution reaches a pH value of about 12 after mixing the Co(II) and N_2H_4 solutions. Diffraction peaks attributed to both hcp and fcc Co structures are observed in the XRD profiles. The small Co peaks at 63.8° and 73.6° are 100 and 101 hcp Co, respectively. The diffused peak at 80.5° is characteristic of 200 fcc Co. The strongest peak at 68.0° is due to 111 fcc Co, whereas the shoulder to the right of the 111 peak is 002 hcp. The Co peaks are very broad, implying small crystallite sizes.

Diffused $Co(OH)_2$ peaks at 57.7°, 58.9°, and 80.2° are determined on the sample prepared after 5 min reaction time. SEM images of the precipitates in Fig. 3.5(a) show 2 distinct morphologies, namely: spherical nanoparticles of about 44 nm diameter and lamellar precipitates about 100 nm thick and 0.50 - 1.0 μm wide. When the reaction proceeds to 10 min, only spherical nanoparticles of about 52 nm mean diameter are present as seen in Fig. 3.5(b). $Co(OH)_2$ peaks are also not observed in the XRD pattern. Therefore, the broad $Co(OH)_2$ peaks are possibly due to poorly crystallized lamella formed as an intermediate solid phase. Longer reaction time results in a slight increase in particle size of Co. Thus,

almost all Co(II) are reduced after about 20 min. The synthesized Co nanoparticles are slightly agglomerated owing to their strong magnetic attraction.

Figure 3.6(a) shows the change in mixed potential during electroless deposition of Co in an aqueous solution of pH 12 at room temperature. At the beginning of the reaction, the mixed potential is more positive than the oxidation-reduction potential of Co(II)/Co [$E_{Co(II)/Co}$ = –0.62 V vs standard hydrogen electrode (SHE)]. Naturally, no Co nanoparticles are formed. When the reaction reaches about 3 min, the mixed potential drops below $E_{Co(II)/Co}$. This initiates the change in solution color from blue to black. The transition in the mixed potential coincides with the change in morphology and structure of the products in Fig. 3.4(a) and 3.5(a). The mixed potential remains almost constant up to about 20 min. Black precipitates appear in the solution, and a significant amount of gas is simultaneously released. Therefore, as N_2H_4 is consumed, the mixed potential is gradually increased due to the reduction in the total anodic current.[5-6]

The corresponding change in the deposited mass is shown in Fig. 3.6(b). Initially, Δm slowly increases until about 3 min. Since the mixed potential is larger than $E_{Co(II)/Co}$ at this time, no Co deposition occurs. Possibly, some solid $Co(OH)_2$ adheres on the surface of the electrode. When the mixed potential shifts below $E_{Co(II)/Co}$, the adsorbed $Co(OH)_2$ is possibly reduced and Δm decreases. At about 20 min, a sharp increase in Δm is observed, which coincides with the endpoint of the reaction evaluated from the mixed potential.

To understand the reduction of Co(II), the cathodic current coupled with the effective mass change was measured in an aqueous solution with 87 mM Co(II) acetate, 0.22 M NaOH, and 0.10 M sodium sulfate (Na_2SO_4) as a supporting electrolyte. The total volume was 115 cm^3 with a pH of about 12. Figure 3.7(a) is the linear sweep voltammogram

measured at 1 mV s^{-1} from the rest potential of 0.20 V up to −1.0 V vs SHE. The cathodic current is observed at about −0.73 V vs SHE, which is more negative than the calculated $E_{Co(II)/Co}$ and the oxidation-reduction potential of the H_2O/H_2 redox pair (E_{H_2O/H_2} = −0.53 V at pH 12, $P_{H_2} = 10^{-6}$). This suggests that Co deposition and H_2 generation concomitantly occur during the reaction. Thus, the pH near the electrode surface increases, which promotes the deposition of $Co(OH)_2$. The mass change during the cathodic polarization is shown in Fig. 3.7(b). A positive Δm of about 1.0 x 10^{-2} μg is observed immediately after immersing the Pt-sputtered QCM substrate into the solution. While the current density remains zero from −0.20 to −0.73 V, Δm is slowly increased as the potential decreases. This indicates that non-faradaic deposition indeed occurs before Co(II) reduction, which agrees with the QCM measurement in Fig. 3.6(b). Below −0.80 V, Δm significantly increases. This implies faster Co deposition at more negative potentials.

3.4.2 Effect of addition of increasing amount of H_2PtCl_6

Figure 3.8 shows the mixed potentials measured in aqueous solutions containing different concentrations of H_2PtCl_6. H_2PtCl_6 is used as nucleating agent based on the results of Chapter II. Because the mixed potentials without H_2PtCl_6 are fluctuated, their average values are plotted in Fig. 3.8(a). The instability of the mixed potential is due to very small cathodic and anodic current densities during the reaction. The average values are obviously much higher than $E_{Co(II)/Co}$ throughout the reaction. Consequently, no Co nanoparticles are formed even after 2 h.

In contrast, the mixed potential shifts more negatively with an increase in the concentration of H_2PtCl_6, and the reduction of Co(II) occurs faster. In the presence of 2.2 x

10^{-2} mM H_2PtCl_6, the mixed potential drops to $E_{Co(II)/Co}$ about 7 min after the addition of the reducing agent N_2H_4. The color of the solution then changes to black. At 0.22 mM H_2PtCl_6, the mixed potential is equal to $E_{Co(II)/Co}$ after about 3 min. Adding more H_2PtCl_6 results in an instantaneous drop of the mixed potential below $E_{Co(II)/Co}$, and a spontaneous change in the color of the solution. Because of the acceleration of the reaction rates with higher amounts of H_2PtCl_6, it is plausible that the Pt nanoparticles formed from H_2PtCl_6 act as catalysts for Co(II) reduction, as well as nucleation sites for Co nanoparticles.[4-5,7]

To elucidate the influence of H_2PtCl_6 on the reaction rate, the change in mixed potential during Pt deposition is observed. Except for Co(II) acetate, the aqueous solutions contain the same concentration of reactants as those used during the synthesis of Co nanoparticles (0.22 M NaOH, 1.1 mM PEG, and 0.87 M N_2H_4). Figure 3.9 shows lower mixed potential with an increase in the concentration of H_2PtCl_6. It has been reported that N_2H_4 is catalytically oxidized on the surface of Pt nanoparticles.[8] Therefore, the decrease in the mixed potential with larger concentration of H_2PtCl_6 is explained by considering that the mixed potential is mainly controlled by a change in the current density for N_2H_4 oxidation. The oxidation of N_2H_4 is generally slow at room temperature, but the addition of H_2PtCl_6 accelerates the reaction due to the catalytic activity of the Pt nanoparticles. The anodic current density therefore increases, which lowers the mixed potential. At the same time, the reduction of Co(II) occurs more readily owing to the enhanced oxidation of N_2H_4 at higher amounts of H_2PtCl_6. As a result, small Co nanoparticles are immediately formed.

Since H_2 generation and Co deposition simultaneously occur, a large amount of evolved gases is expected particularly due to the presence of Pt nanoparticles. On the other hand, the strong H_2 generation after the precipitation of Co nanoparticles cannot be attributed

to the catalytic activity of Pt nanoparticles since they are already encapsulated by Co. Therefore, anodic polarization curves are measured in aqueous solutions with 0.87 M N_2H_4 and 0.22 M NaOH using Co and Pt substrates. The Co working electrode is prepared by electrodepositing Co on one side of a commercial Pt-sputtered QCM substrate using the method described in previous reports.[9-10] The Pt working electrode was a commercial Pt-sputtered QCM substrate. As shown in Fig. 3.10, the anodic current primarily due to N_2H_4 oxidation is observed at about –0.88 and –0.79 V vs SHE on the Co and Pt substrates, respectively. At the end of the sweep at –0.20 V, current densities of about 16 and 11 mA cm^{-2} are obtained on the Co and Pt substrates. The high anodic current measured on the Co electrode suggests that Co also has catalytic activity for N_2H_4 oxidation. Therefore, after the Pt nanoparticles are completely covered by Co, oxidation of N_2H_4 is continuously induced on the surface of Co. Co deposition subsequently occurs on the surface of Co, leading to the release of H_2 gas.

Figure 3.11 illustrates the formation of Co nanoparticles by the present method. As discussed in the previous sections, several cathodic (Pt deposition, Co deposition, and H_2 generation) and anodic (N_2H_4 oxidation) partial reactions occur simultaneously during the formation of Co nanoparticles. In principle, oxygen reduction is also plausible. This, however, can be neglected under the presence of N_2H_4. The overall Co deposition reaction is as follows:

$$Co(II) + ½\ N_2H_4 + 2OH^- \rightarrow Co + ½\ N_2 + 2H_2O \qquad (3\text{-}12)$$

Because the oxidation-reduction potential of the Pt(IV)/Pt redox pair is larger than $E_{Co(II)/Co}$ and E_{H_2O/H_2}, Pt(IV) is first reduced by N_2H_4 to form small Pt nanoparticles. Since N_2H_4 is catalytically oxidized on the Pt nanoparticles, Co(II) are easily reduced on the surface of Pt. Co atoms are then preferentially deposited on the Pt nanoparticles. When the Pt nanoparticles are completely encapsulated by Co, N_2H_4 oxidation proceeds on the surface of Co due to its catalytic activity. Therefore, Co nanoparticles continuously grow.

The SEM images of the synthesized Co nanoparticles are shown in Fig. 3.12. The mean particle size decreases with an increase in the amount of H_2PtCl_6. This shows that the nucleating agent apparently works as nuclei of Co nanoparticles.[11-12] The smallest Co nanoparticles of about 24 nm in mean diameter are prepared with the addition of 2.2 mM H_2PtCl_6. The relative standard deviations of the sample size are about 12 - 16 %, which indicates quite narrow size distributions.

Figure 3.13 are the XRD profiles of the products prepared with 0 - 2.2 mM H_2PtCl_6. Without adding the nucleating agent, only peaks of $Co(OH)_2$ are present. On the other hand, hcp and fcc Co nanoparticles are fabricated in the solutions containing H_2PtCl_6. This is consistent with the change of the mixed potentials in Fig. 3.8. The peak widths of 111 and 200 fcc Co at 68.0º and 80.5º become larger with an increase in the concentration of H_2PtCl_6. This indicates that the crystallite sizes of Co nanoparticles are smaller in the samples with the larger H_2PtCl_6 concentration, which is verified by the particle morphology observed by SEM.

The strongest peak at 68.0º is ascribed to 111 fcc Co and its shoulder at a higher scattering angle is due to 002 hcp Co. Thus, the fcc Co phase is dominant in the synthesized Co nanoparticles. This is in good agreement with previous studies.[11,13-14] In Fig. 3.13(e), a very diffused 111 CoO peak is observed at 55.5º. Therefore, the very surface layer of Co

nanoparticles of 24 nm in diameter is oxidized during the preparation of the samples for XRD measurements.

3.4.3 Effect of increasing concentration of NaOH

Figure 3.14 is the SEM images of the Co particles prepared with increasing concentration of NaOH. Large Co particles of about 500 nm in mean diameter are formed with the addition of 0.11 M NaOH. The Co particles are irregularly-shaped and agglomerated, leading to a broad size distribution. In contrast, spherical Co nanoparticles are obtained at 0.22 - 0.87 M NaOH. The Co nanoparticles are uniform in size with mean diameters in the range of 54 - 62 nm.

Figure 3.15 shows the mixed potential measured during the reaction with 0.11 - 0.87 M NaOH. The mixed potential decreases with an increase in the concentration of NaOH. Co(II) reduction occurs faster at larger amounts of NaOH as indicated by the rapid change in the color of the solution after mixing the Co(II) and N_2H_4 solutions. Therefore, NaOH influences the kinetics of the reaction. At 0.11 M NaOH, the mixed potential is larger than $E_{Co(II)/Co}$ for about 80 min. The mixed potential then decreases below $E_{Co(II)/Co}$, and black Co powder is subsequently obtained after 120 min. At 0.22 - 0.87 M NaOH, the solution spontaneously changes to black after the addition of N_2H_4. Simultaneously, the mixed potential then quickly drops below $E_{Co(II)/Co}$.

To clarify the influence of NaOH on reaction rate, polarization curves of Co deposition and N_2H_4 oxidation are separately evaluated in aqueous solutions using Pt-sputtered QCM substrates. For Co deposition, the total current density and the effective mass change are concurrently measured by voltammetry and QCM as shown in Fig. 3.16. The

cathodic current is observed at about –0.64 V vs SHE in the presence of 0.11 M NaOH. Similarly, the onset of cathodic current is evaluated at about –0.73, –0.78 and –0.82 V with 0.22, 0.44 and 0.87 M NaOH, respectively. Thus, it is ascertained that the reduction potential of Co decreases with increasing amount of NaOH. On the other hand, there is no obvious trend observed on the influence of NaOH concentration on the total cathodic current density. Nonetheless, the smallest cathodic current density is measured at 0.87 M NaOH, which indicates that Co deposition is retarded by the precipitation of a high concentration of solid $Co(OH)_2$ in the solution.[15-18] The corresponding mass changes during polarization measurements are plotted in Fig. 3.16(b), which shows increasing amount of deposits at a higher concentration of NaOH. At 0.11 M NaOH, the mass is increased at about –0.72 V vs SHE. This potential is more negative than the value determined by voltammetry in Fig. 3.16(a). Therefore, the cathodic current from –0.64 to –0.72 V could be due to H_2 generation, which explains the non-substantial change in mass. On the other hand, non-electrochemical deposition is promoted with an increase in the amount of NaOH. For example, a sharp increase in mass is observed at 0.87 M NaOH from 0 to –0.82 V, where the current is about zero. As a result, the surface of the electrode is possibly covered, leading to a smaller current density. In theory, the reduction in $E_{Co(II)/Co}$ leads to the decrease in mixed potential. This is consistent with the results in Fig. 3.15.

Figure 3.17 shows the anodic polarization curves measured in aqueous solutions containing 0.87 M N_2H_4 and 0.11 - 0.87 M NaOH. The oxidation potential of N_2H_4 is reduced from –0.74 to –0.88 V with the addition of 0.11 to 0.87 M NaOH. This indicates an increase in the reducing force of N_2H_4 with a larger amount of NaOH. On the other hand, the anodic current density is increased with increasing concentration of NaOH. The anodic

current density at 0.44 M NaOH is about twice as large as the values at 0.11 and 0.22 M, while the anodic current density at 0.87 M is almost twice the value at 0.44 M. Consequently, the mixed potential in Fig. 3.15 progressively decreases. Therefore, the addition of a larger concentration of NaOH results in lower reduction and oxidation potentials of Co and N_2H_4, respectively. In addition, the anodic current density for N_2H_4 oxidation is increased. Consequently, the mixed potential decreases, which leads to faster reaction rates.

3.4.4 Effect of addition of propylene glycol (PG)

Figure 3.18 shows the SEM images of Co particles formed after 1 h in solutions with increasing volume ratio of PG:H_2O. Spherical Co particles with narrow size distributions are obtained in all samples. The mean diameter, however, is reduced from 132 to 55 nm with a decrease in the volume of PG. The 132 nm Co particles formed in pure PG solution are composed of several smaller nanoparticles as seen at high magnification by SEM.

To understand the effect of PG on the formation of Co particles, samples are prepared at different reaction times in a pure PG solution containing 87 mM Co(II) acetate, 0.22 M NaOH, 0.22 mM H_2PtCl_6, 1.1 mM PEG, and 0.87 M N_2H_4. Figure 3.19 shows the XRD profiles of the Co products in propylene glycol. At 5 min, a sharp 111 CoO peak at 55.5º is observed, and the small 200 CoO peak at 65.0º overlaps with the 100 hcp, 111 fcc, and 002 hcp Co. Thus, a large broad peak is observed in Fig. 3.19(a). The large particles in Fig. 3.20(a) are therefore agglomerates of Co and CoO, which is from the reaction between Co(II) and OH^- ions. After 10 - 60 min, the XRD patterns in Fig. 3.19(b-e) show an increase in the

intensity of Co peaks. Simultaneously, the CoO peaks become weaker. More intermediate phase is possibly dissolved to supply Co(II) at longer reaction time.

Based on the above results, the endpoint of the formation of Co nanoparticles in pure PG solution is evaluated to be about 60 min since no significant change in morphology is observed after this time, and only a small amount of CoO is present in the particles. This CoO is possibly from oxidation during washing. In contrast, Co nanoparticles are prepared after 20 min in an aqueous solution as shown in Fig. 3.4 and 3.5. Therefore, Co(II) reduction is slower in a PG solution than in an aqueous solution. This is also clearly seen in the SEM images of the Co products in Fig. 3.20, which show variations in the morphology with time. At the early stage of reaction (5 - 10 min), large agglomerated particles consisting of CoO as the intermediate product and Co nanoparticles as the final product are obtained. The samples have a wide size distribution with diameters in the range of 100 - 400 nm. After 20 min, the mean diameter is about 152 nm, and the particles are more spherical. When the reaction reaches 40 min, the particle size is further decreased to about 143 nm. At this point, CoO is dissolved and Co nanoparticles are obtained.

To investigate the influence of PG on the oxidation of N_2H_4, an anodic polarization curve is measured on a Pt electrode in a PG solution with 0.22 M NaOH and 0.87 M N_2H_4. The anodic curve is plotted in Fig. 3.21 together with the anodic polarization curve in an aqueous solution with the same concentration of NaOH and N_2H_4. The oxidation potential of N_2H_4 in PG solution is observed at about –0.58 V vs Ag/AgCl, which is more positive than the value in an aqueous solution (about –1.0 V vs Ag/AgCl). The slope of the anodic current density is smaller in a PG solution, which results in a smaller current density at the end of the

sweep. This suggests that the oxidation of N_2H_4 is relatively slow in PG even in the presence of Pt nanoparticles as catalysts. Consequently, the reduction rate of Co(II) decreases.

The mixed potential measured during electroless deposition with increasing volume ratio of PG:H_2O shows two distinct behaviors as depicted in Fig. 3.22. At start of the reaction, the mixed potential increases with larger amount of PG. This is attributed to the decrease in the anodic current density, which slows down the rate of Co deposition. On the other hand, the mixed potential is lower at a higher amount of PG after 20 - 30 min reaction. Since Co nanoparticles are easily obtained in aqueous solutions, the rapid increase in the mixed potential after 20 min is primarily due to the consumption of N_2H_4 in the solution. In contrast, a higher concentraton of N_2H_4 is still available in a PG solution owing to the slow oxidation rate. Therefore, more negative mixed potential is observed.

3.4.5 Effect of increasing concentration of N_2H_4

Figure 3.23 shows the dependence of the mixed potential with time in aqueous solutions with 0.61 - 1.3 M N_2H_4. In general, the mixed potential decreases with an increase in the concentration of N_2H_4. Specifically, an instantaneous drop of the mixed potential below $E_{Co(II)/Co}$ is observed after the addition of 1.3 M N_2H_4, suggesting a very fast reaction rate. SEM images of the synthesized Co nanoparticles in Fig. 3.24 show that the mean particle diameter is slightly reduced from 75 to 50 nm with a larger concentration of N_2H_4. More Co atoms are precipitated at a time with a higher N_2H_4 concentration, which leads to a faster nucleation of Co nanoparticles. Thus, the growth step is suppressed, and smaller nanoparticles are obtained.

3.5 Summary

Metallic Co particles of 24 - 500 nm diameters are prepared by electroless deposition in an aqueous solution at room temperature using H_2PtCl_6 and N_2H_4 as nucleating and reducing agents, respectively. Electrochemical measurements, such as in-situ monitoring of mixed potentials in conjunction with quartz crystal microbalance and linear sweep voltammetry, are carried out to study the formation of Co nanoparticles. Co(II) reduction generally occurs when the mixed potential drops below $E_{Co(II)/Co}$, which coincides with the increase in deposited mass measured by QCM. Both the overall reaction rate and the apparent particle diameter depend on the concentrations of the H_2PtCl_6 and NaOH, and volume of propylene glycol in the solution. The current density for N_2H_4 oxidation is increased with increasing concentration of H_2PtCl_6, possibly due to the catalytic activity of Pt nanoparticles. In addition, both a higher amount of NaOH and a lower volume of propylene glycol result in the decrease in the oxidation potential of N_2H_4 and the increase in the anodic current density. Consequently, the mixed potential is shifted negatively. Co deposition is therefore accelerated, leading to the reduction in the particle size.

Table 3.1 List of standard Gibbs free energy of formation[4] (kJ mol^{-1}) at 298 K used for thermodynamic calculation.

Chemical species	Standard Gibbs free energy of formation (kJ mol^{-1})
H^+ (aq)	0.0
H_2 (g)	0.0
H_2O (l)	–237.2
Co^{2+} (aq)	–53.6
Co (s)	0.0
$Co(OH)_2$ (s)	–456.1
N_2H_4 (aq)	127.9
N_2 (g)	0.0
NH_3 (g)	–16.6

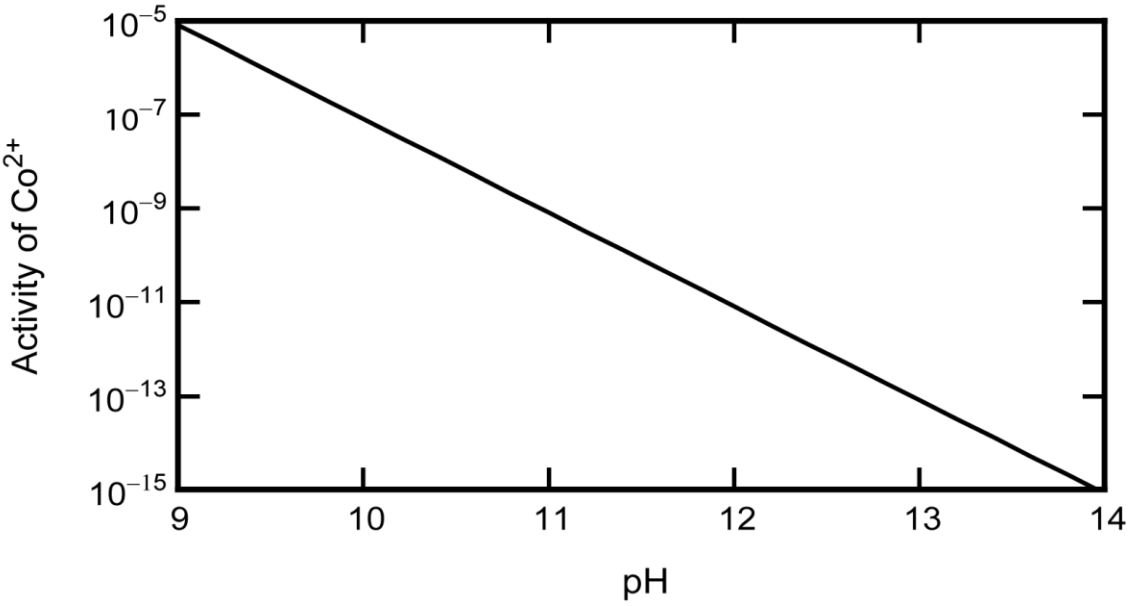

Figure 3.1 pH-dependence of the activity of Co^{2+} aquo ions calculated in Equation (3-3) from the thermodynamic data in Table 3.1.

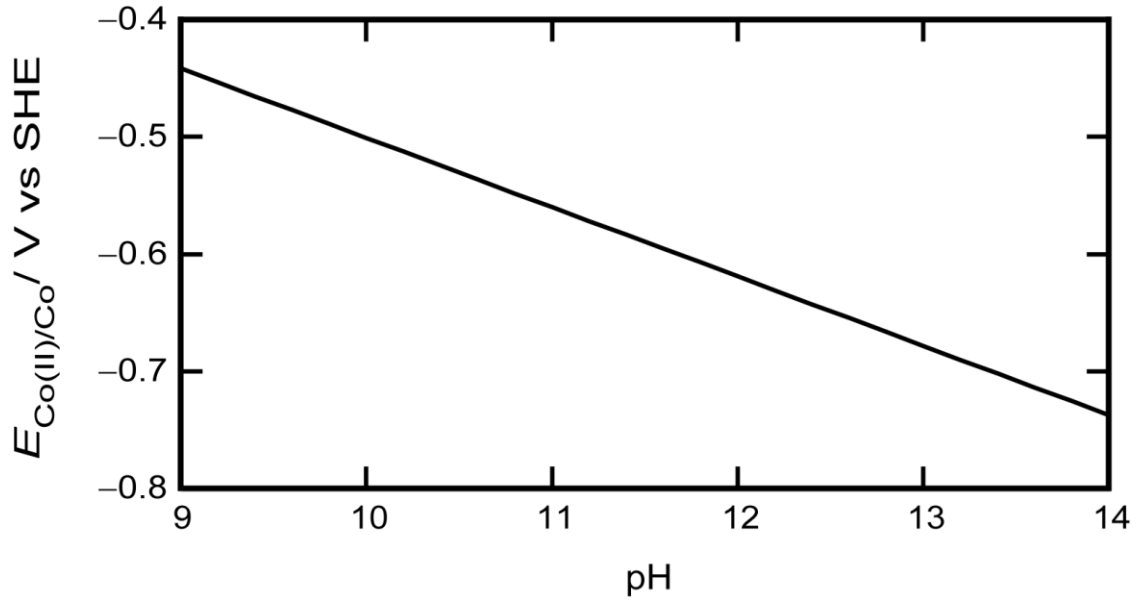

Figure 3.2 pH-dependence of the oxidation-reduction potential of the Co(II)/Co redox pair ($E_{Co(II)/Co}$) calculated in Equation (3-8) from the thermodynamic data in Table 3.1.

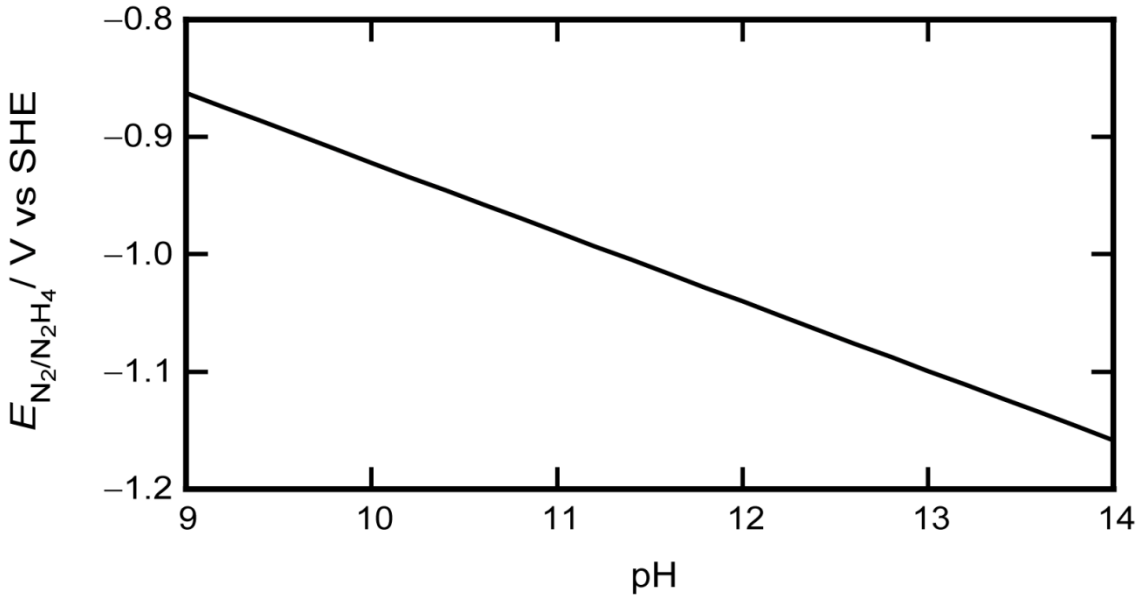

Figure 3.3 Change in the oxidation-reduction potential of the N_2/N_2H_4 [E_{N_2/N_2H_4}] redox pair with pH calculated in Equations (3-11) from the thermodynamic data in Table 3.1.

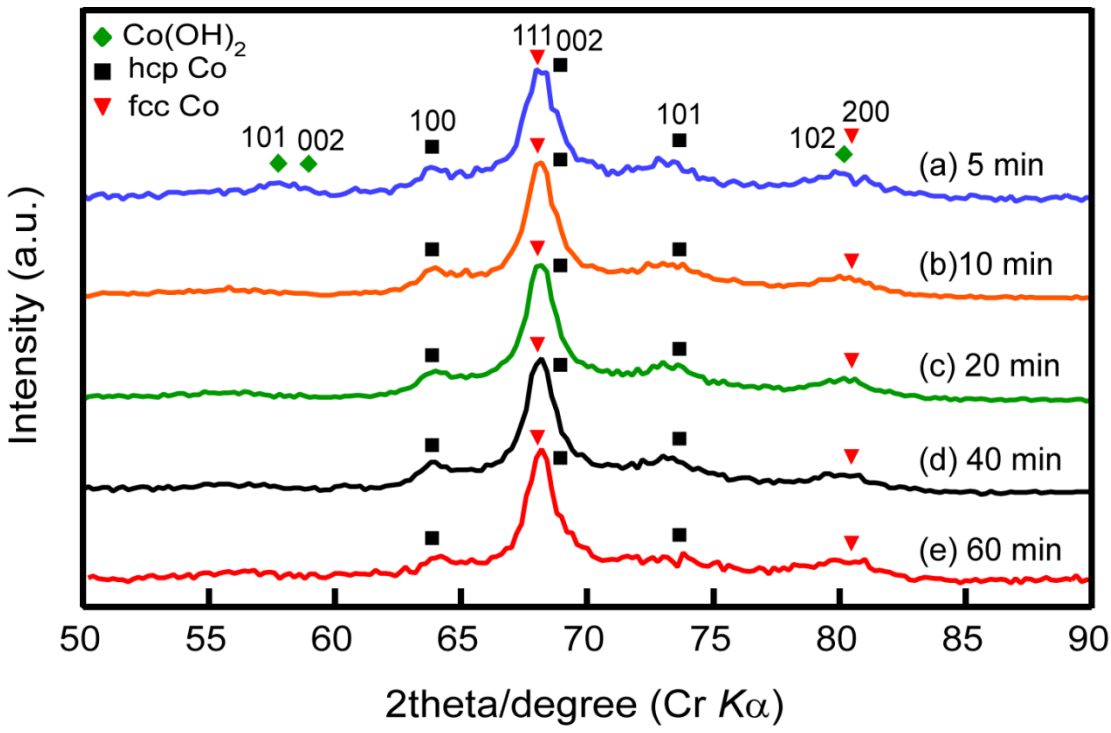

Figure 3.4 XRD profiles of Co products prepared at reaction times of (a) 5, (b) 10, (c) 20, (d) 40, and (e) 60 min by electroless deposition in an aqueous solution at room temperature. The aqueous solution contains 87 mM Co(II) acetate, 1.1 mM PEG, 0.22 M NaOH, 0.22 mM H_2PtCl_6, and 0.87 M N_2H_4.

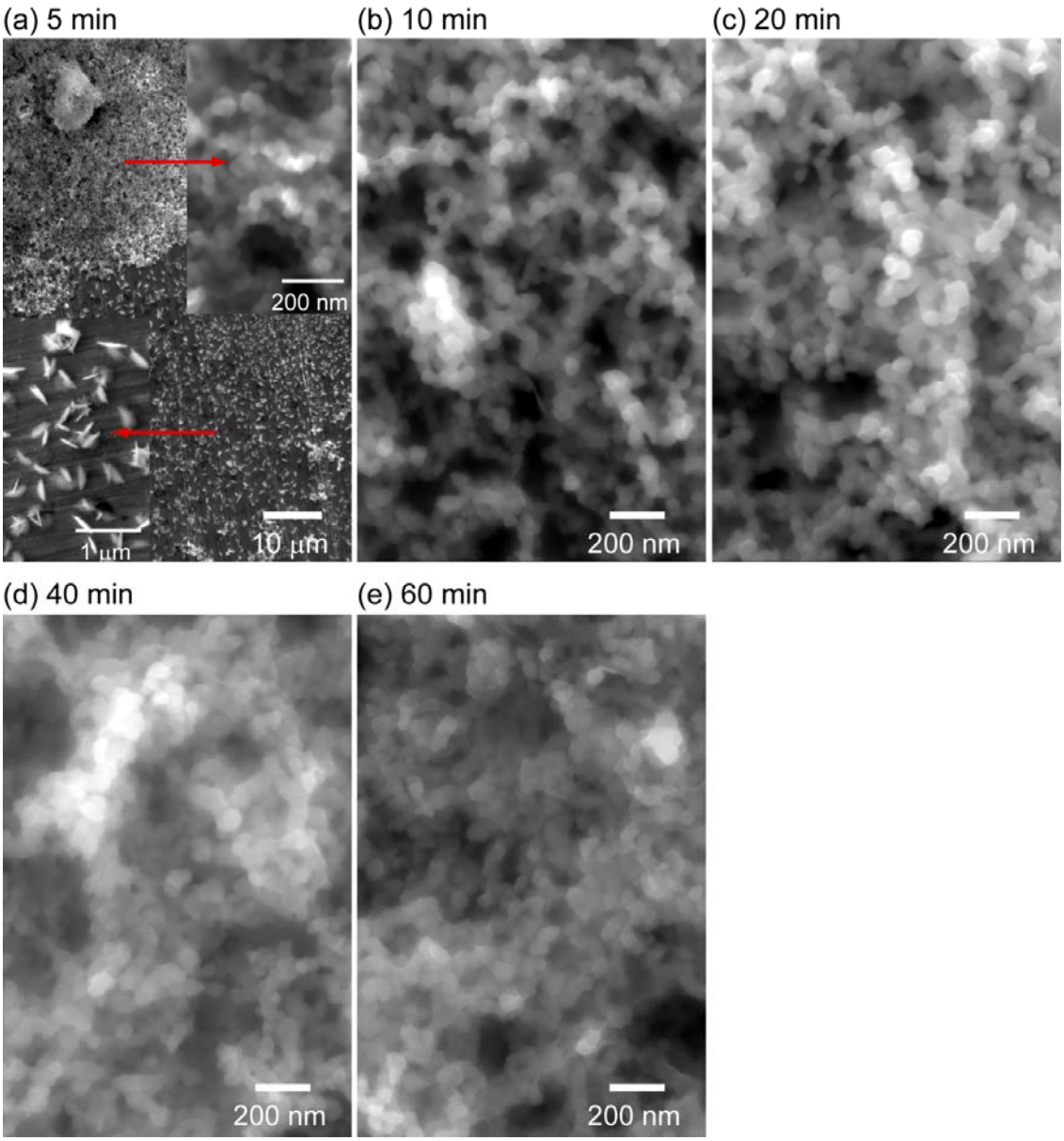

Figure 3.5 SEM images of Co products prepared at reaction times of (a) 5, (b) 10, (c) 20, (d) 40, and (e) 60 min in an aqueous solution at room temperature. Inset shows high-magnification SEM images of Co products obtained after 5 min reaction. The aqueous solution contains 87 mM Co(II) acetate, 1.1 mM PEG, 0.22 M NaOH, 0.22 mM H_2PtCl_6, and 0.87 M N_2H_4.

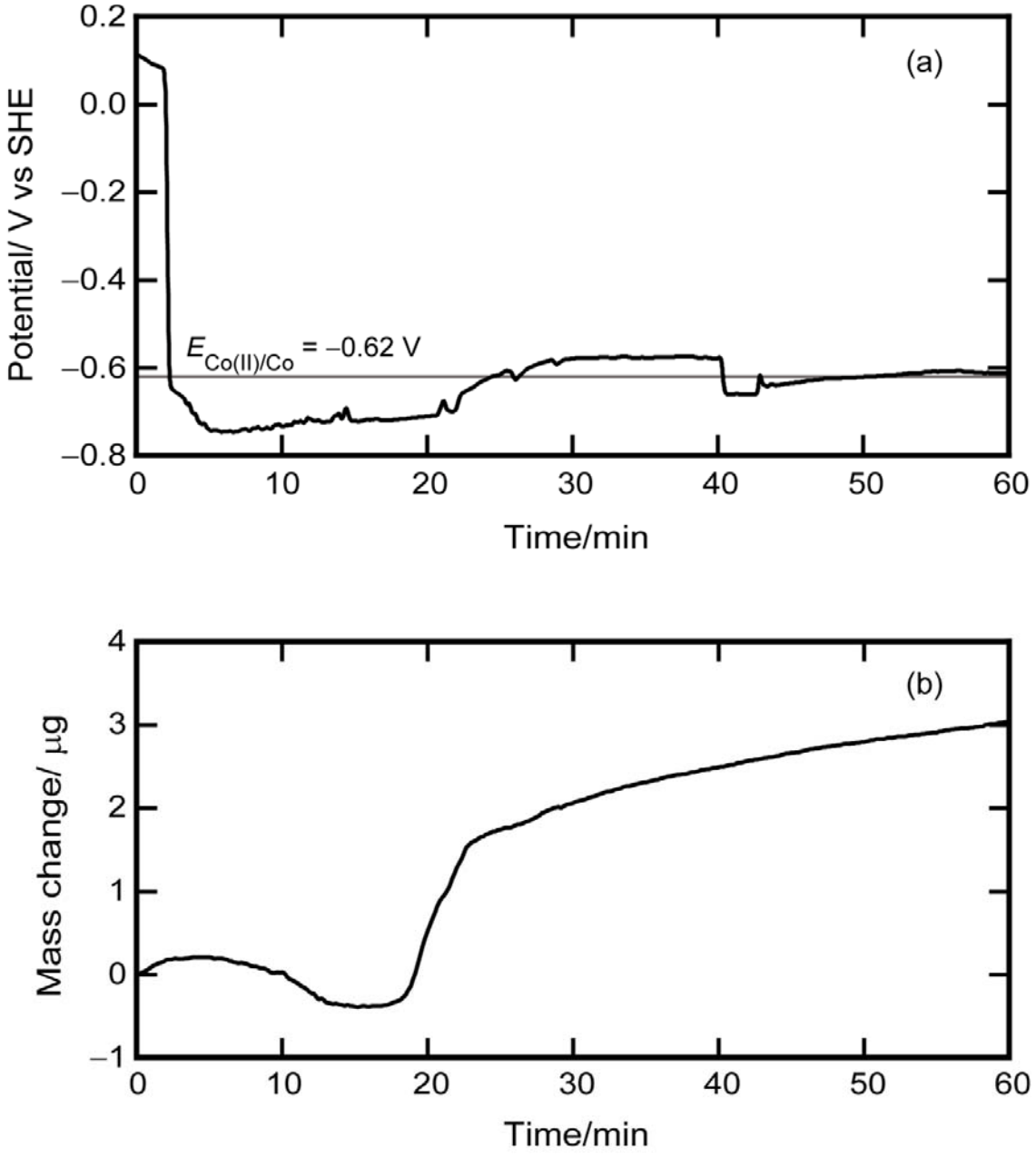

Figure 3.6 Changes in (a) mixed potential and (b) deposited mass (Δm) measured on a Pt-sputtered QCM substrate during electroless deposition in an aqueous solution at room temperature. The aqueous solution contains 87 mM Co(II) acetate, 1.1 mM PEG, 0.22 M NaOH, 0.22 mM H_2PtCl_6, 0.87 M N_2H_4, and 0.10 M Na_2SO_4 as supporting electrolyte.

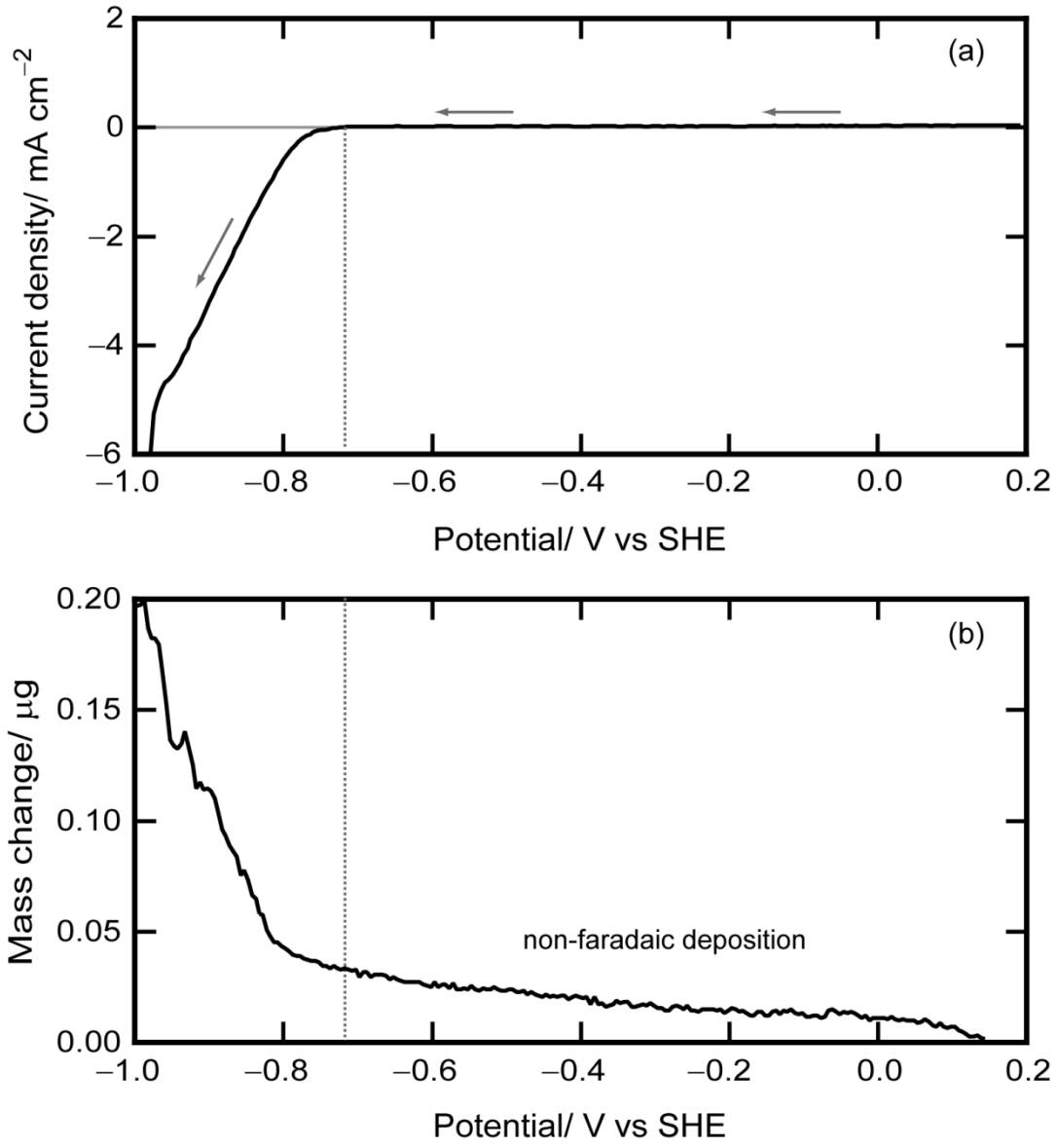

Figure 3.7 (a) Cathodic polarization curve and the (b) effective mass change measured on a Pt-sputtered QCM substrate in an aqueous solution containing 87 mM Co(II) acetate and 0.22 M NaOH. The onset of cathodic current is observed at about −0.73 V vs SHE as indicated by the dashed line. Arrows point to the direction of the sweep. The aqueous solution contains 0.10 M Na_2SO_4 as supporting electrolyte.

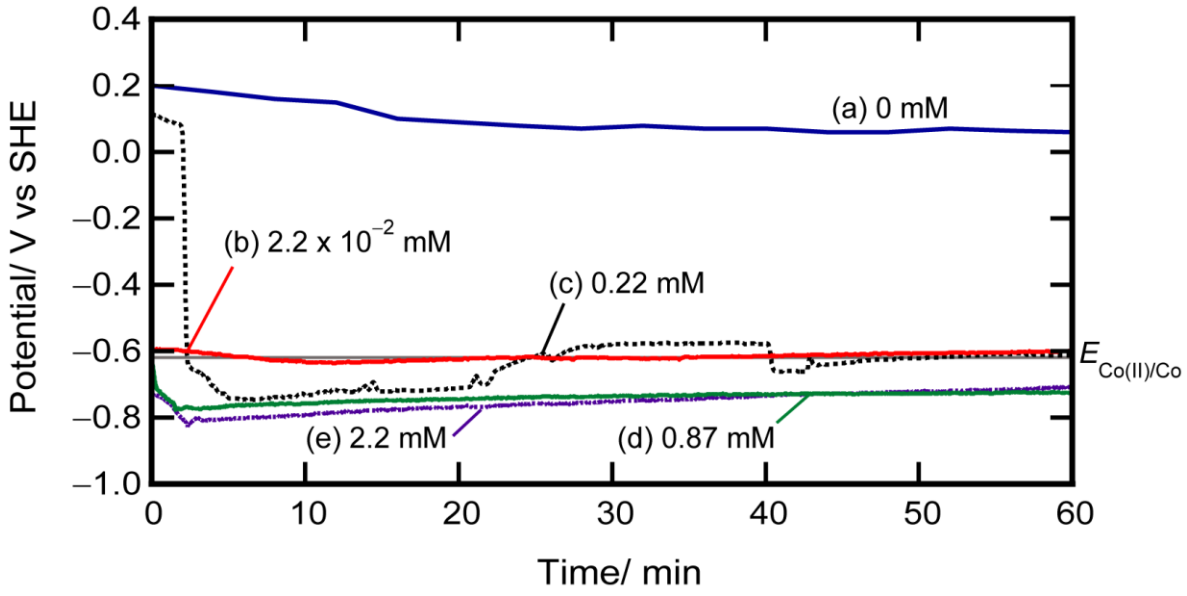

Figure 3.8 Change in mixed potential with time during electroless deposition in an aqueous solution containing (a) 0, (b) 2.2 x 10^{-2}, (c) 0.22, (d) 0.87, and (e) 2.2 mM H_2PtCl_6 nucleating agent. The aqueous solution contains 87 mM Co(II) acetate, 1.1 mM PEG, 0.22 M NaOH, 0.87 M N_2H_4, and 0.10 M Na_2SO_4 as supporting electrolyte.

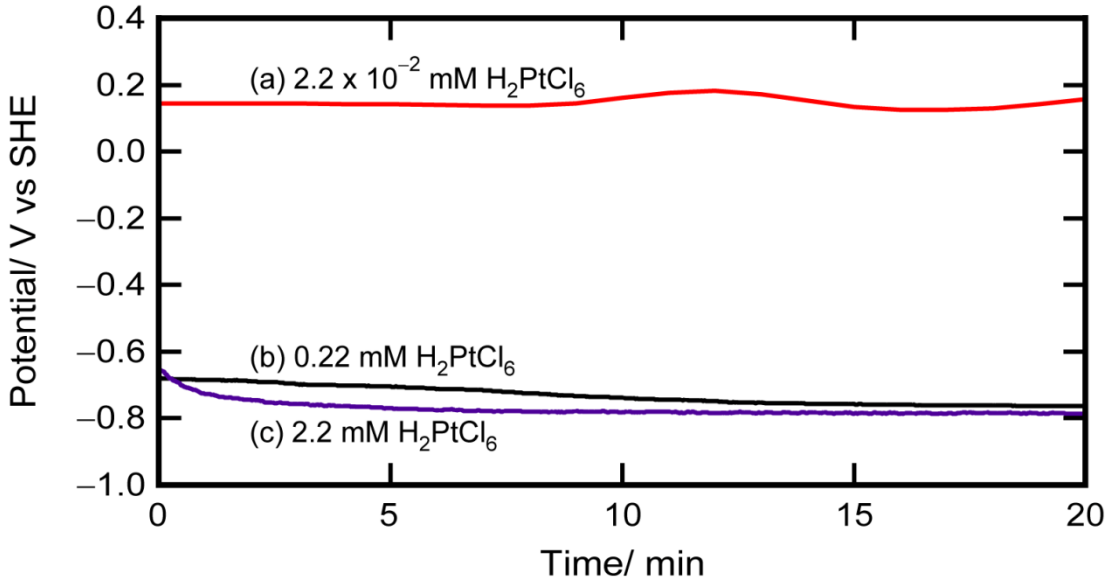

Figure 3.9 Change in mixed potential with time measured on a Pt-sputtered QCM electrode during electroless deposition of (a) 2.2 x 10^{-2}, (b) 0.22, and (c) 2.2 mM H_2PtCl_6 in an aqueous solution at room temperature. The aqueous solution contains 1.1 mM PEG, 0.22 M NaOH, 0.87 M N_2H_4, and 0.10 M Na_2SO_4 as supporting electrolyte.

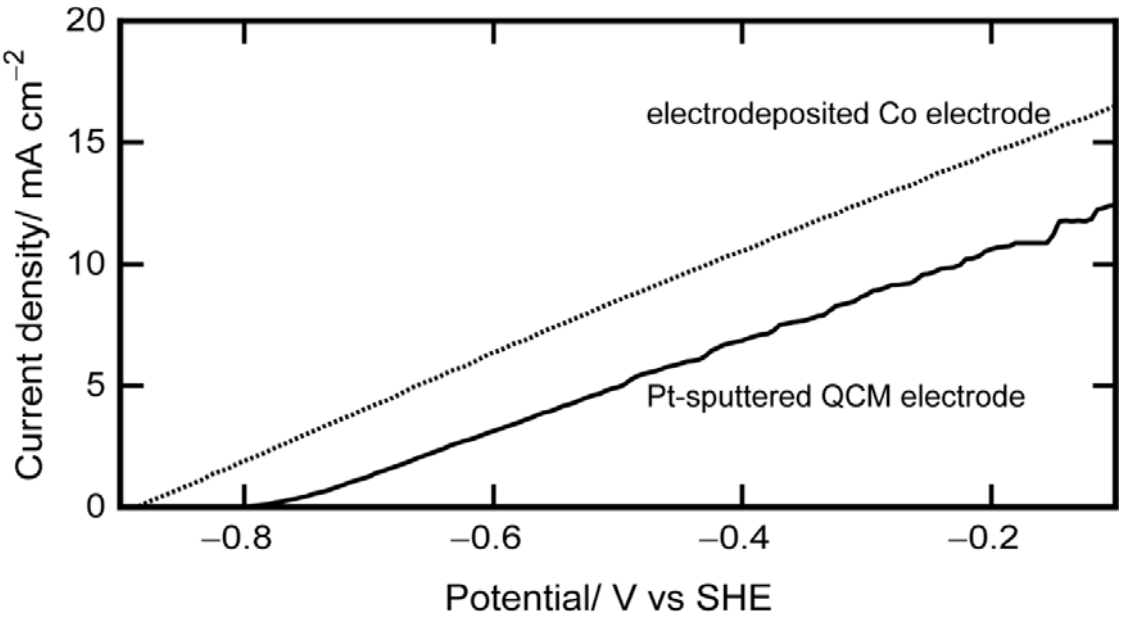

Figure 3.10 Anodic polarization curves measured in an aqueous solution containing 0.87 M N_2H_4 and 0.22 M NaOH using electrodeposited Co and commercial Pt-sputtered QCM electrodes. The aqueous solution contains 0.10 M Na_2SO_4 as supporting electrolyte.

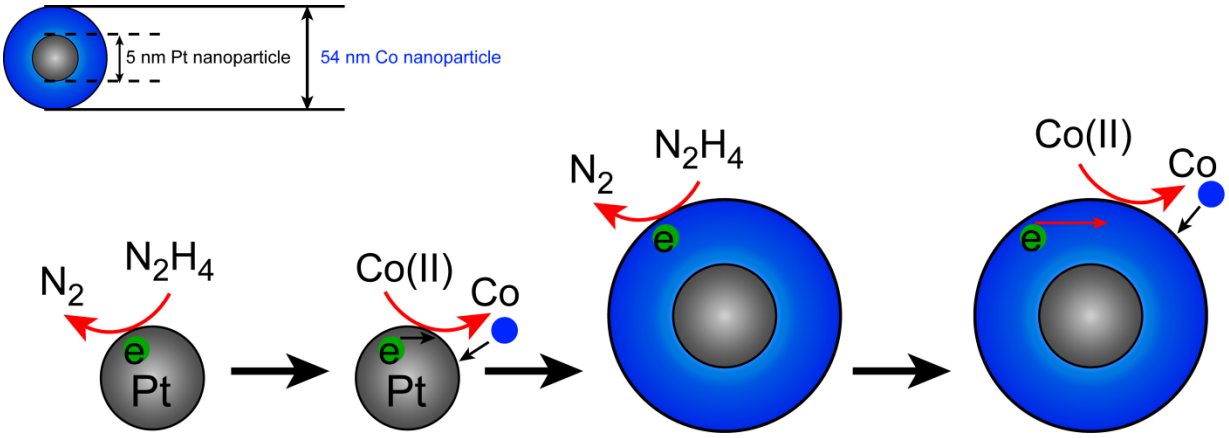

Figure 3.11 Schematic of the formation of Co nanoparticles by electroless deposition in an aqueous solution using H_2PtCl_6 and N_2H_4 as nucleating and reducing agents.

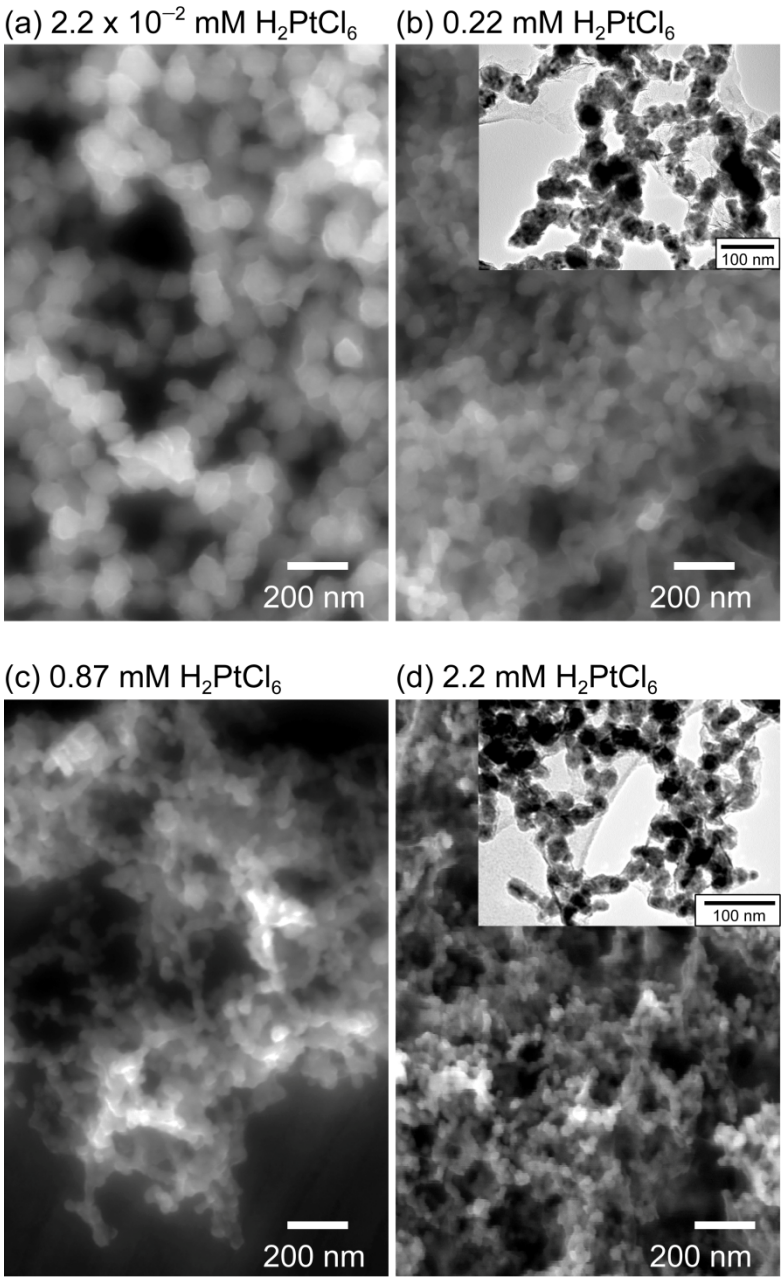

Figure 3.12 SEM and TEM images of Co nanoparticles prepared using (a) 2.2 x 10^{-2}, (b) 0.22, (c) 0.87, and (d) 2.2 mM H_2PtCl_6 nucleating agent. The mean particle size is (a) 112, (b) 54, (c) 40, and (d) 24 nm. The aqueous solution contains 87 mM Co(II) acetate, 1.1 mM PEG, 0.22 M NaOH, and 0.87 M N_2H_4.

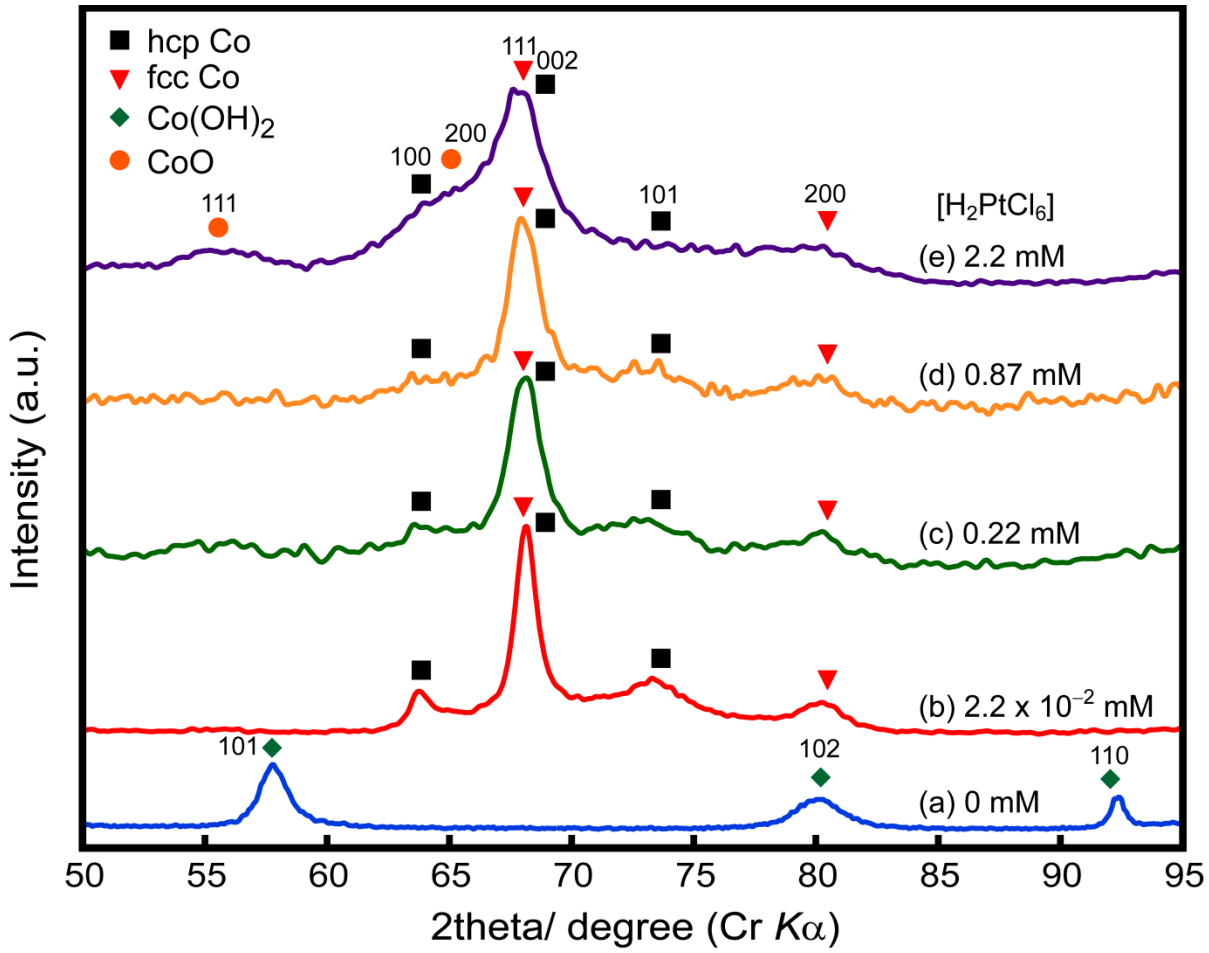

Figure 3.13 XRD profiles of Co products prepared using (a) 0, (b) 2.2 x 10^{-2}, (c) 0.22, (d) 0.87, and (e) 2.2 mM H_2PtCl_6. The aqueous solution contains 87 mM Co(II) acetate, 1.1 mM PEG, 0.22 M NaOH, and 0.87 M N_2H_4.

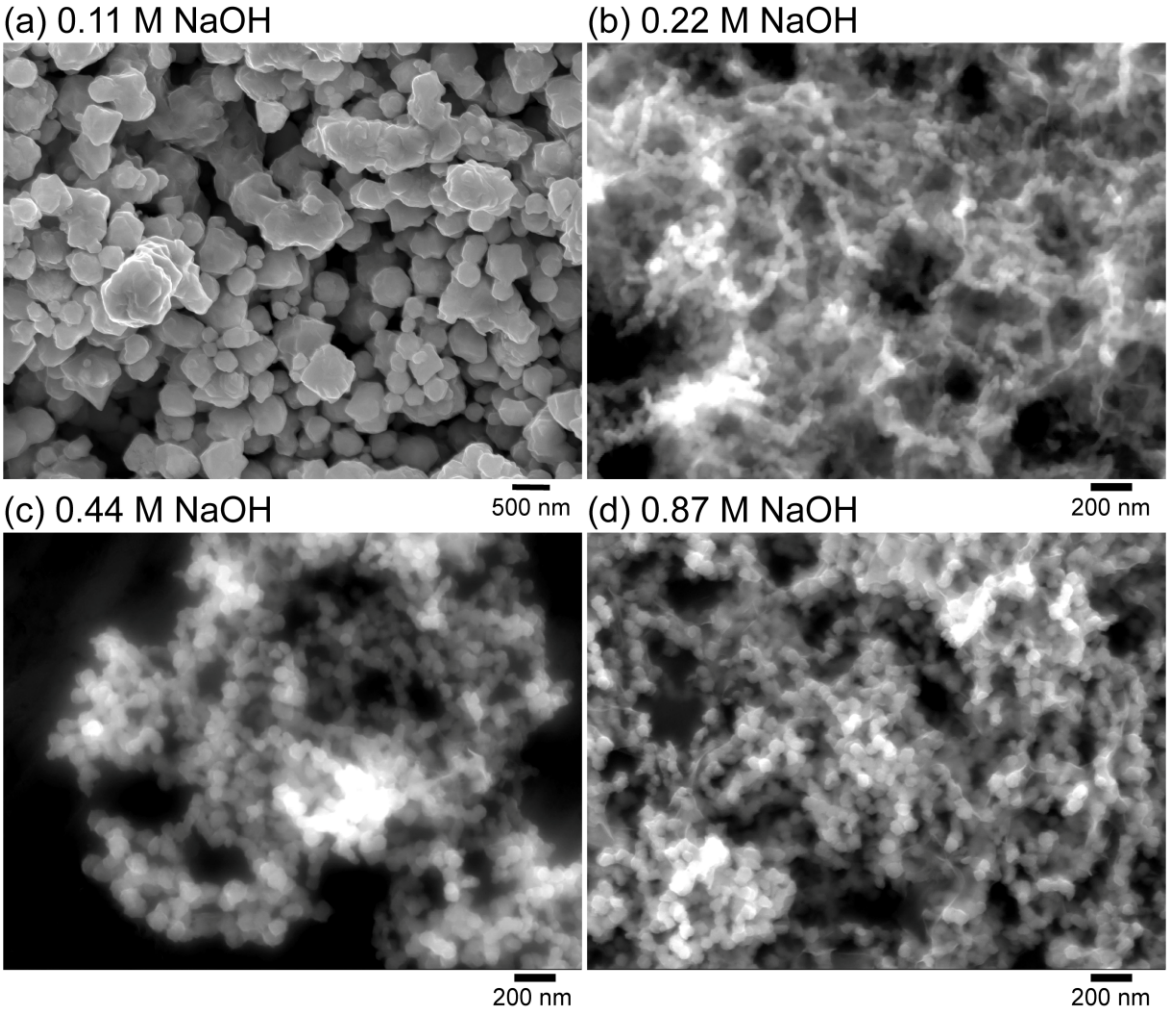

Figure 3.14 SEM images of Co particles synthesized using (a) 0.11, (b) 0.22, (c) 0.44, and (d) 0.87 M NaOH. The pH of the solution increases from about 10 to 14 with an increase in the concentration of NaOH. The aqueous solution contains 87 mM Co(II) acetate, 1.1 mM PEG, 0.22 mM H_2PtCl_6, and 0.87 M N_2H_4.

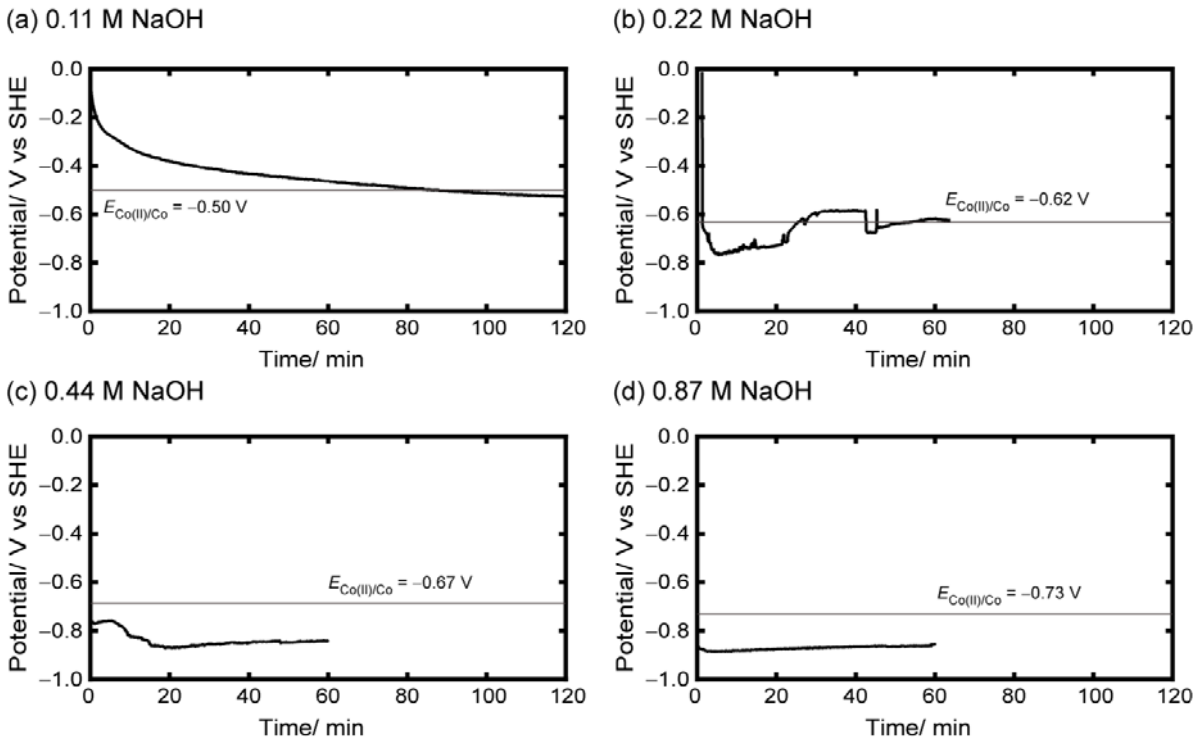

Figure 3.15 Change in mixed potential with time measured during electroless deposition of Co particles using (a) 0.11, (b) 0.22, (c) 0.44, and (d) 0.87 M NaOH. The pH of the solution increases from about 10 to 14 with an increase in the concentration of NaOH. The aqueous solutions contain 87 mM Co(II) acetate, 1.1 mM PEG, 0.22 mM H_2PtCl_6, 0.87 M N_2H_4, and 0.10 M Na_2SO_4 as supporting electrolyte.

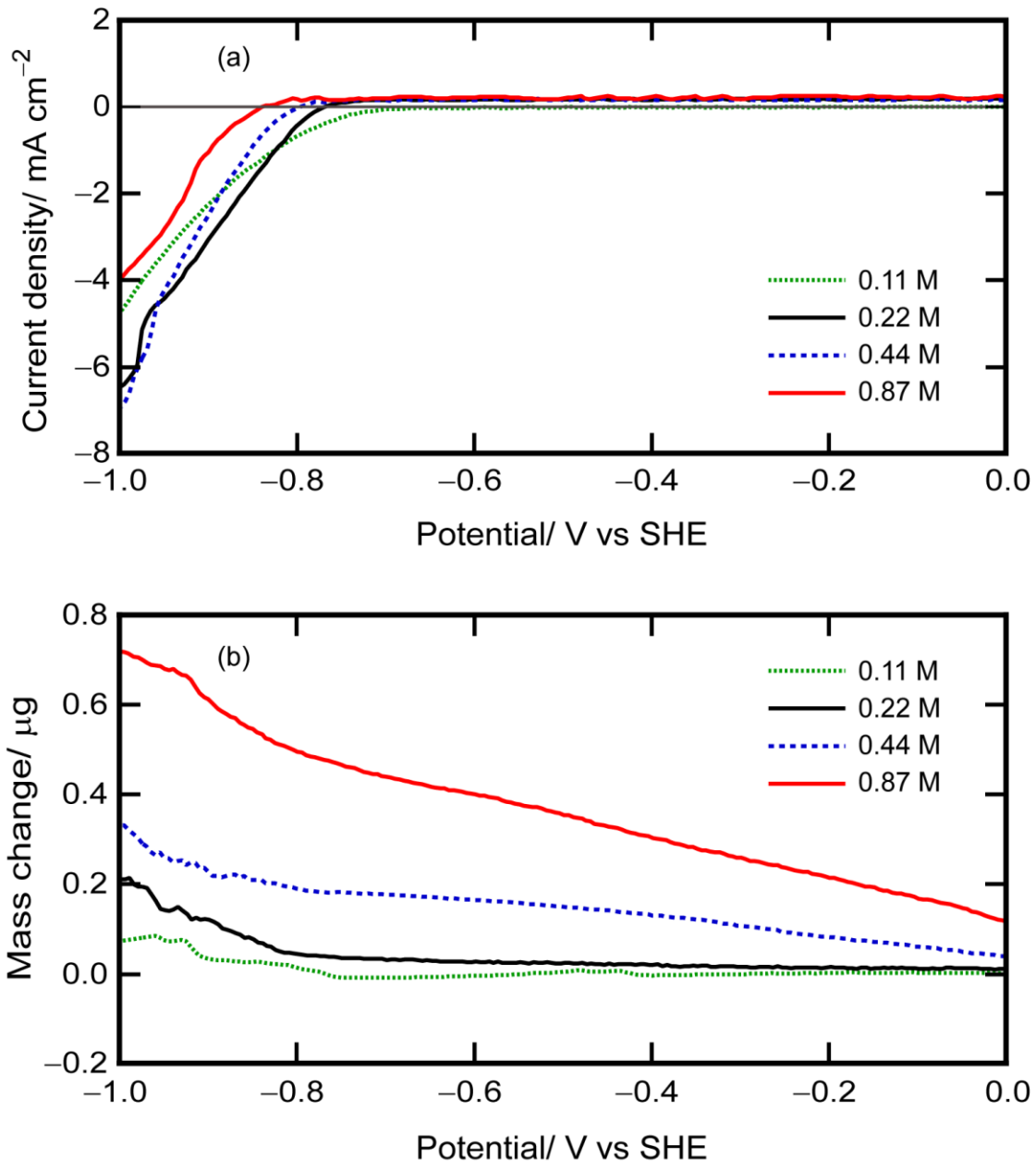

Figure 3.16 (a) Cathodic polarization curves with the (b) effective mass change measured at 1 mV s^{-1} on Pt-sputtered QCM substrates in 115 cm^3 aqueous solutions containing 87 mM Co(II) acetate and 0.11 - 0.87 M NaOH. The aqueous solutions contain 0.10 M Na_2SO_4 as supporting electrolyte.

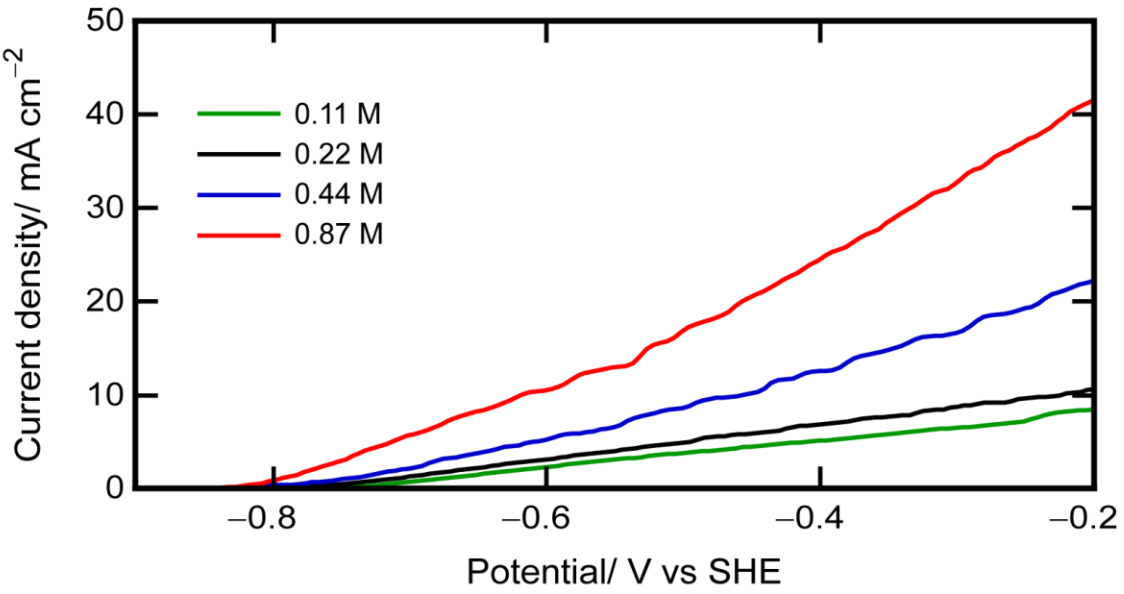

Figure 3.17 Anodic polarization curves measured on a Pt-sputtered QCM substrate at 1 mV s^{-1} in 115 cm^3 aqueous solutions containing 0.87 M N_2H_4 and 0.11 - 0.87 M NaOH. The aqueous solutions contain 0.10 M Na_2SO_4 as supporting electrolyte.

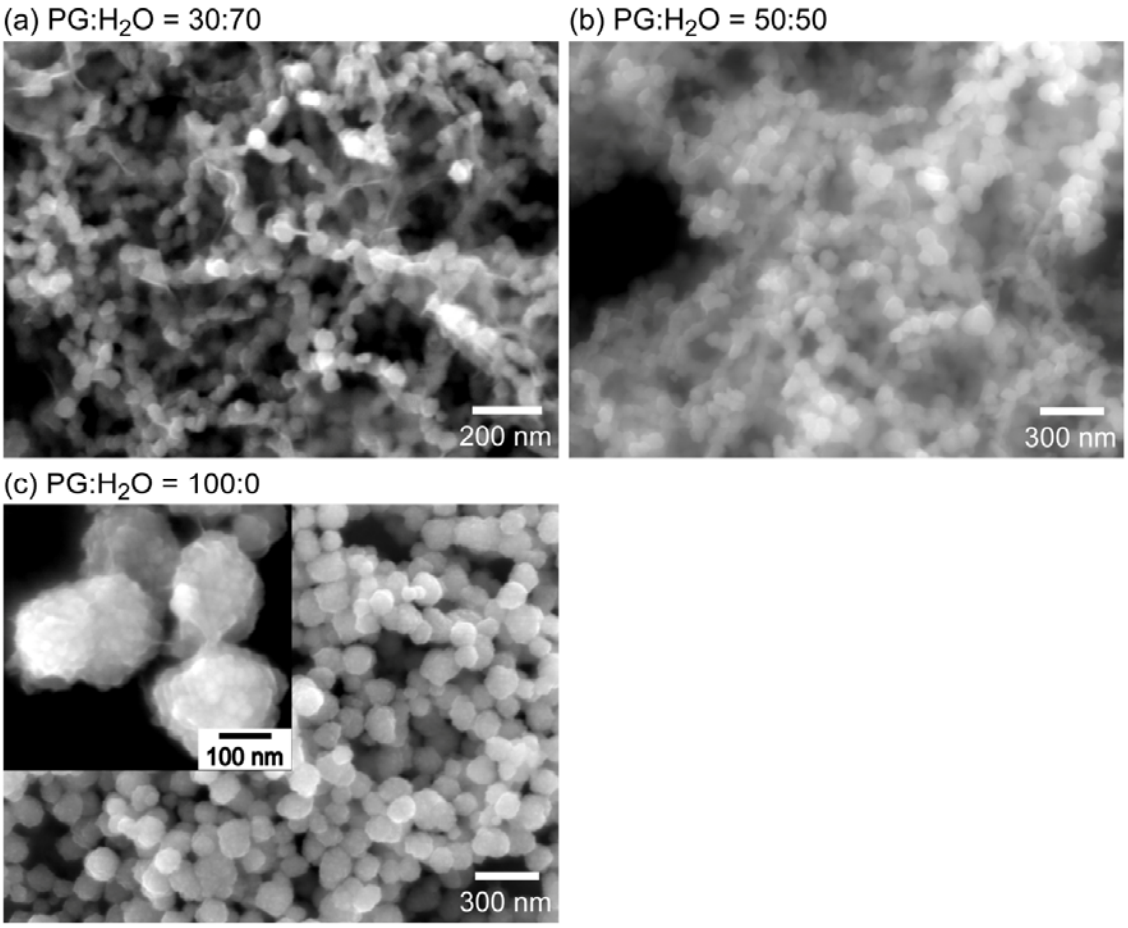

Figure 3.18 SEM images of Co particles prepared in solutions with a PG:H_2O volume ratio of (a) 30:70, (b) 50:50, and (c) 100:0 at room temperature. The mean particle size of the Co particles is (a) 55, (b) 79, and (c) 132 nm. Inset shows a SEM image of the 132 nm Co particles at high magnification. The solutions contain 87 mM Co(II) acetate, 1.1 mM PEG, 0.22 M NaOH, 0.22 mM H_2PtCl_6, and 0.87 M N_2H_4.

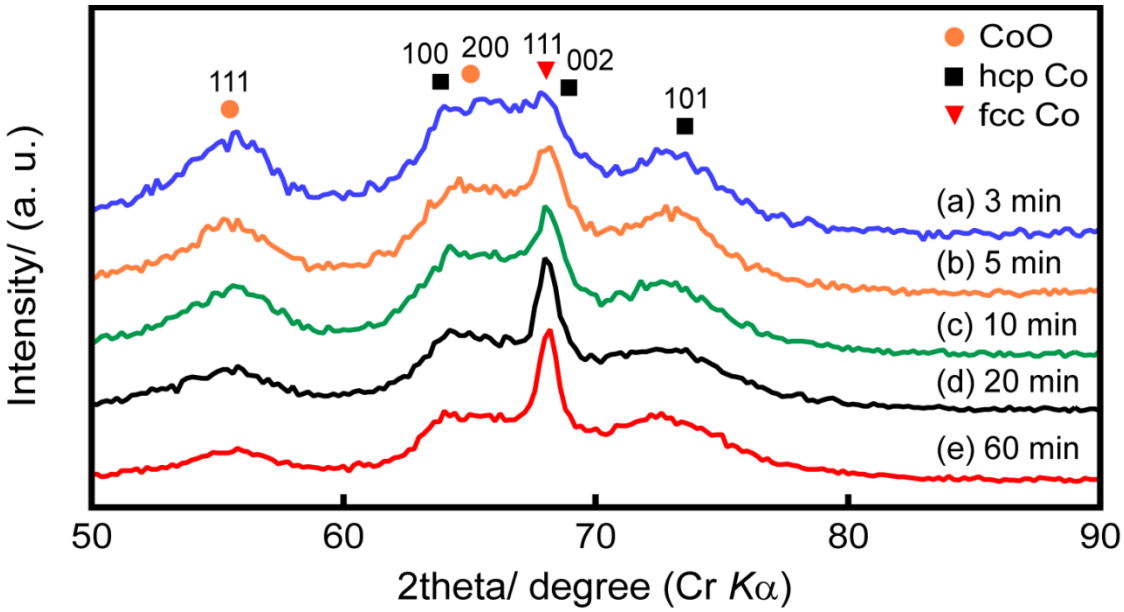

Figure 3.19 XRD patterns of Co products prepared in pure propylene glycol at a reaction time of (a) 5, (b) 10, (c) 20, (d) 40, and (e) 60 min. The solution contains 87 mM Co(II) acetate, 1.1 mM PEG, 0.22 M NaOH, 0.22 mM H_2PtCl_6, and 0.87 M N_2H_4.

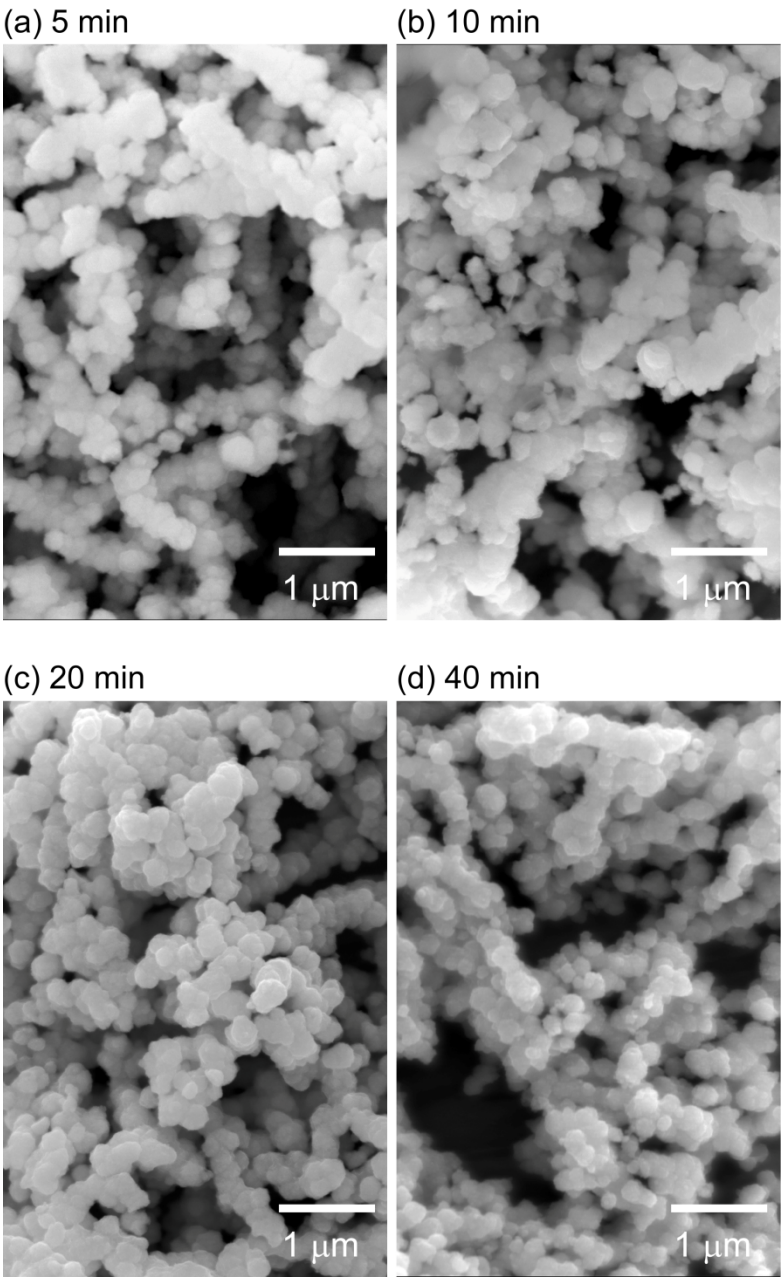

Figure 3.20 SEM images of Co products prepared in a propylene glycol solution after (a) 5, (b) 10, (c) 20, and (d) 40 min. The solution contains 87 mM Co(II) acetate, 1.1 mM PEG, 0.22 M NaOH, 0.22 mM H_2PtCl_6, and 0.87 M N_2H_4.

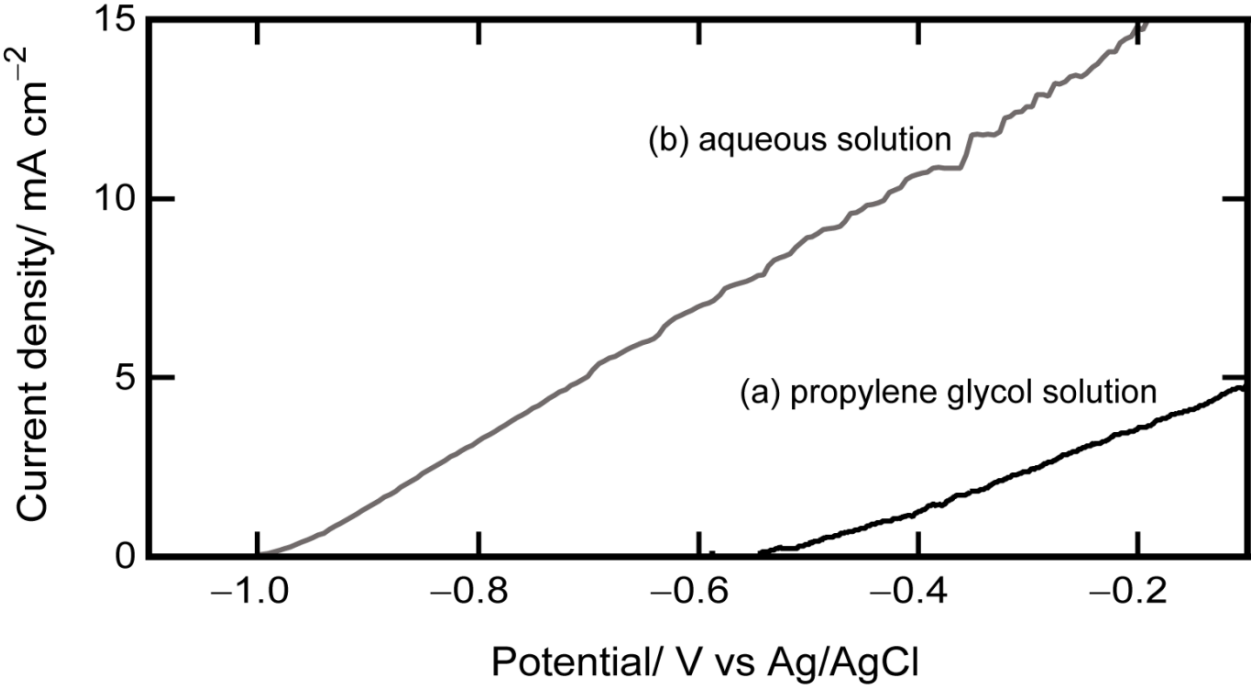

Figure 3.21 Anodic polarization curves measured at 1 mV s^{-1} on Pt- sputtered QCM substrates in (a) propylene glycol and (b) aqueous solutions containing 0.87 M N_2H_4 and 0.22 M NaOH. 0.10 M Na_2SO_4 and 0.10 M $LiClO_4$ are used as supporting electrolytes in aqueous and PG solutions, respectively.

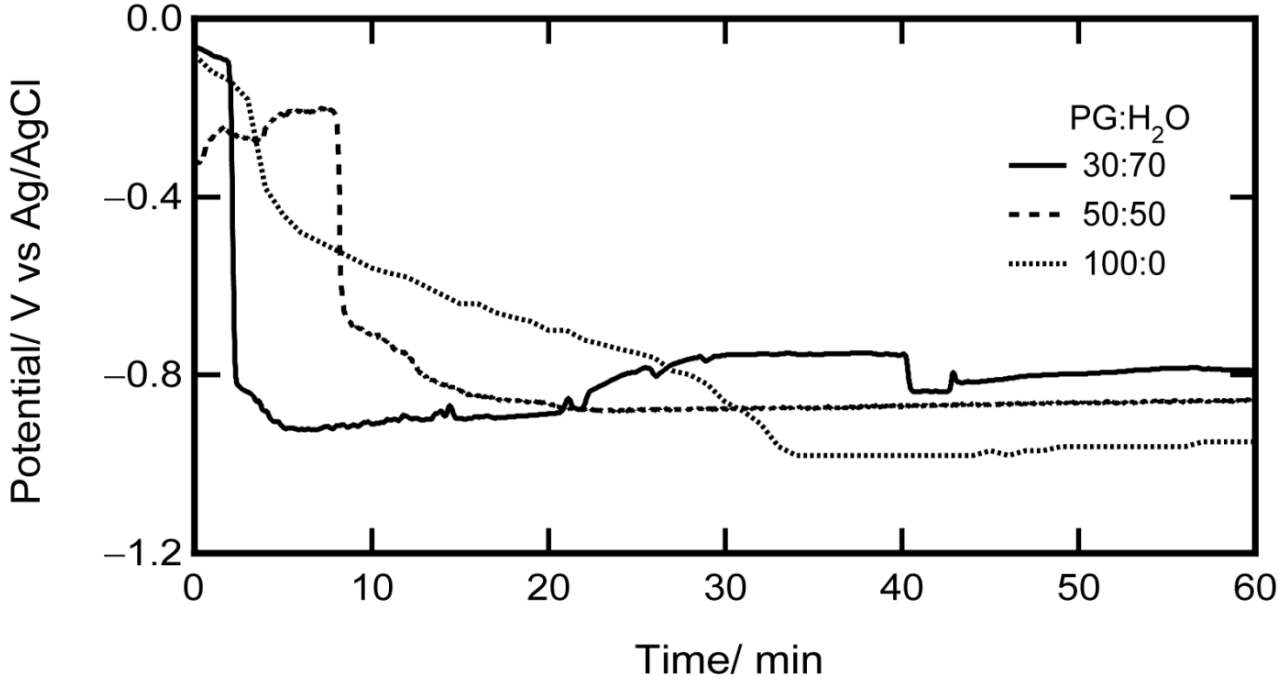

Figure 3.22 Change in mixed potential with time during electroless deposition in solutions with PG:H_2O volume ratios of 30:70, 50:50, and 100:0. The mean particle sizes of the Co particles are 55, 79, and 132 nm, respectively. The solutions contain 87 mM Co(II) acetate, 1.1 mM PEG, 0.22 M NaOH, 0.22 mM H_2PtCl_6, and 0.87 M N_2H_4. 0.10 M Na_2SO_4 or 0.10 M $LiClO_4$ is used as supporting electrolyte.

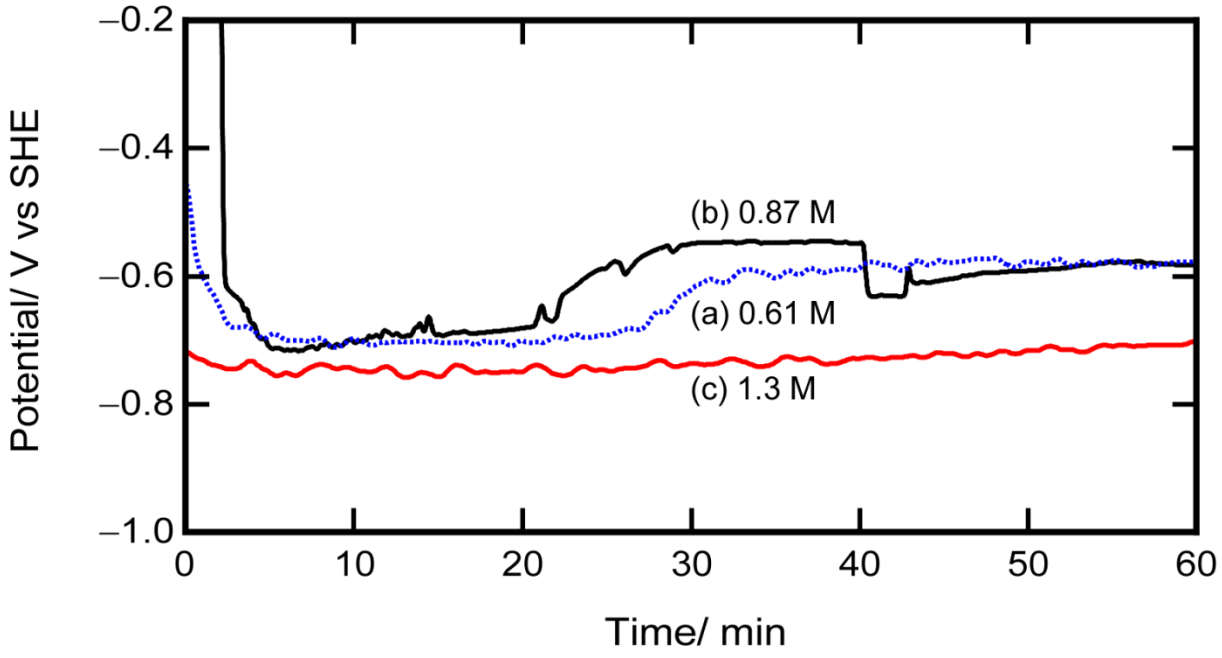

Figure 3.23 Mixed potential measured during electroless deposition in aqueous solutions with (a) 0.61, (b) 0.87, and (c) 1.3 M N_2H_4. The solutions contain 87 mM Co(II) acetate, 1.1 mM PEG, 0.22 M NaOH, 0.22 mM H_2PtCl_6, and 0.10 M Na_2SO_4 as supporting electrolyte.

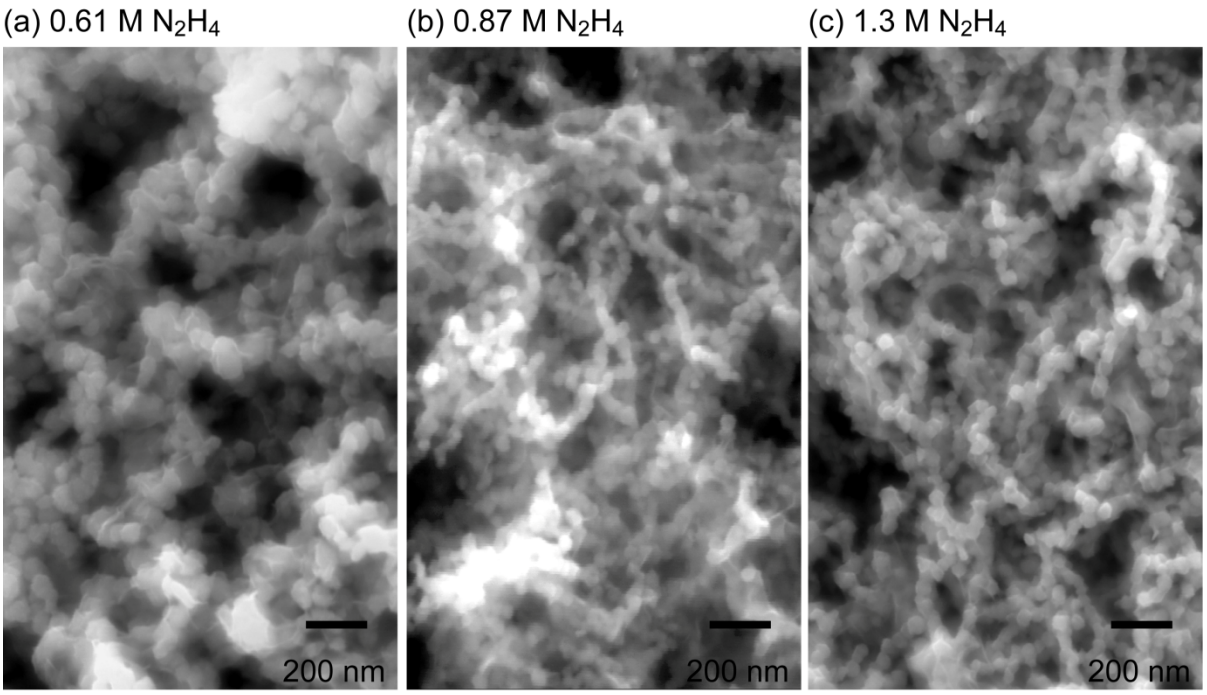

Fig. 3.24 SEM images of Co nanoparticles prepared by electroless deposition in aqueous solutions with (a) 0.61, (b) 0.87, and (c) 1.3 M N_2H_4. The mean particle diameters are (a) 75, (b) 55, and (c) 50 nm. The solutions contain 87 mM Co(II) acetate, 1.1 mM PEG, 0.22 M NaOH, and 0.22 mM H_2PtCl_6.

References

1. V. Salgueriño-Maceira, M. A. Correa-Duarte, M. Farle, M. A. Lopez-Quintela, K. Sieradzki, and R. Diaz, "Synthesis and Characterization for Colloidal Cobalt Particles', *Langmuir,* **22**, 1455 (2006).

2. Y.-W. Zhao, R. K. Zheng, X. X. Zhang, and J. Q. Xiao, "A Simple Method to Prepare Uniform Co Nanoparticles", *IEEE Trans. Magn*., **39**, 2764 (2003).

3. S. Ram, "Allotropic Phase Transformations in HCP, FCC and BCC Metastable Structures in Co-Nanoparticles" *Mater. Sci. Eng A*, **304**, 923 (2001).

4. W. M. Latimer, *The Oxidation States of the Elements and their Potentials in Aqueous Solutions,* 2nd ed., Prentice-Hall, Englewood Cliffs, NJ (1959).

5. M. D. L. Balela, S. Yagi, and E. Matsubara, "Room-Temperature Synthesis of Cobalt Nanoparticles by Electroless Deposition in Aqueous Solution", *Electrochem. Solid-State Lett.,* **13**, D4 (2010).

6. M. D. L. Balela, S. Yagi, and E. Matsubara, "Room-Temperature Synthesis of Cobalt Nanoparticles in Aqueous Solution", *ECS Trans.,* **28**, 29 (2010).

7. E. Gileadi, *Electrode Kinetics for Chemists, Chemical Engineers, and Materials Scientists*, Wiley-VCH, Inc., New York (1993).

8. M. Grzelczak, J. Perez-Juste, B. Rodriguez-Gonzales, M. Spasova, I. Barsukov, M. Farle, and L. M. Liz-Marzan, "Pt-Catalyzed Growth of Ni Nanoparticles in Aqueous CTAB Solution", *Chem. Mater.,* **20**, 5299 (2008).

9. S. Yagi, M. Kawamori, and E. Matsubara, "Electrochemical QCM Study of the Synthesis Process of Cobalt Nanoparticles via Electroless Deposition", *Electrochem. Solid-State Lett.,* **13**, E1 (2010).

10. S. Yagi, M. Kawamori, and E. Matsubara, “Electrochemical Study of the Synthesis Process of Co-Ni Alloy Nanoparticles via Electroless Deposition”, *J. Electrochem. Soc.,* **157**, E92 (2010).

11. M. D. L. Balela, S. Yagi, Z. Lockman. A. Aziz, A. V. Amorsolo Jr., and E. Matsubara, “Electroless Deposition of Ferromagnetic Cobalt Nanoparticles in Propylene Glycol”, *J. Electrochem. Soc.,* **156**, E139 (2009).

12. T. Sugimoto, *Monodispersed Particles,* Elsevier, Amsterdam (2001).

13. T. Hinotsu, B. Jeyadevan, C. N. Chinnasamy, K. Shinoda, and K. Tohji, “Size and Structure Control of Magnetic Nanoparticles by Using a Modified Polyol Processs”, *J. Appl. Phys.,* **95**, 7477 (2004).

14. N. Chakroune, G. Viau, C. Ricolleau, F. Fiévet-Vincent, and F. Fiévet, “Cobalt-Based Anisotropic Particles Prepared by the Polyol Process”, *J. Mater. Chem.,* **13**, 312-318 (2003).

15. S. Nakahara and S. Mahajan, “The Influence of Solution pH on Microstructure of Electrodeposited Cobalt”, *J. Electrochem. Soc.,* **127**, 283 (1980).

16. D.R. Gabe, “The Role of Hydrogen in Metal Electrodepositon Processes”, *J. Appl. Electrochem.*, **27**, 908 (1997).

17. M. I. Jeffrey, W. L. Choo, and P. L. Breuer, “The Effect of Additives and Impurities on the Cobalt Electrowinning Process”, *Minerals Eng.,* **13**, 1231 (2000).

18. J. T. Matsushita, F. Trivinho-Strixino, and E. C. Pereira, “Investigation of Cobalt Deposition Using the Electrochemical Quartz Crystal Microbalance”, *Electrochimica Acta*, **51**, 1960 (2006).

Chapter IV Electroless Deposition of Co Nanowires at Room Temperature under a Magnetic Field

4.1 Introduction

Control of the morphology of nanostructures is a critical aspect in the fabrication of electronic or mechanical devices and functional materials.[1-3] For example, one-dimensional (1D) ferromagnetic nanostructures, such as nanowires and nanorods, have been attracting significant attention due to their large anisotropic magnetism.[3-6] Recently, the application of magnetic field during liquid reduction is widely being used to fabricate anisotropic nanostructures due to its simplicity and effectiveness. Fe_3O_4 nanochains,[7] Ni-Co alloy microwires,[8-9] Co nanorods, [5,10,11] and Ni nanowires[4,6,12-13] have already been synthesized by magnetic-field-assisted hydrothermal process.

In this chapter, the preparation of Co nanowires at room temperature under the normal pressure will be presented. Co nanowires with a mean diameter of about 190 nm and lengths up to 160 μm are fabricated by electroless deposition in propylene glycol under parallel magnetic field. In an aqueous solution, Co nanowires of about 59 nm diameter and 30 μm long are prepared in the same manner. As discussed in Chapter III, the rate of Co deposition is largely reduced because of the decrease in the rate of N_2H_4 oxidation by carrying out the reaction in propylene glycol instead of in water. Thus, a change of the wire morphology will be discussed in different reaction rates. The reduction of Co(II) and the oxidation of N_2H_4 in propylene glycol are studied by linear sweep voltammetry, while the formation of Co particles is monitored by in-situ mixed potential measurements. The morphological and structural evolution of the products is investigated by electron microscopy

and X-ray diffraction analysis. A formation mechanism of Co nanowires in aqueous and propylene glycol solutions will be discussed.

4.2 Experimental

The chemical reagents used in this work were analytical grade (AR) Co(II) acetate tetrahydrate [$Co(C_2H_3O_2)_2 \cdot 4H_2O$], poly(ethylene glycol) [PEG, $H(OCH_2CH_2)nOH$, M_w = 20,000], propylene glycol (PG, $C_3H_8O_2$), sodium hydroxide (NaOH), hexachloroplatinic acid hexahydrate ($H_2PtCl_6 \cdot 6H_2O$), hydrazine monohydrate ($N_2H_4 \cdot H_2O$), lithium perchlorate ($LiClO_4$), and ethanol (C_2H_6O) by Nacalai Tesque. In a typical synthesis, the metal ion and reducing agent solutions were separately prepared. First, 10.0 mmol Co(II) acetate and 0.13 mmol PEG were dissolved in 50 cm^3 PG while nitrogen gas (N_2) was bubbled at 50 cm^3 min^{-1}. Then, 25 cm^3 of 1.0 M (mol dm^{-3}) NaOH in PG solution was added to hydrolyze the Co(II) ions and adjust the pH to about 12. Next, 10.0 cm^3 of 2.5 mM H_2PtCl_6-PG solution was added as a nucleating agent. To prepare the reducing agent solution, 4.0 M N_2H_4 was dissolved in 25 cm^3 deaerated PG. The N_2H_4 solution was then thoroughly mixed with the Co(II) solution in a 200 cm^3 Pyrex beaker by mechanical stirring. The total solution had a volume of 115 cm^3, with final concentrations of 87 mM Co(II) acetate, 1.1 mM PEG, 0.22 M NaOH, 0.22 mM H_2PtCl_6, and 0.87 M N_2H_4. The resulting solution was immediately placed inside a superconducting magnet (Japan Magnet Technology JMTD-10T100M) under a parallel magnetic field for 1 h. The magnetic field intensity was varied from 1 - 10 T. After the solution was kept for 1 h, Co nanowires were formed. The nanowires were separated with a magnet and ultrasonicated for 10 min in ethanol. This washing process was repeated 10 times to remove organic contaminants on the surface of the nanorods.

The morphology of the as-prepared products was observed in a field-emission-scanning electron microscope (JEOL JSM 6500-F) and a transmission electron microscope (TEM, JEOL JEM 2010). The mean diameter and lengths were determined by image analyses of 100 nanowires in each sample. The crystalline structure was investigated by X-ray diffraction (XRD) using Cr *K*α radiation (MAC Science M03XHF22).

To investigate the reduction of Co(II) ions in propylene glycol at room temperature, linear sweep voltammetry was performed using a potentiostat/galvanostat (Hokuto Denko Co. Ltd., HA-151). A Pt-sputtered quartz crystal substrate (0.196 cm^2) and a Pt sheet (4 cm^2) were used as working and counter electrodes, respectively. The voltammogram was recorded from 0 to −1.5 V at a rate of 1 mV s^{-1}. For the evaluation of the electroinactive area of propylene glycol solution in the presence of 0.22 M NaOH, the anodic and cathodic sweeps were conducted independently. Each sweep was started at the rest potential, which was observed to be reproducible. The anodic current was measured from the rest potential to 1.5 V, while the cathodic current was recorded from the rest potential to −1.5 V. The time-dependence of the mixed potential during electroless deposition of Co was also measured on a Pt-sputtered QCM substrate. All mixed potential and linear sweep voltammetric measurements in propylene glycol used 0.10 M $LiClO_4$ as supporting electrolyte. A Ag/AgCl electrode (Horiba, 2565A-10T) was used as a reference electrode. In this paper, all potentials in propylene glycol were reported against the potential of the Ag/AgCl electrode.

4.3 Results

4.3.1 Electrochemical consideration of Co deposition and N_2H_4 oxidation in propylene glycol

Figure 4.1(a) shows the linear sweep voltammogram of a propylene glycol (PG) solution containing 0.22 M NaOH. The reduction and oxidation potentials of PG are –0.80 and 0.90 V vs Ag/AgCl, respectively. In the presence of 0.22 M NaOH, PG begins to oxidize when the applied potential is more positive than 0.90 V, whereas the reductive decomposition of PG occurs at potentials more negative than –0.80 V resulting in the generation of H_2 gas. The onset potential of Co(II) reduction determined from the inflection point of the voltammogram of PG solution with 0.22 M NaOH and 87 mM Co(II) acetate in Fig. 4.1(b) is about –0.54 V. This exists in the oxidation-reduction potential window of PG. Thus, at potentials below –0.54 V up to –0.80 V, only Co deposition possibly occurs.

Figure 4.2 shows the mixed potential during electroless deposition of Co in a PG solution with 87 mM Co(II) acetate, 1.1 mM PEG, 0.22 M NaOH, 0.22 mM H_2PtCl_6, and 0.87 M N_2H_4 at room temperature. After 5 min reaction, the mixed potential drops below –0.54 V vs Ag/AgCl, and the solution simultaneously changes to black. The mixed potential then gradually decreases to about –1.0 V at 30 min after the reaction has started. Around this time, the solution is completely black and evolves H_2 gas.

Figure 4.3 are the anodic polarization curves measured on electrodeposited Co and commercial Pt-sputtered QCM substrates in a PG solution containing 0.22 M NaOH and 0.87 M N_2H_4. The anodic curves are plotted with the polarization curves measured in an aqueous solution with the same concentration of reactants; the anodic current densities are much smaller in PG than in aqueous solution, suggesting slower oxidation rate. The onset of oxidation in a PG solution is observed at about –0.70 and –0.58 V vs Ag/AgCl on the Co and

Pt electrodes, respectively. These values are more negative than the measured reduction potential of Co, indicating that Co deposition is thermodynamically plausible. The anodic current density in PG is slightly larger on Co than on Pt elecctrode, which is consistent with the results obtained in an aqueous solution.

4.3.2 Influence of magnetic field on particle morphology

Figure 4.4 shows the scanning electron microscope (SEM) and TEM images of Co products after the reaction under a magnetic field of 0 - 10 T. In the absence of the magnetic field, only spherical Co nanoparticles of about 132 nm in mean diameter are observed after 1 h reaction. High-magnification SEM images show the large Co nanoparticles made up of smaller nanoparticles in the inset of Fig. 4.4(a). On the other hand, Co nanowires are formed when the reaction is conducted under a magnetic field as in Figure 4.4(b-e). Each Co nanowire has an almost uniform diameter over its entire length and seems to be agglomerates of smaller nanoparticles [see insets of Fig.4.4(b-e)].[14] Although the Co nanoparticles prepared without magnetic fields are somewhat agglomerated [Fig. 4.4(a)], the morphology of the nanowires obtained under a magnetic field is clearly different from them. This suggests the remarkable influence of the magnetic field on the morphology of Co.

Only straight Co nanowires are obtained under a magnetic field of 1 T. They have an average diameter of about 240 nm and lengths up to 30 μm. When the strength of magnetic field is increased, longer nanowires with smoother surface are formed. Consequently, the diameters of Co nanowires are reduced. For example, Co nanowires about 190 nm in mean diameter and 160 μm long are prepared under 10 T. Bundles of Co nanowires with parallel orientations are also observed at a stronger magnetic field.

XRD profiles of the samples prepared under different magnetic field are shown in Fig. 4.5. Similar patterns are obtained for the Co nanoparticles and nanowires fabricated under 0 - 10 T. Both hcp and fcc Co peaks are observed. The crystallite sizes of Co nanoparticles and nanowires are evaluated from the widths of the 111 fcc Co peaks by Scherrer's equation, and the calculated sizes of about 12 - 15 nm are much smaller than the apparent diameters. This indicates agglomerates of small nanoparticles, which coincides with the morphology observed by electron microscopy. While the nanoparticles and nanowires are metallic Co, their very surface may have been oxidized because a weak and broad 111 cobalt oxide (CoO) peak is observed at 55.5°. Surface oxidation occurs during the washing process before the XRD measurements.

4.3.3 Formation of Co nanowires

Figure 4.6 are typical SEM images of Co products obtained after 5, 15, 17, and 20 min after the start of the reaction under 10 T. At 5 min, large agglomerated particles with diameters in the range of 100 - 500 nm are observed in Fig. 4.6(a). A mixture of short Co cylinders and spherical particles is then obtained after about 15 min reaction. These cylinders and particles have smaller diameters than the Co product after 5 min. Short Co nanowires are subsequently formed after 17 min. Extending the reaction time results in longer Co nanowires, and spherical particles are no longer present in the precipitates. Figure 4.7 shows the corresponding XRD patterns of products prepared at different reaction times under 10 T. From the XRD profiles, we can find that relatively large amount of CoO exists in the sample of 5 min reaction, which is formed from the reaction of Co(II) with OH^- ions in PG. Thus, the larger particles are agglomerates consist of CoO and metallic Co particles.

This is also verified by the fact that the particle size is reduced at 17 min and no CoO peak is observed.

4.4 Discussion

4.4.1 Mechanism of formation of Co nanowires

The schematic of the stepwise formation of Co nanowires under a magnetic field is illustrated in Fig. 4.8. First, small ferromagnetic Co nanoparticles are precipitated in the solution as primary particles, regardless of the presence of magnetic field in Stage I. These Co nanoparticles are encapsulated in solvated intermediate solid Co(II) species, resulting in the large agglomerated particles in Fig. 4.6(a). As the intermediate solid phase is dissolved in the solution, the primary Co nanoparticles become more mobile. The primary nanoparticles, however, are too small in size to align along the magnetic field under the agitation due to the gas bubbling in the reduction reaction with N_2H_4.[9] As the reaction progresses, the primary Co nanoparticles agglomerate to increase the magnetic interaction, and they consequently start to align along the magnetic field (Stage II).[15] Small Co nanoparticles are heterogeneously nucleated on the surface of the large particles, specifically at the neck of two particles. At this point, the formation energy of Co nanoparticles is less because of the reduction of the interface energy with the solvent. The large nanoparticles then grow to an ellipsoidal shape elongated along the magnetic field direction (Stage III). These ellipsoidal nanoparticles continuously grow parallel to the magnetic field in the same manner of Stage III (Stage IV) as shown in Fig 4.6(b). Finally, straight and stable Co nanowires grow with their long axes parallel to the magnetic field. As more Co nanowires are precipitated in the solution, local magnetic fields are generated, resulting in the

agglomeration of the nanowires. If a stronger magnetic field is applied, formation of thick parallel arrays of Co nanowires occurs as in Fig. 4.4(b-e).

4.4.2 Effects of increasing concentrations of H_2PtCl_6 and N_2H_4

Figure 4.9 shows the SEM images and the corresponding diameter distributions of the Co nanowires prepared with increasing concentration of nucleating agent H_2PtCl_6. The nanowire diameter apparently decreases as the concentration of H_2PtCl_6 increases. At a higher concentration of nucleating agent, smaller primary Co nanoparticles are generated due to faster nucleation of Co.[16] As a result, the growth of the primary nanoparticles is suppressed leading to the decrease in the diameter of the Co nanowires.

On the other hand, the mean diameters and lengths of the Co nanowires are reduced to some degree by decreasing the concentration of N_2H_4 as shown in Fig. 4.10. Short nanowires about 4 μm long and 180 nm in diameter are prepared at 0.43 M N_2H_4. At low concentrations of N_2H_4, the reduction of Co(II) ions is slow and a few Co nanoparticles are formed in the solution at a time. Thus, for a constant reaction time of 1 h, smaller Co nanowires are obtained with decreasing concentration of N_2H_4. Since a high concentration of H_2PtCl_6 and a low amount of N_2H_4 lead to the reduction of wire diameter, samples are fabricated using 87 mM Co(II) acetate, 1.1 mM PEG, 0.22 M NaOH, 2.2 mM H_2PtCl_6, and 0.43 M N_2H_4 under 5 T. As shown in Fig. 4.10(d), the Co product is wires with a mean diameter of about 110 nm and an aspect ratio of 600. Although the sample does not look very rigid, the Co nanowires apparently possess some mechanical strength since they retain their morphology even after several ultrasonic washing. Therefore, by controlling the reduction rate with the concentration of reactants, the morphology of the Co products under a

magnetic field can be changed from ellipsoidal particles to short cylinders, and finally to smooth nanowires.

4.4.3 Influence of solvent

Using water instead of PG as a solvent for Co(II) solution, Co nanowires are fabricated in the same method described in the experimental section. Figure 4.11(a-b) show the SEM images of the Co products prepared under 0 and 10 T. Spherical Co nanoparticles with a mean diameter of about 54 nm were prepared under 0 T as it is seen in Fig. 4.11(a). In contrast, Co nanowires of less than 30 μm long and an average diameter of about 59 nm are obtained under 10 T. Compared to the smooth nanowires formed in PG, the Co nanowires in Fig. 4.11(b) appear as linear networks of self-aligned spherical nanoparticles. The variation in morphology can be attributed to difference in the reaction rates in PG and aqueous solutions, with the slower reaction in PG favoring the formation of smooth and long nanowires. Nonetheless, the Co nanowires in Fig. 4.11(b) are strong and stable since they maintain their morphology after washing.

Figure 4.12 shows the SEM images of Co products obtained in an aqueous solution from 5 - 20 min reaction under 10 T. At 5 - 10 min, spherical Co nanoparticles are observed and show no clear difference regardless of the magnetic field. The particle size is slightly increased from 44 nm at 5 min to 52 nm at 10 min. Bead-like nanowires up to 1 μm long and 52 nm in diameter are then formed after 15 min reaction. After 20 min, the Co nanowires grow up to 20 μm long. In an aqueous solution, the fast deposition of Co possibly promotes the rapid alignment of Co nanoparticles along the magnetic field once they have grown to a certain size (about 52 nm). Consequently, bead-like nanowires are obtained instead of

smooth nanowires. On the other hand, the corresponding XRD patterns of the Co products obtained under 10 T in Fig. 4.13 show the same hcp and fcc Co peaks with comparable intensity ratios. This suggests that the structure of Co is not affected by the magnetic field possibly due to the rapid nucleation of Co nanoparticles.

A schematic diagram illustrating the stepwise formation of Co nanowires in an aqueous solution under a magnetic field is shown in Fig. 4.14. At the early stage in the reaction in an aqueous solution (Stage I), spherical Co nanoparticles are rapidly precipitated due to the fast reaction rate regardless of the magnetic field. Because of the enhanced oxidation of N_2H_4 in water, Co(II) is immediately reduced on the surface of the primary Co nanoparticles, resulting in an increase in particle size. Since the dipole magnetic moment is proportional to the volume of a nanoparticle, the magnetic interaction among the Co nanoparticles becomes stronger to be significantly affected by the magnetic field once they have reached a certain size. Subsequently, when the dipole magnetic moments of the Co nanoparticles are oriented along the magnetic field, attractive interactions are induced parallel to the magnetic field direction. Thus, neighboring Co nanoparticles start to assemble and form linear networks of spherical nanoparticles aligned along the magnetic field direction (Stage II) as it is seen in Fig. 4.12(c-d). As the reaction proceeds, Co is heterogeneously nucleated on the gaps between the spherical nanoparticles because of the reduction of interfacial energy. This leads to the formation of Co nanowires (Stage III). Since the reaction in an aqueous solution is much faster than in PG, the morphology of the nanowires is bead-like shape.

To elucidate the effect of deposition rate on the morphology of Co nanowires, 2.0 mM sodium citrate is added as a complexing agent to stabilize the Co(II) ions in an aqueous

solution. Large Co nanowires with smoother surface morphology are obtained after 1 h under 10 T as shown in Fig. 4.11(c-d). The diameter of the Co nanowires is increased to about 180 nm, while the length is reduced to about 10 μm. Spherical Co particles of 100 - 200 nm diameters are also observed in the sample with sodium citrate. These Co nanowires are possibly formed by the assembly of the large particles, which are then connected by Co atoms. Due to the reduction in the reaction rate, smoother nanowires are formed.

4.5 Summary

Stable Co nanowires with a mean diameter of about 190 nm and lengths up to 160 μm are successfully fabricated by electroless deposition in propylene glycol solution at room temperature under a magnetic field. Without the magnetic field, only spherical Co particles are obtained. The size of the nanowires is varied to some extent by the strength of the magnetic field; longer and thinner nanowires are formed under a stronger magnetic field. The wire morphology is greatly influenced by the rate of Co deposition. A slow reaction rate favors the formation of long and smooth Co nanowires. Thus, by changing process parameters, such as the concentrations of nucleating and reducing agents, type of solvent, and addition of a complexing agent, the wire morphology can be changed from bead-like networks of particles to smooth nanowires.

The formation mechanism of Co nanowires under a magnetic field is proposed. Regardless of the solvent and the magnetic field strength, spherical Co nanoparticles are first precipitated in the solution. These nanoparticles are magnetized by the magnetic field and then assembled to grow along the magnetic field direction. Consequently, robust Co nanowires are formed with long axes parallel to the direction of the magnetic field.

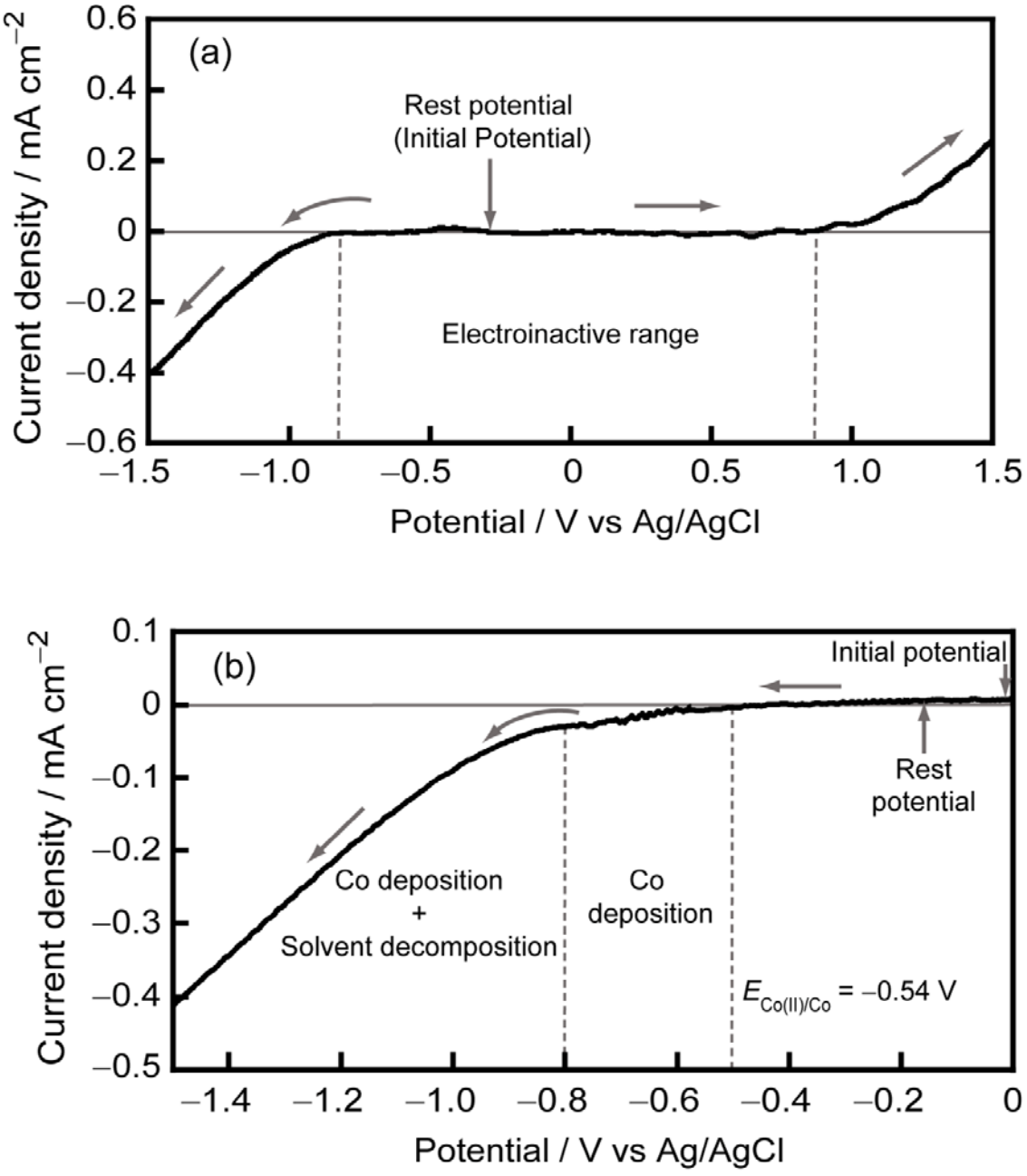

Figure 4.1 Voltammograms measured at 1 mV s^{-1} of a propylene glycol solution containing (a) 0 and (b) 87 mM Co(II) acetate using Pt-sputtered QCM electrodes. The solutions contain 0.22 M NaOH and 0.10 M $LiClO_4$ as supporting electrolyte. The arrows indicate the direction of the sweep.

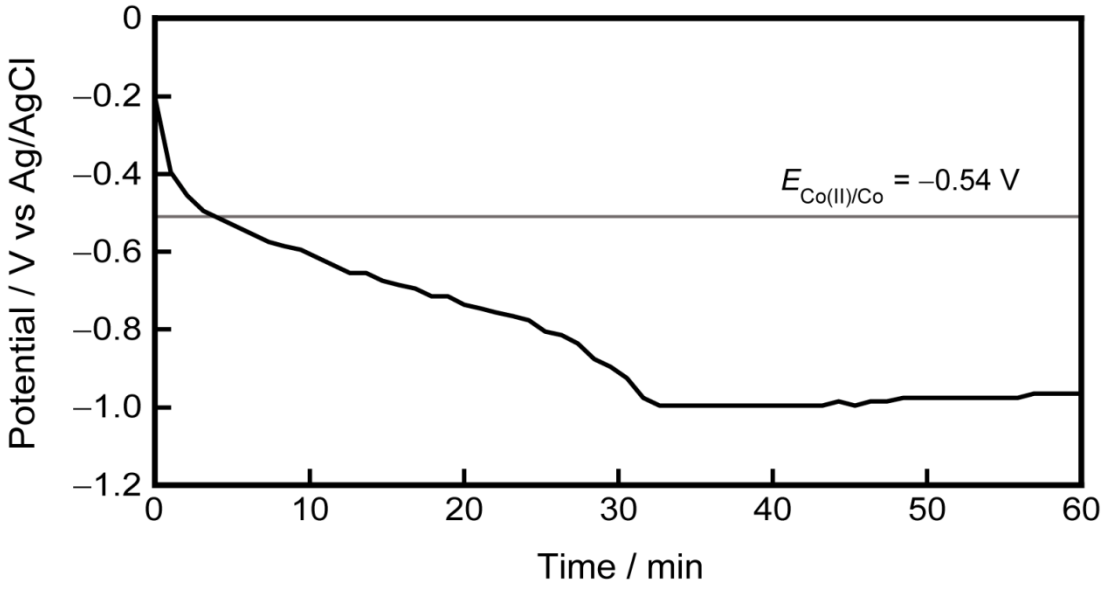

Figure 4.2 Change in mixed potential with time measured on Pt-sputtered QCM substrate during electroless deposition of Co nanoparticles in a propylene glycol solution at room temperature. The solution contains 87 mM Co(II) acetate, 1.1 mM PEG, 0.22 M NaOH, 0.22 mM H_2PtCl_6, 0.87 M N_2H_4, and 0.10 M $LiClO_4$ as supporting electrolyte.

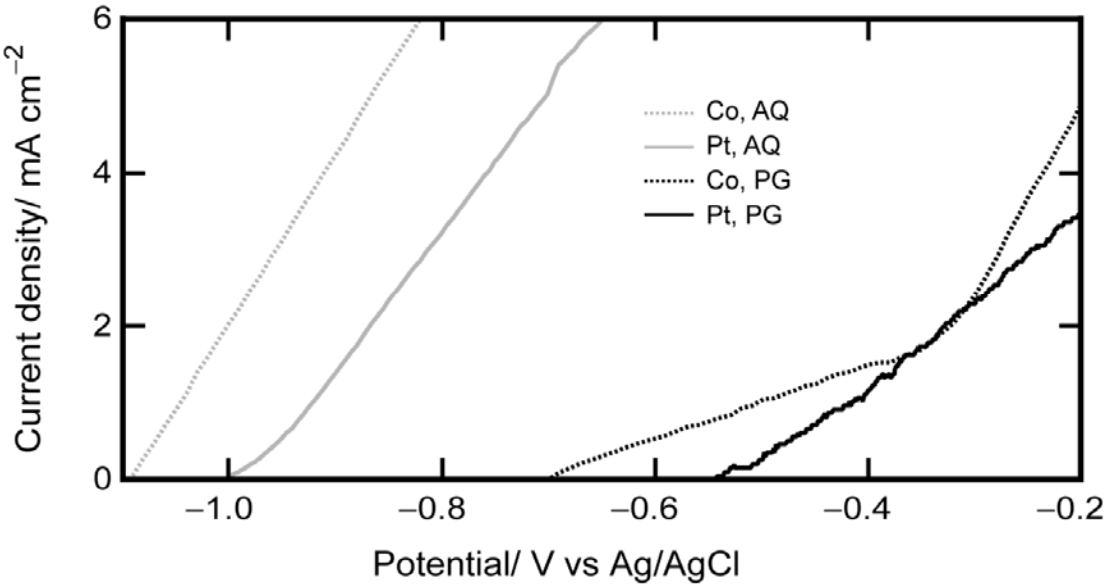

Figure 4.3 Anodic polarization curves measured at 1 mV s^{-1} at room temperature on electrodeposited Co and commercial Pt-sputtered QCM substrates in aqueous (AQ) and propylene glycol (PG) solutions containing 0.22 M NaOH and 0.87 M N_2H_4. 0.10 M $Na2SO_4$ and 0.10 M $LiClO_4$ are used as supporting electrolytes in aqueous and propylene glycol solutions, respectively.

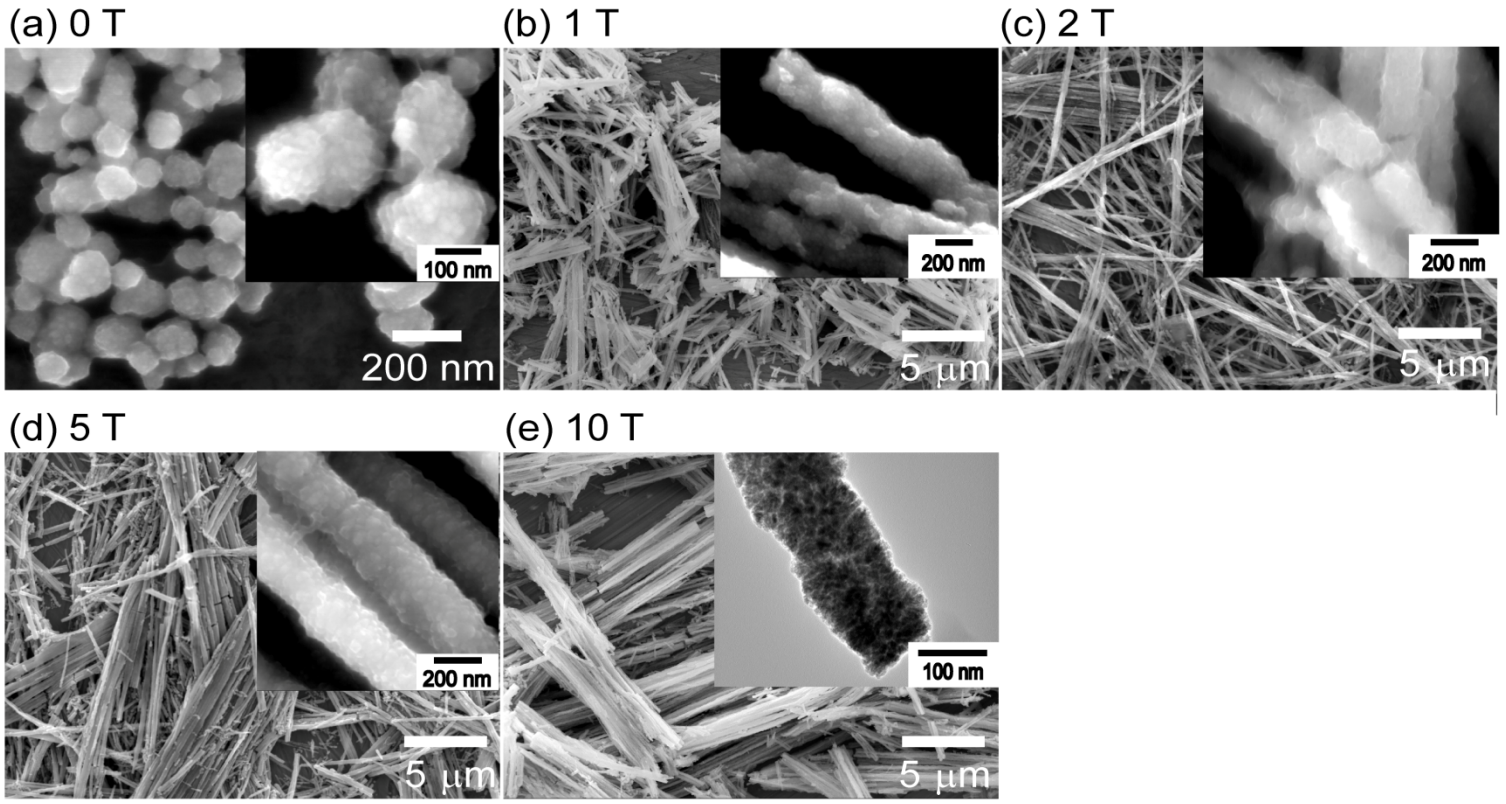

Figure 4.4 SEM and TEM images of Co products fabricated by electroless deposition in a PG solution with 87 mM Co(II) acetate, 1.1 mM PEG, 0.22 M NaOH, 0.22 mM H_2PtCl_6, and 0.87 M N_2H_4 under a magnetic field of (a) 0, (b) 1, (c) 2, (d) 5,and (e) 10 T.

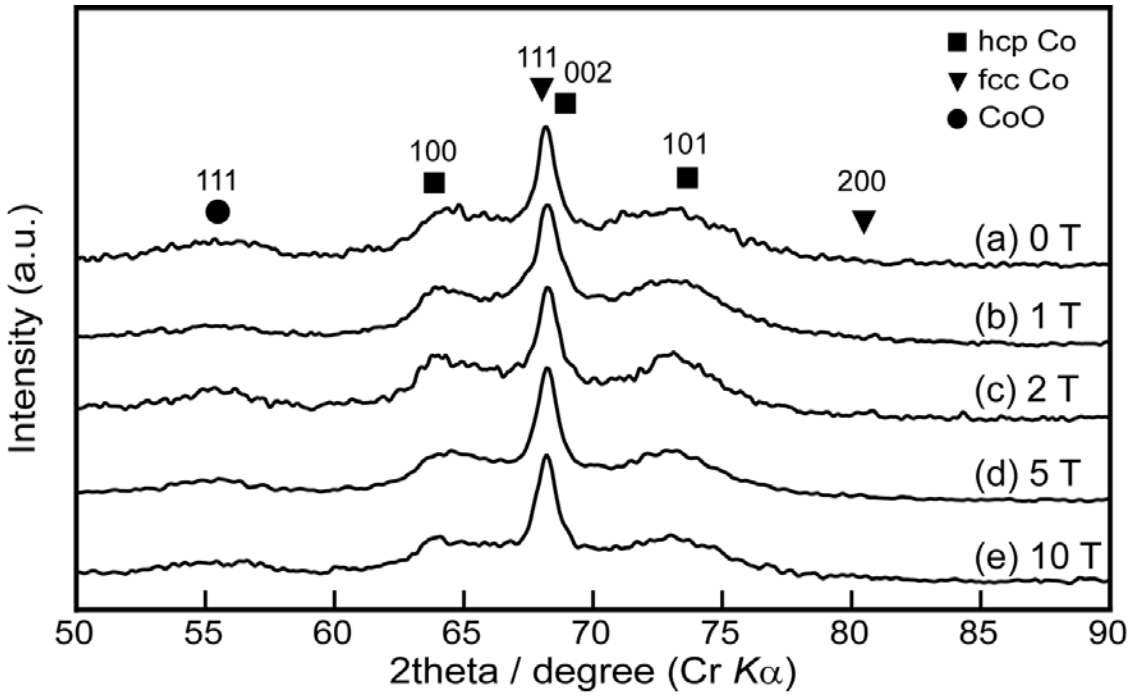

Figure 4.5 Corresponding XRD profiles of the samples prepared under (a) 0, (b) 1, (c) 2, (d) 5, and (e) 10 T in a PG solution with 87 mM Co(II) acetate, 1.1 mM PEG, 0.22 M NaOH, 0.22 mM H_2PtCl_6, and 0.87 M N_2H_4.

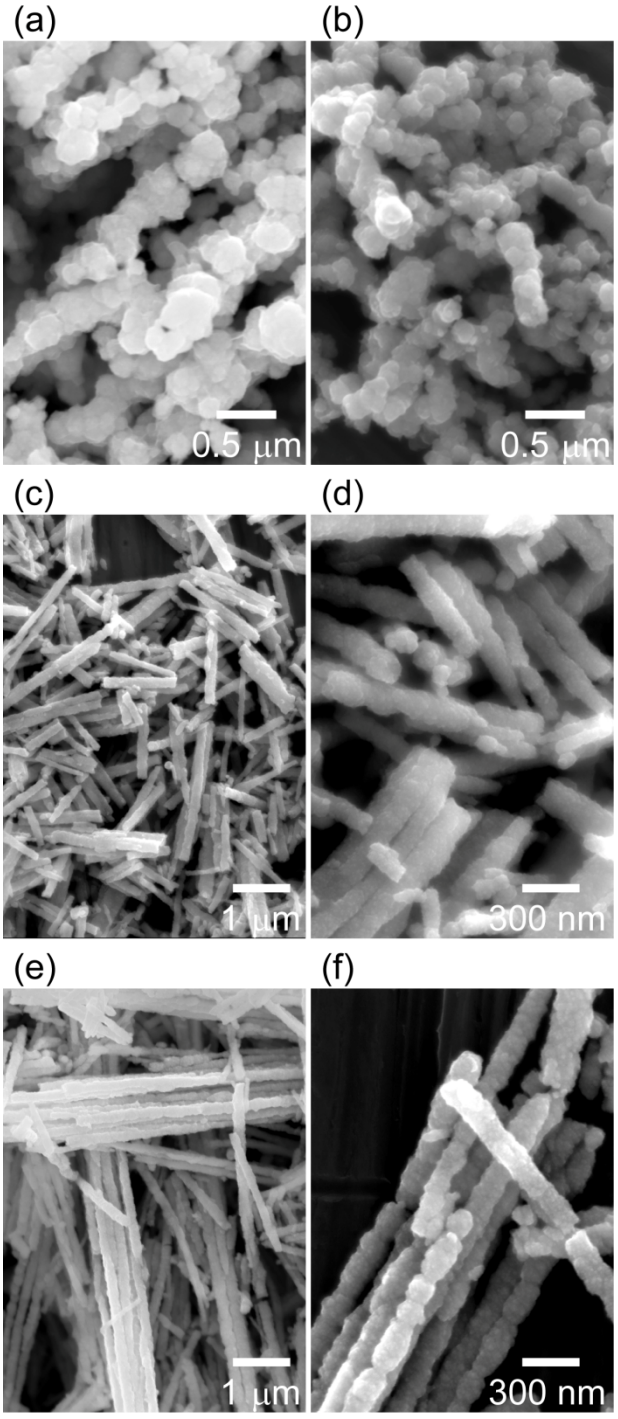

Figure 4.6 SEM images of Co products obtained at reaction times of (a) 5, (b) 15, (c,d) 17, and (e,f) 20 min under 10 T in a PG solution containing 87 mM Co(II) acetate, 1.1 mM PEG, 0.22 M NaOH, 0.22 mM H_2PtCl_6, and 0.87 M N_2H_4.

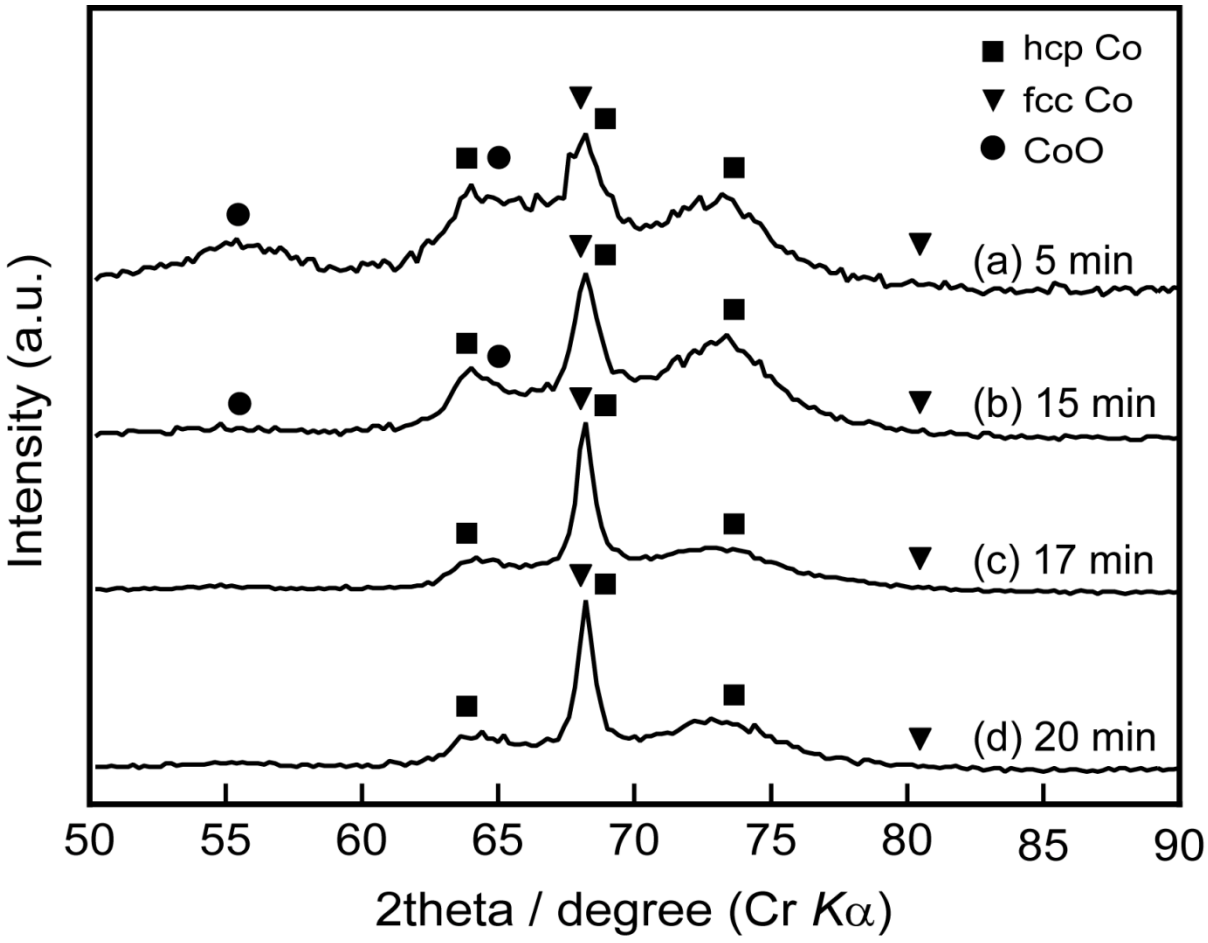

Figure 4.7 XRD patterns of Co products obtained at reaction times of (a) 5, (b) 15, (c) 17, and (d) 20 min under 10 T in a PG solution containing 87 mM Co(II) acetate, 0.22 M NaOH, 1.1 mM PEG, 0.22 M NaOH, 0.22 mM H_2PtCl_6, and 0.87 M N_2H_4.

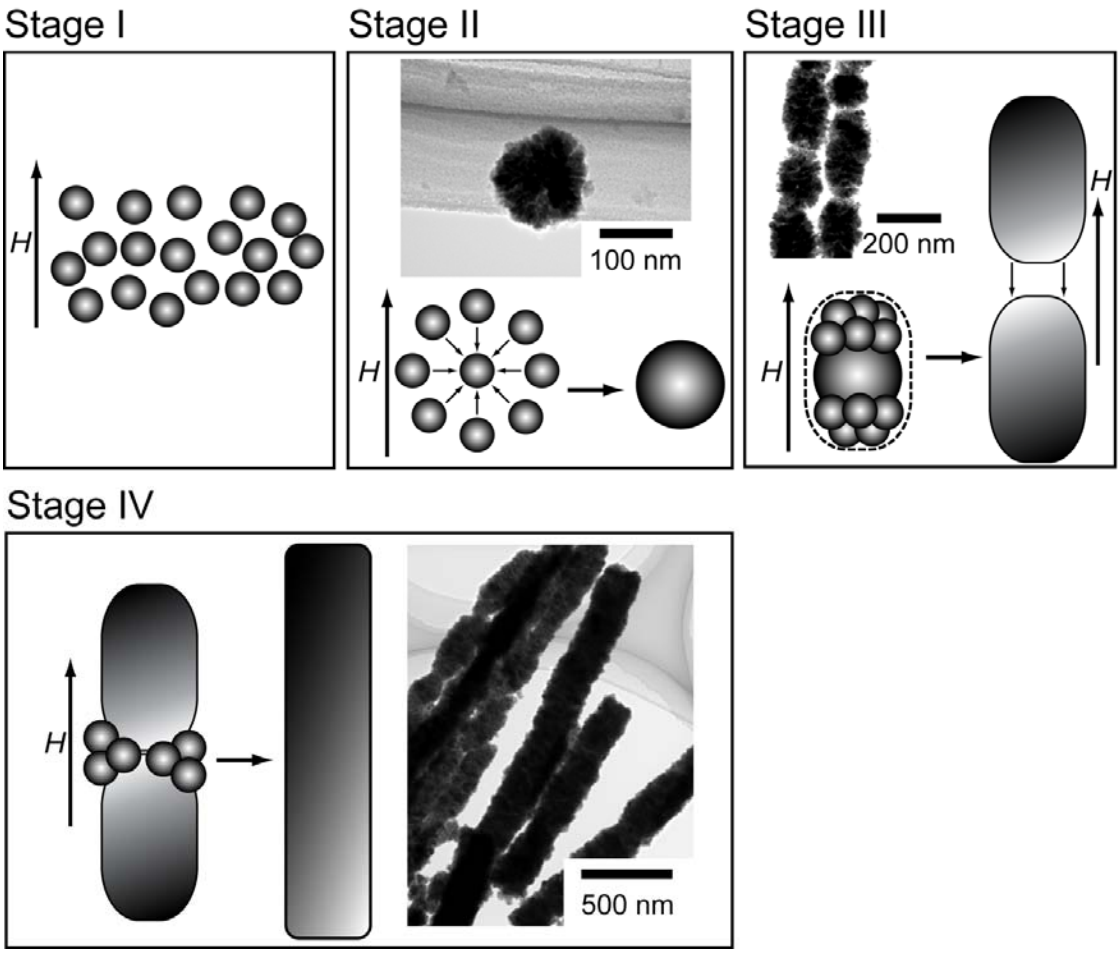

Figure 4.8 Schematic of the formation of Co nanowires by electroless deposition in a PG solution at room temperature under a magnetic field.

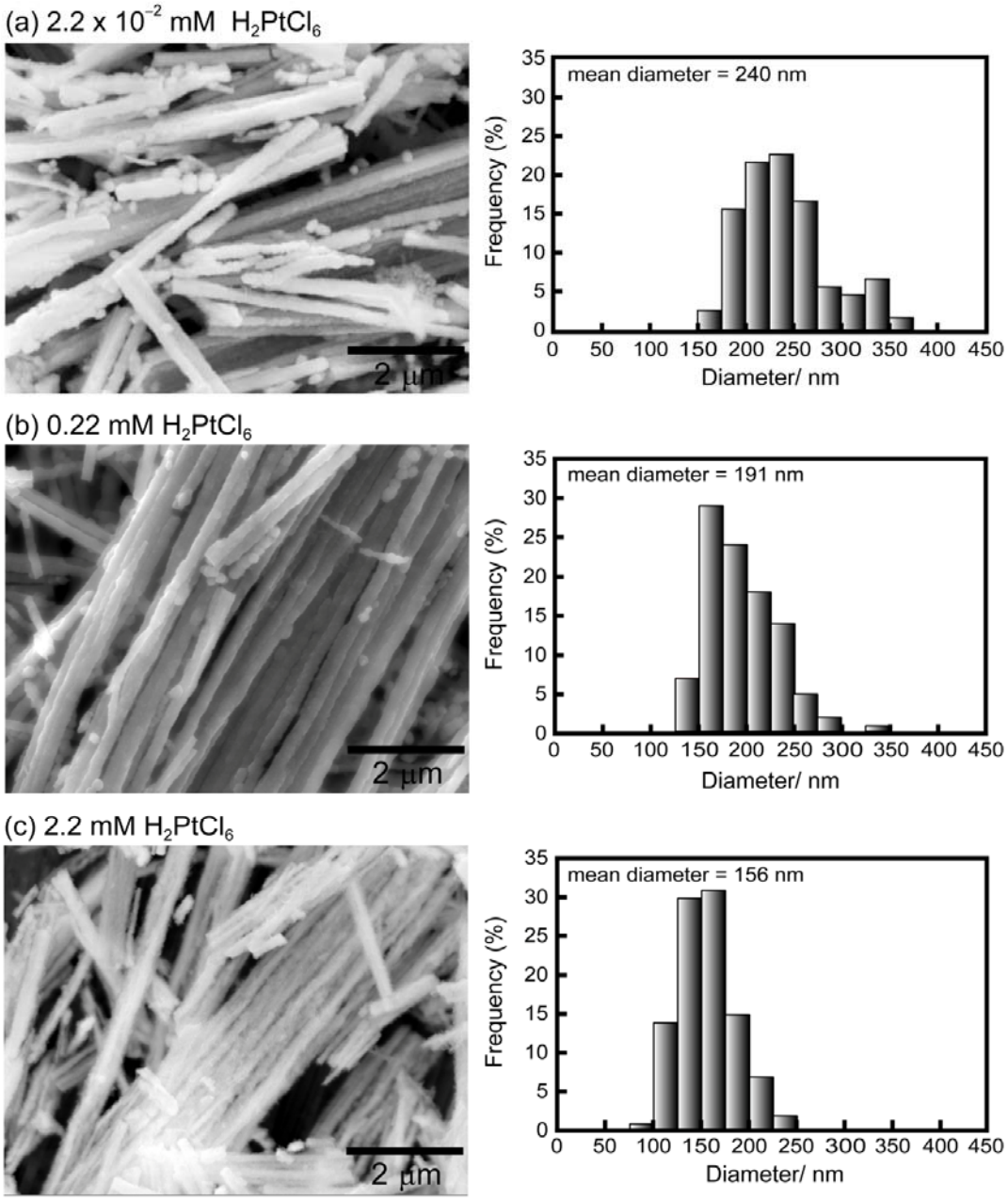

Figure 4.9 SEM images of Co nanowires prepared by adding (a) 2.2 x 10^{-2} (b) 0.22, and (c) 2.2 mM H_2PtCl_6 in a PG solution with 87 mM Co(II) acetate, 1.1 mM PEG, 0.22 M NaOH, and 0.87 M N_2H_4 under 5T. The corresponding diameter distributions of the samples are also shown.

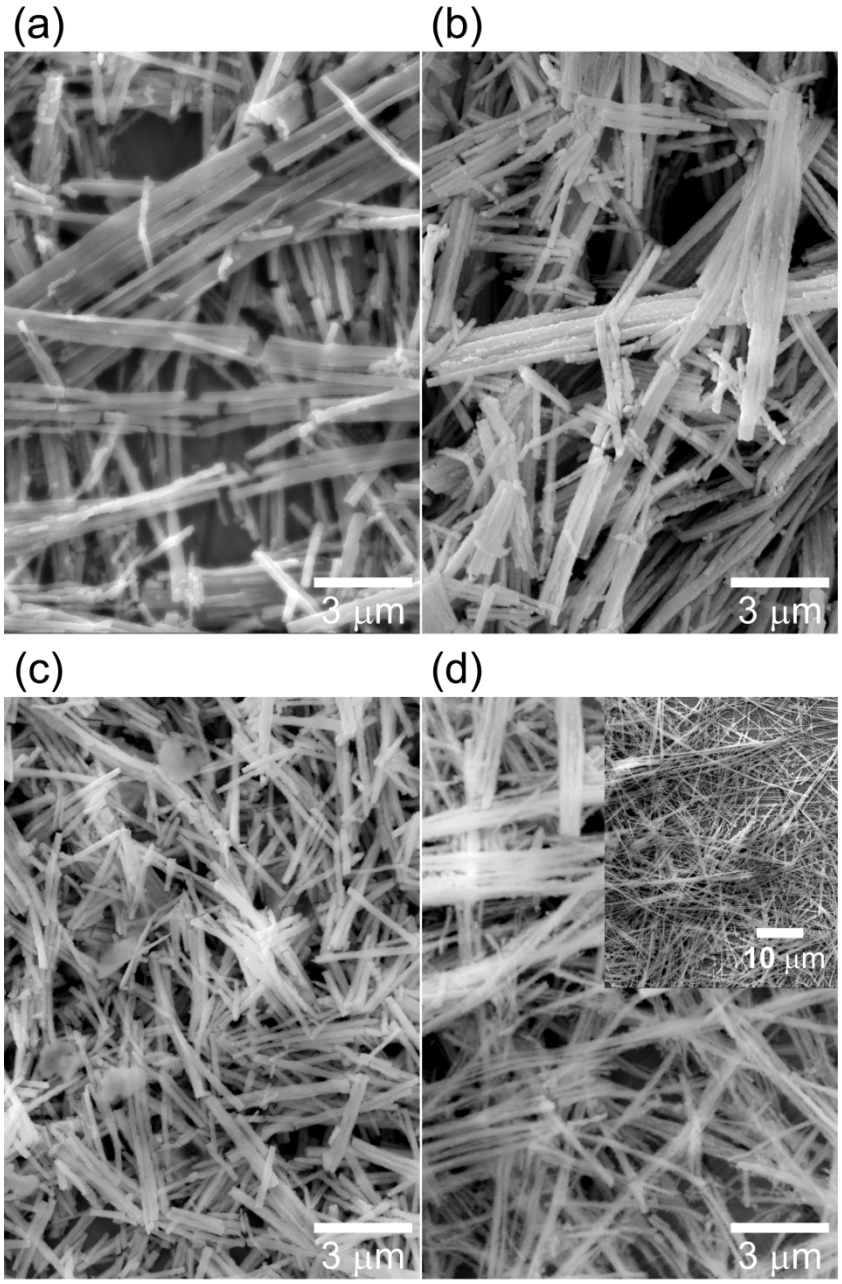

Figure 4.10 SEM images of Co nanowires synthesized with (a) 0.87 M (b) 0.61 M, and (c,d) 0.43 M N_2H_4 at room temperature under 5T. Samples (a-c) are prepared in a PG solution with 87 mM Co(II) acetate, 1.1 mM PEG, 0.22 M NaOH, and 0.22 mM H_2PtCl_6, whereas sample (d) is prepared in a PG solution containing 87 mM Co(II) acetate, 1.1 mM PEG, 0.22 M NaOH,and 2.2 mM H_2PtCl_6.

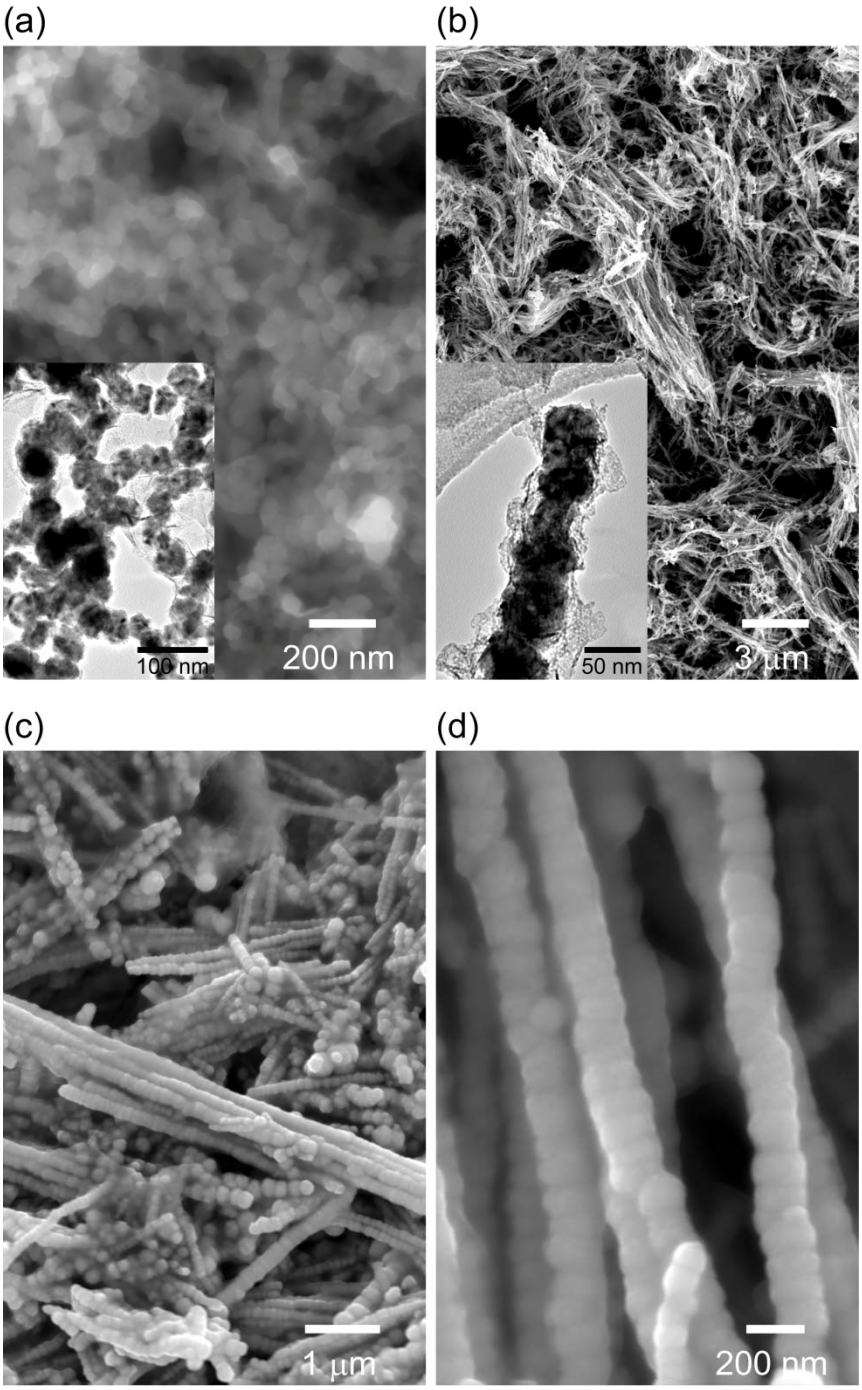

Figure 4.11 SEM and TEM images of Co products obtained by electroless deposition under (a) 0 and (b) 10 T in an aqueous solution with 87 mM Co(II) acetate, 1.1 mM PEG, 0.22 M NaOH, 0.22 mM H_2PtCl_6, and 0.87 M N_2H_4. (c,d) SEM images of Co nanowires prepared under 10 T by adding 2.0 mM sodium citrate into the original Co solution.

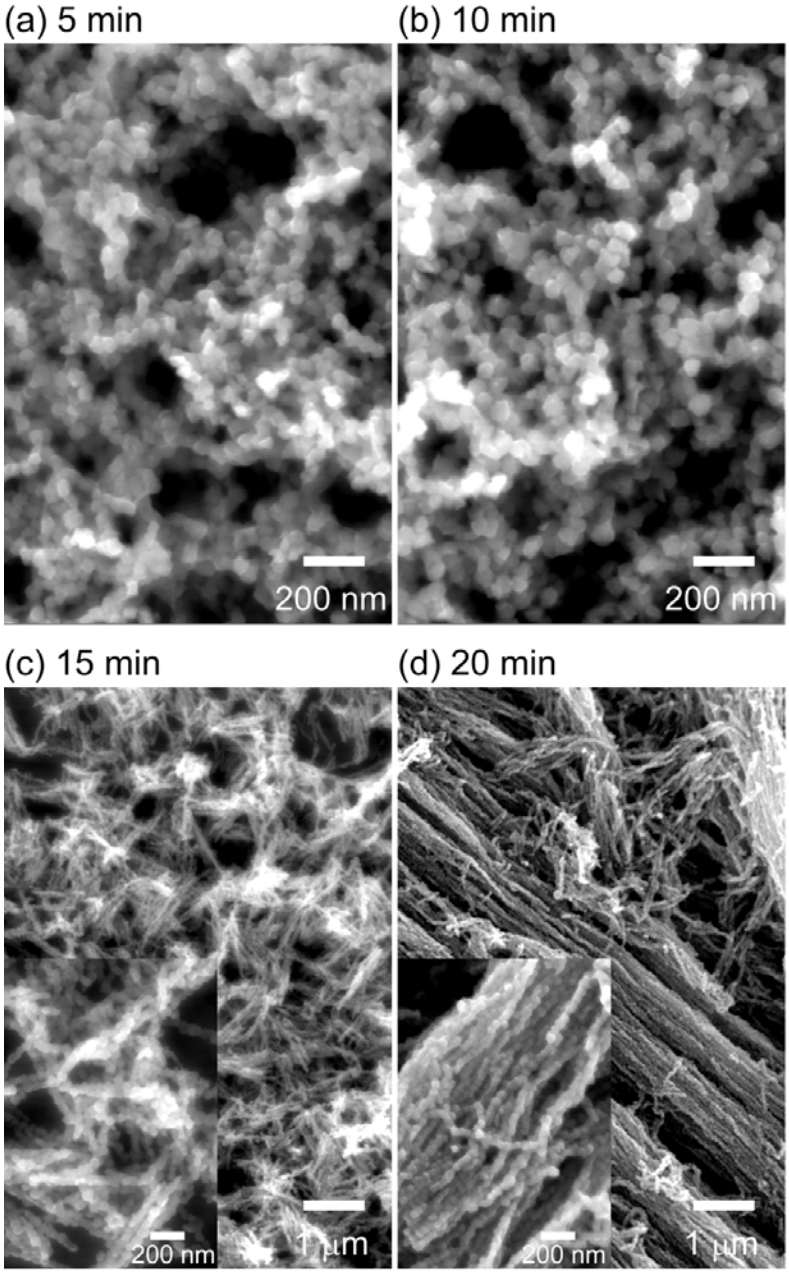

Figure 4.12 SEM images of the Co products obtained under 10 T at a reaction time of (a) 5, (b) 10, (c) 15, and (d) 20 min in an aqueous solution containing 87 mM Co(II) acetate, 1.1 mM PEG, 0.22 M NaOH, 0.22 mM H_2PtCl_6, and 0.87 M N_2H_4.

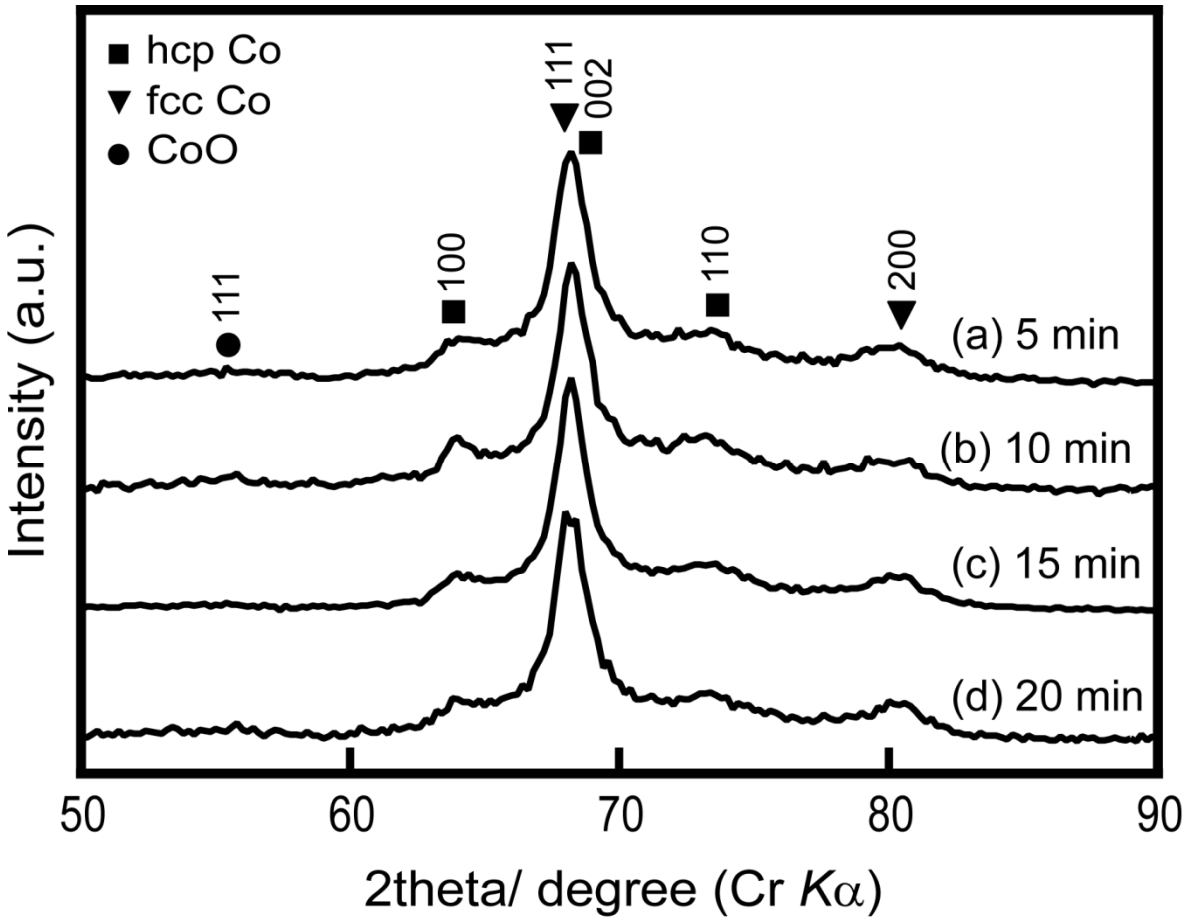

Figure 4.13 XRD profiles of the Co products obtained under 10 T at a reaction time of (a) 5, (b) 10, (c) 15, and (d) 20 min in an aqueous solution containing 87 mM Co(II) acetate, 1.1 mM PEG, 0.22 M NaOH, 0.22 mM H_2PtCl_6, and 0.87 M N_2H_4.

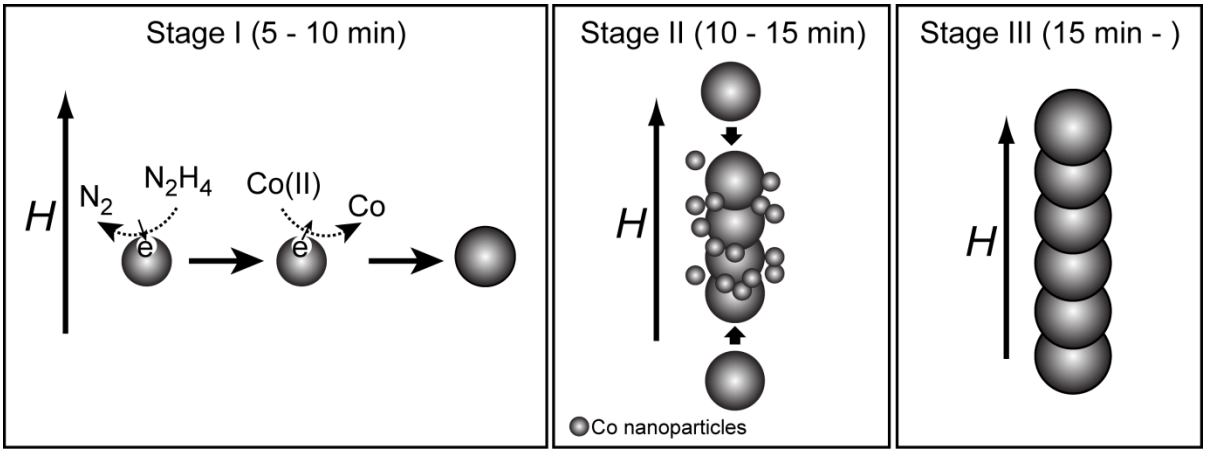

Figure 4.14 Schematic diagram of the formation of Co nanowires by electroless deposition in an aqueous solution at room temperature under a magnetic field using N_2H_4 as reducing agent.

References

1. E. K. Athanassiou, P. Grossman, R. N. Grass, and W. J. Stark, "Template Free, Large Scale Synthesis of Cobalt Nanowires Using Magnetic Fields for Alignment", *Nanotech.,* **18**, 165606 (2007).

2. M. Aslam, R. Bhobe, N. Alem, S. Donthu, and V. P. Dravid, "Controlled Large-Scale Synthesis and Magnetic Properties of Single-Crystal Cobalt Nanorods", *J. Appl. Phys.,* **98**, 074311 (2005).

3. G. Viau, C. Garcia, T. Maurer, G. Chaboussant, F. Ott, Y. Soumare, and J.-Y. Piquemal, "Highly Crystalline Cobalt Nanowires with High Coercivity Prepared by Soft Chemistry", *Phys. Status Solidi. A,* **206**, 663 (2009).

4. G. Zhang, T. Zhang, X. Lu, W. Wang, J. Qu, and X. Li, "Controlled Synthesis of 3D and 1D Nickel Nanostructures Using an External Magnetic Field Assisted Solution-Phase Approach", *J. Phys. Chem,* **111**, 12663 (2007).

5. B.-Y. Xie, Y. Qian, S. Zhang, S. Fu, and W. Yu, "A Hydrothermal Reduction Route to Single-Crystalline Hexagonal Cobalt Nanowires", *Eur. J. Inorg. Chem.,* **2006**, 2454 (2006).

6. H. Niu, Q. Chen, M. Ning, Y. Jia, and X. Wang, "Synthesis and One-Dimensional Self-Assembly of Acicular Nickel nanocrystallites under Magnetic Fields", *J. Phys. Chem. B,* **108**, 3996 (2004).

7. H. Wang, Q.-W. Chen, L.-X. Sun, H. Qi, S. Zhou, and J. Xiong, "Magnetic-Field-Induced Formation of One-Dimensional Magnetite Nanochains", *Langmuir*, **25**, 7135 (2009).

8. M. Wu, G. Liu, M. Li, P. Dai, Y. Ma, and L. Zhang, "Magnetic Field-Assisted Solvothermal Assembly of One-Dimensional Nanostructures of Ni-Co Alloy Nanoparticles", *J. Alloys and Compounds,* **491**, 689 (2010).

9. M. J. Hu, B. lin, S. H. Yu, “Magnetic Field-Induced Sovothermal Synthesis of One-Dimensional Assemblies of Ni-Co Alloy Microstructures”, *Nano. Res.,* **1**, 303 (2008).

10. J. Wang, M. Yao, C. Xu, Y. Zhu, G. Xu, and P. Cui, “Magnetic chains of Co Spheres Synthesized by Hydrothermal Process under Magnetic Field”, *Mater. Lett.*, **62**, 3431 (2008).

11. F. Liang, L. Guo, Q. P. Zhong, X. Wen, S. Yang, W. Zheng, C. Chen, N. Zhang, and W. Chu., “One-Step Solution Fabrication of Magnetic Chains Consisting of Jingle-Bell-Shaped Cobalt Mesospheres”, *Appl. Phys. Lett.,* **89**, 103105 (2006).

12. H. Niu, Q. Chen, H. Zhu, Y. Lin, and X. Zhang, “Magnetic Field-Induced Growth and Self-Assembly of Cobalt Nanocrystallites”, *J. Mater. Chem.,* **13**, 1803 (2003).

13. C. Gong, J. Tian, T. Zhao, Z. Wu, and Z. Zhang, “Formation of Ni Chains Induced by Self-Generated Magnetic Field” *Mater. Research Bull.*, **44**, 35 (2009).

14. F. Wang, H. Gu, and Z. Zhang, “Preparation Of Cobalt Nanocrystals in the Homogenous Solution with the Presence of a Static Magnetic Field”, *Mater. Research Bull.*, **38**, 347 (2003).

15. J. Park, Y. Jun, J. Choi, and J. Cheon, “Formation of One-Dimensional Nickel Wires by Chemical Reduction of Nickel Ions under Magnetic Fields”, *Chem. Comm.,* **2007**, 5001 (2007).

16. M. D. L. Balela, S. Yagi, and E. Matsubara, “Room-Temperature Synthesis of Cobalt Nanoparticles by Electroless Deposition in Aqueous Solution”, *Electrochem. Solid–State Lett.,* **13**, D4 (2010).

Chapter V General Summary

Co nanoparticles have been successfully synthesized by a variety of liquid-phase methods, specifically in an organic solution at an elevated temperature. This is attributed to the difficulty of formation of non-agglomerated and un-oxidized Co nanoparticles in an aqueous solution at room temperature. The polyol synthesis has been widely used for the fabrication of size-controlled Co nanoparticles with a narrow size distribution. However, the study of the synthesis conditions for the formation of Co nanoparticles is still empirical. Therefore, in-situ mixed potential measurements are carried out to investigate the electroless depositions of Co nanoparticles in boiling propylene glycol. The monitoring of mixed potential during the reaction has been useful in understanding the effects of temperature, concentration of NaOH, and addition of different nucleating agents on the oxidation rate of propylene glycol, as well as on the rate of formation of Co particles. Thus, the optimum conditions for the formation of Co particles are determined. The mixed potential of propylene glycol decreases with an increase in temperature and concentration of NaOH. This indicates a faster oxidation of propylene glycol leading to the formation of decomposition products. Consequently, Co(II) reduction is accelerated, and smaller Co particles are obtained.

In the presence of nucleating agents, the mixed potential is further decreased, and Co(II) reduction occurs at temperatures below the boiling point of propylene glycol. The smallest Co particles are then produced, suggesting that the nucleating agent does not only aid in the formation of minute Co particles, but also enhances the oxidation of propylene glycol. The nature of the nucleating agent apparently influences both the particle

morphology and reaction rate. At the same concentration of nucleating agent, the addition of H_2PtCl_6 results in the largest decrease in the boiling temperature, leading to the formation of the finest Co nanoparticles. The optimum conditions determined for the electroless deposition of Co particles in boiling propylene glycol are then applied for the electroless deposition of Co in an aqueous solution at room temperature.

Using similar reaction conditions as the polyol process, the formation of Co nanoparticles by electroless deposition in an aqueous solution at room temperature is studied. At 5 min reaction time, Co nanoparticles of about 44 nm are obtained in an aqueous solution containing 87 mM Co(II) acetate, 1.1 mM PEG, 0.22 M NaOH, 0.22 mM H_2PtCl_6, and 0.87 M N_2H_4. This coincides with the drop of the mixed potential below the oxidation-reduction potential of the Co(II)/Co redox pair. Both Co particle size and mixed potentials are decreased with an increase in the concentrations of NaOH and H_2PtCl_6. The current density for N_2H_4 oxidation is larger at a higher concentration of H_2PtCl_6, possibly due to the catalytic activity of small Pt nanoparticles. A higher concentration of NaOH results in larger anodic currents and lower oxidation potential for N_2H_4, indicating a stronger reducing force with increasing NaOH concentration. In addition, the reduction potential of Co shifts negatively with a higher concentration of NaOH. Therefore, the mixed potential is decreased and Co deposition is enhanced. Hence, the particle size of the Co nanoparticles is decreased. On the other hand, the addition of propylene glycol in the solution decreases the anodic current density for N_2H_4 oxidation, which results in the increase in the mixed potentials. Co deposition is therefore suppressed, and larger Co nanoparticles are obtained.

When electroless deposition of Co at room temperature is conducted under a magnetic field, Co nanowires are fabricated instead of spherical nanoparticles. Using

propylene glycol as solvent, Co nanowires with a mean diameter of about 190 nm and lengths up to 160 μm are obtained after 1 h under 10 T. The size of the nanowires is dependent of the magnetic field strength; longer and thinner nanowires are formed under a stronger magnetic field. When the reaction is conducted in water, bead-like networks of Co nanoparticles about 59 nm in mean diameter and 30 μm long are formed under 10 T. These nanowires appear to have some mechanical strength since they maintain their morphology even after ultrasonication. Therefore, the wire morphology is significantly dependent on the rate of Co deposition. By changing the reaction conditions, such as the concentrations of H_2PtCl_6 and N_2H_4, the type of solvent, and addition of complexing agent like sodium citrate, the rate of Co deposition can be controlled, and the wire morphology can be tailored from bead-like networks to ellipsoidal particles to smooth nanowires. The formation of long and smooth Co nanowires is generally favored at a slower reaction rate. Nonetheless, smooth and robust nanowires up to 20 μm long are obtained after 20 min reaction in propylene glycol at 10 T.

The formation of mechanism of Co nanowires under a magnetic field is proposed. Regardless of the magnetic field and solvent, small Co nanoparticles are first formed in the solution as primary particles. These primary particles are strongly magnetized by the magnetic field and then assembled to grow along the magnetic field direction. Consequently, stable Co nanowires are formed with long axes aligned along the magnetic field.

List of Publications

Journals

M. D. L. Balela, S. Yagi, and E. Matsubara, Electroless Deposition of Co Nanowires in an Aqueous Solution under External Magnetic Field, *Electrochem. Solid-State Lett.*, **14**, D68 (2011).

M. D. L. Balela, S. Yagi and E. Matsubara, Fabrication of Co Nanowires by Electroless Deposition under External Magnetic Field, *J. Electrochem. Soc.*, **158**, D210 (2011).

M. D. L. Balela, S. Yagi, and E. Matsubara, Room-Temperature Synthesis of Co Nanoparticles by Electroless Deposition in Aqueous Solution, *Electrochem. Solid-State Lett.*, **13**, D4 (2010).

M. D. L. Balela, S. Yagi, Z. Lockman, A. Aziz, AV Amorsolo Jr, and E. Matsubara, Electroless Deposition of Co Nanoparticles in Propylene Glycol, *J. Electrochem. Soc.*, **156**, E139 (2009).

Proceeding

M. D. L. Balela, S. Yagi, and E. Matsubara, Room-Temperature Synthesis of Co Nanoparticles in Aqueous Solution, *ECS Trans.*, **28**(7), 29 (2010).

List of Presentations

Oral Presentations

Room-Temperature Synthesis of Co Nanoparticles by Electroless Deposition in Aqueous Solution, Joint Symposium on Materials Science and Engineering for the 21st Century, Korean Advanced, Institute of Science and Technology, South Korea, 27-29 June 2010 (Oral Presentation Award)

Room-Temperature Synthesis of Co Nanoparticles in Aqueous Solution, 217th The Electrochemical Society Meeting, Hyatt Regency Hotel, Vancouver, Canada, 25-30 April 2010.

Poster Presentation

Liquid-Phase Synthesis of Metallic Cobalt Nanoparticles by Electroless Deposition in Propylene Glycol, 29th The Philippine-American Academy of Science and Engineering (PAASE) Annual Meeting and Symposium, Ateneo de Manila University, Philippines, 13-15 July 2009.

Acknowledgement

I would like to extend my gratitude to the following individuals for their significant contributions in making the current research work possible:

- *Prof. Eiichiro Matsubara*, for the PhD opportunity, for the guidance, teachings, and discussions, for imparting the value of research.

- *Dr. Shunsuke Yagi*, for the conversations, arguments, debates, for the invaluable comments and advices, for the assistance in the experiments

- *Dr. Tetsu Ichitsubo and Mr. Kenji Kazumi*, for their assistance in magnetic measurements and TEM analysis

- *Dr. Murase, Prof. Nakamura, and Prof. Sugimura*, for their suggestions and comments during the doctoral presentation

- *Mr. Hidetaka Nakanishi, Mr. Makoto Kawamori, Ms. Mari Otogawa, Ms. Tomoe Weedall, Mr. Kawaguchi Tomoya, and the rest of the members of the Matsubara Laboratory*, for the company and assistance in the laboratory.

- *Dr. Michael Delmo*, for the comments, for teaching and explaining about magnetism and magnetic properties

- *My family*, for their encouragement and support.

- *Eugene Clef* – for the blind faith, and for keeping me sane every day

Most of all, to *God Almighty* for all the blessings and opportunities, for the good health, and for the wonderful people who keeps my life fun and interesting every single day.